12-2020

Understanding Radiation Resistance in Head and Neck Tumor Xenografts Using Diffuse Reflectance and Raman Spectroscopy

Sina Dadgar
University of Arkansas, Fayetteville

Understanding Radiation Resistance in Head and Neck Tumor Xenografts Using Diffuse
Reflectance and Raman Spectroscopy

A dissertation submitted in partial fulfilment
of the requirements for the degree of
Doctor of Philosophy in Biomedical Engineering

by

Sina Dadgar
Azad University of Miyaneh
Bachelor of Science in Electrical Engineering, 2012
Bahçeşehir University
Master of Science in Electrical Engineering, 2014

December 2020
University of Arkansas

This dissertation is approved for recommendation to the Graduate Council.

_____
Narasimhan Rajaram, Ph.D.
Dissertation Director

_____   _____
Timothy J. Muldoon, Ph.D.   Kyle P. Quinn, Ph.D.
Committee Member   Committee Member

_____
Magda O. El-Shenawee, Ph.D.
Committee Member

Abstract

Each year, 800,000 new patients are diagnosed with head and neck squamous cell carcinoma (HNSCC), a majority of whom are treated with a combination of daily fractions of radiation and weekly chemotherapy sessions for up to seven weeks. Current methods to evaluate treatment response of individual patients are limited to anatomical measurements of tumor burden using CT scan or MRI 4-8 weeks after completion of treatment. However, earlier knowledge of radiation-response prior to or at early days after commencement of therapy can aid oncologist with escalating and de-escalating treatment plans for exceptionally non-responding and responding patients. Such a knowledge can be only be gained if proper understanding of radiation-induced physiological and biomolecular changes is established and associated with treatment response.

This dissertation presents two quantitative optical spectroscopic methods that can provide snapshots of tumor physiology and biomolecular content which can be used as biomarkers of treatment response. Because tumor hypoxia has been linked to poor treatment outcome, we employed diffuse reflectance spectroscopy to measure vascular oxygen saturation. In chapter 2, we first investigated the sensitivity of diffuse reflectance spectroscopy to tumor hypoxia and determined that optical measurement of tumor vascular oxygen saturation is negatively correlated with tumor hypoxia. In chapter 3, we utilized this technique to study radiation-induced kinetics of tumor oxygenation among radiation-resistant and -sensitive tumors. We established tumor xenografts from two human head and neck cancer cell lines in mice which were treated with 4 doses of 2 Gy twice weekly for two weeks. We observed greater rate of reoxygenation in radiation-resistant tumors which was accompanied with greater content of hypoxia inducible factor-1α (HIF-1α). Our results indicate that reduced oxygen consumption rate can potentially play a significant role in promoting radiation resistance. In addition, the radiation-induced changes in tumor optical properties were used to train a logistic regression model which successfully differentiated local-control and treatment-failure tumors.

In addition to changes in reoxygenation, radiation treatment has also been known to induce microenvironmental changes within tumor. Thus in chapter 4, we used Raman spectroscopy to investigate early radiation-induced biomolecular changes in tumor microenvironment of radiation-resistant and -sensitive tumors. Raman spectra of head and neck tumor xenografts 1, 24, and 48 hours after radiation was collected and the spectra were analyzed using multivariate curve resolution-alternating least squares (MCR-ALS) and pure spectral profiles of biological specimen were extracted. We observed higher contributions to Raman spectra from lipid- and collagen-like species respectively in radiation-sensitive and -resistant tumors. Our results indicate the sensitivity of Raman spectroscopy to radiation-induced microenvironmental changes at early time points after radiation. The association between the observed functional and biomolecular changes with the radiosensitivity of the utilized tumors motivate further clinical studies to investigate whether such changes can be used as potential biomarkers of radiation response.

Acknowledgment

First and foremost, I would like to thank Dr. Narasimhan Rajaram, for his continuous support, encouragement, and mentorship throughout my graduate school years. He gave me the opportunity to start, grow, and thrive and this dissertation would not have been completed without the guidance and wisdom I received from him.

I would also like to thank Drs. Timothy J. Muldoon, Kyle P. Quinn, and Magda O. El-Shenawee for their constructive criticism and insightful feedback. In addition to my academic committee advisers, I received guidance and support from Mr. Eric R. Siegel, Drs. Robert J. Griffin, Ruud P.M. Dings, and Santosh Paidi.

To my fellow lab members that I closely worked with: thank you for your collaboration, friendship, and support; this journey would have been boring without you. Former students of our laboratory, Daria Semeniak, Kinan Alhallak, and Dr. David Lee have played significant roles in conceptualization of the studies laid out in this work. Very special thanks to Joel Rodriguez Troncoso who was always available and assisted me with all my experiments.

Words cannot describe the love I received from my family. Zhale, Mortaza, Saman, Marziyeh, Parmis, Jesus, Lauras, Pablo, and Jahangir: you all believed in me even when I doubted myself.

Sandra, thank you for everything.

Dedication

To Kamuran Kadipaşaoğlu

Table of content

List of published papers

1. Dadgar, S., Troncoso, J. R. & Rajaram, N. Optical spectroscopic sensing of tumor hypoxia. J. Biomed. Opt. 23, 1–10 (2018), chapter 2 of this dissertation.

2. Dadgar, S., Troncoso, J. R., Siegel, E. R., Curry, N. M., Griffin, R. J., Dings, R. P. M. & Rajaram, N. Spectroscopic investigation of radiation-induced reoxygenation in radiation-resistant tumors. Neoplasia 23, 49–57 (2021), chapter 3 of this dissertation.

List of figures

Chapter 4

Chapter 5

List of tables

Chapter 1: Introduction

Introduction to head and neck cancer

Head and neck cancers encompass cancers of the oral and nasal cavity, pharynx, and larynx. Because majority of head and neck cancer originate in epithelial layer of mucosal tissue, the malignancy is typically referred to as head and neck squamous cell carcinoma (HNSCC)[1]. Repeated tobacco exposure and alcohol dependence are known to be substantial non-intrinsic risk factors for HNSCC[2]. However, oncogenic viruses, such as human papillomavirus (HPV), also play significant role in development of HNSCC[3]. Regardless, HNSCC is the sixth most common cancer type with an annual ~800,000 new cases and ~400,000 deaths worldwide[4] with 5th lowest 5-year survival rate of 65%. Over the past few decades HNSCC incidence has slightly reduced primarily due to reduction in tobacco consumption and better patient management[5]. However, the annual economic toll of HNSCC to U.S. economy is $14 billion with a median total cost of $80,000 per person[6,7]. Because of the high cost of cancer treatment, prevention, early detection, and treatment response identification become more cost-effective, and potentially life-saving strategies.

Cancer staging

According to American Joint Committee on Cancer (AJCC), cancer staging is based on three factors – Tumor size and location, the extent of lymph Node involvement, and the degree of Metastatic spread (TNM)[8]. Using TNM criteria, head and neck cancer is usually classified into one of four major categories. Stage I cancers refer to primary tumors that are 2 cm or smaller and remain in their original location. Stage II cancers are 2-4 cm and have not invaded nearby tissues, lymph nodes, or distant sites. Stage III cancer, however, refers to tumors larger than 4 cm or tumors smaller than 3 cm that have reached one lymph node. Finally, stage IV cancer can be defined as tumors that have invaded the nearby tissue, have spread to one or more lymph nodes, or to distant sites.

Stage I and II HNSCC patients are usually treated with surgery or radiation therapy. Although tumor location can influence the choice of treatment, surgery is preferred at early stages because it can avoid the toxic side effects of radiation[1]. Nevertheless, radiation treatment alone can also be used as the sole strategy in combating stage I and II cancers. Using advanced intensity-modulated radiation therapy that optimizes delivery of radiation to specific volumes, radiation exposure to adjacent tissue can be minimized and toxic side effects on normal tissue can be avoided[9]. Radiation for early stage cancer patients is usually delivered in daily fractions of 2.5 Gy for 6-7 weeks and has been shown to lead to promising results with no major toxic side effects[10]. These treatment strategies in ~80% of early-stage cancer patients lead to complete tumor remission.

However, locally advanced cancers (III and IV) are concurrently treated with daily fractions of 2 Gy radiation combined with weekly doses of chemotherapy[11]. Cisplatin and Cetuximab are widely combined with radiation-therapy for treatment of late stage HNSCC and have been shown have similar and promising results in treatment of late stage HNSCC patients[12]. In patients with resectable tumors, concurrent radiation and chemotherapy regimen is administered after surgery. Nevertheless about 50% of patients with late stage disease experience locoregional recurrence (III and IV)[13,14].

Current clinical standard of care

Retrospective clinical studies have shown that Human Papilloma Virus (HPV) status is a good indicator of prognosis, treatment response, and overall survival in HNSCC patients because HPV+ patients show significantly better survival and response to radiation compared with HPV-negative patients[15]. Thus, for early stage HNSCC patients, endoscopic guided biopsy is routinely performed with the goal of identifying HPV status of tumor, determining its radiosensitivity, and deciding best treatment strategies (radiation or surgery). However, for late-stage cancer patients,

biopsies are not usually performed. Because in late-stage, cancer has already spread to nearby tissue or distant site hence, treatment options become limited and patients undergo aggressive treatment plans with the aim of halting tumor growth and spread. Furthermore, despite being prognostically important, knowledge about HPV status does not lead to undertaking different treatment approaches[16]. Thus, HPV status is not currently considered in treatment planning of late-stage head and neck cancer patients.

Thus, current response evaluation metrics heavily rely on anatomical measurements of tumor burden. In 2000, the National Cancer Institute in collaboration with several other international organizations published a set of criteria that are used to evaluate a cancer patient's response to given treatment. Response evaluation criteria in solid tumors (RECIST) classifies treatment outcomes to three main categories: complete response (CR) in which entire target lesion disappears, partial response (PR) in which the longest diameter of target lesions have decreased 30% or more, and progressive diseases (PD) in which the target lesion has experienced a 20% or greater increase in the longest diameter of the target lesion[17]. A fourth category, stable disease (SD) also exists in which neither sufficient reduction or increase in the longest diameter is observed to qualify for PR or PD. The RECIST guidelines utilize tumor growth delay assay to monitor tumor burden regression by radiographic imaging as an important factor in response evaluation of individual patients[18]. In particular, computed tomography (CT) and magnetic resonance imaging (MRI) are used to determine tumor response 6-8 weeks after completion of treatment[19]. These findings are usually confirmed with positron emission tomography (PET) imaging of [^{18}F]-Fluorodeoxyglucose (FDG) uptake several weeks later to avoid high false-positive rate because tracer delivery and uptake can be affected by the post-radiation tumor microenvironment[20]. Although radiographic imaging 6-8 weeks after treatment can be useful in terms of establishing baseline measurements where future recurrence measurements can be compared against, it is a very late-stage measurements in terms of radiation response

evaluation and identification of responding and non-responding patients. Thus, no method can yet determine radiation response of the individual tumors either during or shortly after commencement of treatment. Therefore, patients continue to undergo and complete treatment plan without proper knowledge about treatment efficacy. Information about treatment response either prior to or shortly after commencement of therapy could potentially help oncologists tailor treatment plan for individual patients. However, such a knowledge can be gained by having profound understanding about the underlying physiological and biomolecular events that shape radioresistant phenotype.

Consequence of radiation therapy on cancer cells

Ionizing radiation produces free radicals in cells either directly in the DNA or indirectly in other molecules, primarily water (H_2O). These radiation-induced free radicals, in the presence of O_2, can generate peroxy radicals (DNA-OO·) capable of breaking chemical bonds and initiating a series of events which lead to DNA modification, and cell death (damage fixation). In contrast, lack of O_2 leads to the reduction of free radicals in DNA and restoration of the original form of DNA (DNA-H) leading to cancer cell survival[21–23]. Landmark studies in clinical head and neck cancer and soft-tissue sarcoma have found that pre-treatment oxygenation levels were predictive of treatment response and disease-free survival[24–26]. This important role of oxygen is the rationale for fractionated radiation therapy (2 Gy/day for 6–7 weeks), which is believed to re-oxygenate and radio-sensitize former hypoxic cells and hence, cause cell death via damage fixation[27–29].

Hypoxia and its role in radiation resistance

In 1955, Thomlinson and Gray observed uniform distribution of necrotic cells 100-150 μm away from blood vessels in human tumors and determined that this distance was equivalent to the diffusion limit of oxygen. They reasoned that these cancer cells had become necrotic because of the physical distance between them and nearest blood vessels and virtually no oxygen was available for their respiration. Thus, they postulated that viable cells located between the blood

vessels and the necrotic region had a gradual falling gradient in oxygen tension that caused them to become hypoxic[30]. The concentration of oxygen dissolved in tissue at the time of radiation has previously been shown to play an important factor during radiation because hypoxia protects cancer cells from toxic effects of ionizing radiation[23]. These landmark findings led to initiation of multiple clinical trials where patients breathed hyperbaric oxygen while undergoing radiotherapy. It was rationalized that hyperbaric oxygen breathing can enhance amount of oxygen dissolved in plasma and hence, increase tumor oxygen tension and therefore eliminate the problem of hypoxia. However, these clinical trials were not universally successful[31] as it later became known that in addition to chronic hypoxia, other factors including low vascular density and high oxygen consumption rate can also contribute to tumor hypoxia which cannot be eliminated by greater oxygen delivery[32]. For the past few decades, hypoxia has primarily been measured by hypoxia-visualizing markers such as 2-nitroimidazoles. When partial pressure of oxygen < 10 mmHg, these markers are typically metabolized in biological tissue by undergoing electron reduction and binding to macromolecules which can then be detected by immunohistochemical antibodies[33]. Another technique that enables quantitative determination of hypoxia is oxygen sensing microelectrodes, which if mounted on the tip of a surgical needle and inserted through the tumor, can determine partial pressure of oxygen[34]. Polarographic needles have widely been used in preclinical and clinical studies and have provided a wealth of knowledge about hypoxia and its relevance to deficient disease-free survival in HNSCC patients[26,35–38]. In addition to being implicated to poor radiation outcome, hypoxia also enhances metastatic potential[39]. In addition, hypoxia leads to stabilization of transcription factor hypoxia inducible factor-1 (HIF-1)[40]. While HIF-1 expression is inhibited under oxygenated conditions via prolyl hydroxylases (PHDs), its transcription is significantly upregulated under hypoxic conditions[22,41,42]. HIF-1 significantly contributes to tumor aggression and progression by upregulating angiogenic genes, switching to anerobic metabolism, and protecting cancer cells from oxidative stress[43]. However, both hypoxia

markers and pO_2 measurements are invasive and not amenable to repeated *in vivo* measurements.

In contrast, optical spectroscopy can be used as an alternative to traditional methods of tumor measurement. Optical spectroscopy is a fiber-based approach using non-ionizing radiation to non-destructively and non-invasively examine tissue of interest. Their low cost and small footprint make optical spectroscopy methods an excellent tool for conducting pilot studies in animal models of cancer and in humans. Since optical measurements using the fiber optic probe are non-invasive or minimally invasive (depending on the tissue site), the same subject can be monitored multiple times a day or over weeks to evaluate response to treatment. In addition to its obvious benefits as a clinical adjunct to existing clinical imaging modalities that cannot be used every day on patients, optical spectroscopy obviates the need for sacrificing large numbers of animals at several time points in longitudinal studies to evaluate treatment response.

Optical biopsy of head and neck cancer

Surgical tumor resection is a standard treatment option for early-stage head and neck cancer patients. However, adequate discrimination between tumor and normal adjacent tissue remains challenging. Current technologies in clinical environment cannot detect cancer cells and hence, inspection is limited to visual appearance and palpation of tumor by the trained surgeon. This has led to poor surgical success because cancerous cell residuals are left out due to incomplete tumor resection in oral cancer patients[44]. Thus, several studies have investigated the potential of optical biopsy for real-time guidance of surgeons during intraoperative cancer resection.

One such optical biopsy can be collected using *in vivo* measurements of intrinsic fluorescence spectroscopy because it has been shown that compared to normal oral tissue, tumor lesions have lower green and higher red fluorescence[45]. Based on this premise, Muller *et al* compared *in vivo* intrinsic fluorescence spectra of normal and cancer sites in upper aero-digestive

6

tract of HNSCC patients. They identified biochemical and structural differences between these sites that were driven by collagen and nicotinamide adenine nucleotide (NAD)[46]. In a similar study, Roblyer *et al* utilized autofluorescence imaging coupled with objective image analysis and were able to accurately discriminate oral neoplasia from nonneoplastic tissue[46]. In addition to autofluorescence spectroscopy, diffuse reflectance spectroscopy (DRS) has also been utilized towards fulfilling this goal. Beumer *et al* used DRS in differentiating malignant and non-malignant head and neck cancer patients and identified significant differences driven by oxygenation of these two tumor types[47]. Hu *et al* used oxygen saturation, total hemoglobin concentration, and reduced scattering coefficient extracted from DRS measurements for comparing properties of malignant tumors from contra-lateral normal tissue and observed statistically significant differences between two sample types[48]. Several studies have also used Raman spectroscopy (RS) for such comparisons. On *ex vivo* tumor samples, Valdez *et al* identified different indexes of protein, phenylamine, and lipid between healthy tissue and oropharyngeal carcinoma[49]. Krishna *et al* used *in vivo* Raman spectra collected from lesions of oral cavity to develop multivariate statistical algorithm that was able to discriminate normal from abnormal spectra with 94% sensitivity and specificity[50]. Barroso *et al* studied the changes in concentration of water across the tumor border on tumor specimens freshly excised from oral cavity. They observed Raman spectra of water had a transition to lower concentrations in healthy surrounding tissue compared with high concentrations in tumor[51]. These studies show the premise of optical spectroscopic methods for guiding surgeons during intraoperative surgery with the goal of accurately differentiating cancerous lesions from normal surrounding tissue. More simple and inexpensive setups using fiber-optic microendoscopic systems have also been shown to lead to promising results. Muldoon *et al* used such a setup for comparing microendoscopic images of subcutaneous tumor model to their histopathological assesment[52]. Using nuclear to cytoplasmic ratio, they presented very similar results to histopathological gold-standard measurements. In a more recent study, the same group compared images of oral squamous cell carcinoma specimen acquired by high-

7

resolution microendoscopy to histopathological classification of neoplastic and non-neoplastic tissue and found average sensitivity and specificity of 82 and 84% respectively[53].

Although these studies present the potential of optical measurements in better diagnosis of head and neck tumors, translation of these methods to the clinic has been limited due to the ability of histopathology of tumor biopsies to provide accurate diagnoses. However, patients undergoing chemoradiation therapy rarely have tissue biopsied before or during therapy. Therefore, there is a critical and unmet clinical need for technologies to identify treatment response early during therapy. Given the established ability of optical spectroscopy for evaluating functional and biomolecular status of tissue and the lack of other standard clinical methods, such as imaging or biopsy, there is significant potential for successful translation of noninvasive optical methods to monitor radiation response in HNSCC. In this dissertation, we present two specific techniques - diffuse reflectance and Raman spectroscopy – to gain a better understanding of radioresistant phenotype and identify physiological and biomolecular differences among radiation-sensitive and -resistant tumors that can be exploited in the clinic.

Specific aims

The overall goal of this research is to identify biomarkers that can differentiate late-stage radiation-responsive and non-responsive patients prior to, or at early days after commencement of radiation-therapy. However, such an insight requires deeper understanding of underlying physiological and biomolecular events that shape radioresistant phenotype in a head and neck patients. This dissertation used two human head and neck cancer models (UM-SCC-22B and UM-SCC-47) with opposing radiosensitivity in studying physiological and biomolecular differences between two tumor types. These human-derived cancer cells were used to form murine tumor xenografts and were treated with small doses of radiation which mimics the employed dose in treatment of real head and neck cancer patients. First, we used diffuse reflectance spectroscopy (DRS) in studying physiological changes induced by radiation and whether these changes differed

among radiation-resistant and -sensitive tumors. Second, we used Raman spectroscopy (RS) in studying radiation-induced biomolecular changes in radiation-resistant and -sensitive tumors.

Before utilizing DRS measurements in studying radiation-response, we first sought to validate the sensitivity of DRS to different levels of oxygenation (Chapter 2). Next, we used DRS in studying differential radiation-induced reoxygenation kinetics of radiation-resistant and -sensitive tumors. Using extracted optical parameters, we trained a logistic regression model which accurately differentiated -radiation-resistant and -sensitive tumors (Chapter 3). Finally, we used RS to study innate and radiation-induced biomolecular differences in radiation-resistant and -sensitive tumors (Chapter 4). In addition to optical measurements in chapters 3 and 4, we also investigated the biological pathways that contributed to the observed reoxygenation and biomolecular changes. Finally, we performed a pilot clinical trial assessing feasibility of diffuse reflectance measurements in head and neck cancer patients with diseased tonsils. During the next 3 chapters, this dissertation investigates 3 specific aims outlined as below:

Specific Aim 1: Validate DRS-measured tumor vascular oxygen saturation sO$_2$ using immunohistochemically determined tumor hypoxic fraction.
Publications:

- Dadgar, S., Troncoso, J. R. & Rajaram, N. Optical spectroscopic sensing of tumor hypoxia. J. Biomed. Opt. 23, 1–10 (2018), chapter 2 of this dissertation.

Background: As mentioned previously, tumor hypoxia at the time of irradiation has been identified as a hallmark of poor response to radiation as patients with hypoxic tumors survive significantly shorter compared to patients with well-oxygenated tumors[24,25,35]. Thus for the past few decades, hypoxia visualizing markers[33,37] and tissue oxygen sensing microelectrodes[34–36] have extensively been utilized in measuring tumor hypoxia (or oxygenation) and its association in radiation-response of preclinical animal models and clinical human patients. However, histological assessment of hypoxia requires administration of hypoxia probes (e.g. pimonidazole

hydrochloride). In addition, microscopic visualization techniques are required for evaluation of extent of hypoxia which necessitates tumor biopsy or excision. On the other hand, pO_2 sensing microelectrodes require insertion into tumor thru needles which can distort tumor architecture. Thus, both methods preclude tumors from longitudinal studies because repeated and repetitive measurements of tumors is not feasible. In contrast, diffuse reflectance spectroscopy can measure vascular oxygen saturation *in vivo* and hence, can be used as a negative indicator of hypoxia. However, no study has yet investigated the association between optically determined-vascular oxygenation with gold standard methods of hypoxia determination, namely hypoxia sensing markers.

Objective: To compare optical measurements of tumor vascular oxygenation against immunohistochemical measures of hypoxia from histological slides collected at three different depths of tumor including a depth that corresponds to the penetration depth of our optical probe.

Hypothesis: Optically determined vascular oxygen saturation (sO_2) and total hemoglobin concentration (THb) will be negatively correlated with immunohistochemically determined tumor hypoxia. Specifically, we hypothesize very low values of sO_2 and THb to associate with highly hypoxic tumors and vice versa.

Significance: Non-invasive and *in vivo* measurement of tumor vascular oxygenation that is a negative indicator of tumor hypoxia can be an alternative approach for replacing hypoxia visualizing markers and tissue oxygen sensing microelectrodes. In addition to providing functional information about tumors, DRS is also capable of characterizing structural changes that occur in tumor microenvironment as tissue scattering has been shown to be a strong biomarker of cell necrosis[54]. This aim is investigated in chapter 2 of this dissertation.

Specific Aim 2: Investigate radiation-induced short and long-term changes in oxygen saturation in radiation-resistant and -sensitive head and neck tumor xenografts using diffuse reflectance spectroscopy.

Publications:

- Dadgar, S., Troncoso, J. R., Siegel, E. R., Curry, N. M., Griffin, R. J., Dings, R. P. M. & Rajaram, N. Spectroscopic investigation of radiation-induced reoxygenation in radiation-resistant tumors. Neoplasia 23, 49–57 (2021), chapter 3 of this dissertation.

Background:

Head and neck cancer patients diagnosed at late stage are usually treated with 1.8-2 Gy of radiation in daily basis for a period of 7 weeks. Dose fractionation is believed to lead to reoxygenation of former hypoxic cells and hence, increase in cell killing. Thus, phenomenon of reoxygenation can be used as a biomarker of radiation-response. Several studies have used diffuse reflectance approach in monitoring radiation-induced reoxygenation kinetic and its association with radiation response of preclinical animal models of head and neck cancer[55,56]. Although these studies established the sensitivity of DRS to radiation-induced reoxygenation and its association with radiation-response, it remains unclear whether diffuse reflectance spectroscopy is sensitive to functional changes that are induced by smaller doses of radiation.

Objective: To study short- and long-term reoxygenation kinetics induced by small doses of radiation and its differences among radiation-sensitive and -resistant tumors. We also sought to use the observed fold changes in training a logistic regression model to determine if we can accurately differentiate radiation-resistant and -sensitive tumors. Finally, we investigated the biological pathways that play important role in causing the observed reoxygenation in radiation-resistant and -sensitive tumors.

Hypothesis: Radiation-sensitive tumors will have a greater rate of reoxygenation in comparison to radiation-resistant tumors.

Significance: This work provides valuable information about differential functional changes within radiation-resistant and -sensitive tumor at early time points after treatment with low doses of radiation which are representative of utilized doses in treatment of head and neck cancer patients. Our findings illustrate the potential of this technique for clinical translation where treatment response of patients can be monitored. This aim is investigated in chapter 2 of this dissertation.

Specific Aim 3: Establish early radiation-induced biomolecular alterations in radiation-resistant and -sensitive head and neck tumor xenografts using Raman spectroscopy.

Background:

In addition to vascular changes, radiation can also induce biomolecular changes in tumor microenvironment which can be detected with Raman spectroscopy. Several studies have associated such biomolecular changes with radiation sensitivity of utilized cells and tumors[57–60]. However, such studies of radiation-induced biomolecular changes have been limited to *in vitro* cellular studies or excised tumors. No study has yet used *in vivo* Raman spectroscopy for monitoring differential biomolecular changes in radiation-resistant and -sensitive tumors.

Objective: To study radiation-induced biomolecular alterations in microenvironment of radiation-resistant and -sensitive tumors in early time points after radiation which can be combined with DRS measurements.

Significance: This work motivates the use of combined diffuse reflectance and Raman spectroscopy for longitudinal monitoring of tumor oxygenation and biomolecular content and their evolution in response to radiation in radiation-resistant and -sensitive tumors.

References

1.   Argiris, A., Karamouzis, M. V., Raben, D. & Ferris, R. L. Head and neck cancer. *The Lancet* (2008) doi:10.1016/S0140-6736(08)60728-X.

2.   Marur, S. & Forastiere, A. A. Head and Neck Squamous Cell Carcinoma: Update on Epidemiology, Diagnosis, and Treatment. *Mayo Clinic Proceedings* (2016) doi:10.1016/j.mayocp.2015.12.017.

3.   Steinberg, B. & DiLorenzo, T. A possible role for human papillomaviruses in head and neck cancer. *Cancer Metastasis Rev.* **15**, 91–112 (1996).

4.   Bray, F. *et al.* Global cancer statistics 2018: GLOBOCAN estimates of incidence and mortality worldwide for 36 cancers in 185 countries. *CA. Cancer J. Clin.* (2018) doi:10.3322/caac.21492.

5.   Sturgis, E. M. & Cinciripini, P. M. Trends in head and neck cancer incidence in relation to smoking prevalence: An emerging epidemic of human papillomavirus-associated cancers? *Cancer* (2007) doi:10.1002/cncr.22963.

6.   Yabroff, K. R., Lund, J., Kepka, D. & Mariotto, A. Economic burden of cancer in the United States: Estimates, projections, and future research. *Cancer Epidemiology Biomarkers and Prevention* (2011) doi:10.1158/1055-9965.EPI-11-0650.

7.   Wissinger, E., Griebsch, I., Lungershausen, J., Foster, T. & Pashos, C. L. The Economic Burden of Head and Neck Cancer: A Systematic Literature Review. *PharmacoEconomics* (2014) doi:10.1007/s40273-014-0169-3.

8.   Lydiatt, W. M. *et al.* Head and neck cancers-major changes in the American Joint Committee on cancer eighth edition cancer staging manual. *CA. Cancer J. Clin.* (2017) doi:10.3322/caac.21389.

9.   Eisbruch, A. *et al.* Recurrences near base of skull after IMRT for head-and-neck cancer: Implications for target delineation in high neck and for parotid gland sparing. *Int. J. Radiat. Oncol. Biol. Phys.* (2004) doi:10.1016/j.ijrobp.2003.10.032.

10.   Le, Q. T. X. *et al.* Influence of fraction size, total dose, and overall time on local control of T1-T2 glottic carcinoma. *Int. J. Radiat. Oncol. Biol. Phys.* (1997) doi:10.1016/S0360-3016(97)00284-8.

11.   Vokes, E. E. & Weichselbaum, R. R. Concomitant chemoradiotherapy: Rationale and clinical experience in patients with solid tumors. *Journal of Clinical Oncology* (1990) doi:10.1200/JCO.1990.8.5.911.

12.   Magrini, S. M. *et al.* Cetuximab and radiotherapy versus cisplatin and radiotherapy for locally advanced head and neck cancer: A randomized phase II trial. *J. Clin. Oncol.* (2016) doi:10.1200/JCO.2015.63.1671.

13.   Brockstein, B. *et al.* Patterns of failure, prognostic factors and survival in locoregionally advanced head and neck cancer treated with concomitant chemoradiotherapy: A 9-year, 337-patient, multi-institutional experience. *Ann. Oncol.* (2004)

doi:10.1093/annonc/mdh308.

14.	Leeman, J. E. *et al.* Patterns of treatment failure and postrecurrence outcomes among patients with locally advanced head and neck squamous cell carcinoma after chemoradiotherapy using modern radiation techniques. *JAMA Oncol.* (2017) doi:10.1001/jamaoncol.2017.0973.

15.	Fakhry, C. *et al.* Improved survival of patients with human papillomavirus-positive head and neck squamous cell carcinoma in a prospective clinical trial. *J. Natl. Cancer Inst.* (2008) doi:10.1093/jnci/djn011.

16.	Pfister, D. G. *et al.* Head and neck cancers: Clinical practice guidelines in oncology. *JNCCN Journal of the National Comprehensive Cancer Network* (2011) doi:10.6004/jnccn.2011.0053.

17.	Eisenhauer, E. A. *et al.* New response evaluation criteria in solid tumours: Revised RECIST guideline (version 1.1). *Eur. J. Cancer* (2009) doi:10.1016/j.ejca.2008.10.026.

18.	Passero, V. A. *et al.* Response assessment by combined PET-CT scan versus ct scan alone using RECIST in patients with locally advanced head and neck cancer treated with chemoradiotherapy. *Ann. Oncol.* (2010) doi:10.1093/annonc/mdq226.

19.	Saito, N. *et al.* Posttreatment CT and MR imaging in head and neck cancer: What the radiologist needs to know. *Radiographics* (2012) doi:10.1148/rg.325115160.

20.	de Bree, R. *et al.* Detection of locoregional recurrent head and neck cancer after (chemo)radiotherapy using modern imaging. *Oral Oncology* (2009) doi:10.1016/j.oraloncology.2008.10.015.

21.	Bertout, J. A., Patel, S. A. & Simon, M. C. The impact of O2 availability on human cancer. *Nat. Rev. Cancer* **8**, 967–975 (2008).

22.	Brown, J. M. Tumor Hypoxia in Cancer Therapy. *Methods Enzymol.* **435**, 297–321 (2007).

23.	Gray, L. H., Conger, A. D., Ebert, M., Hornsey, S. & Scott, O. C. The concentration of oxygen dissolved in tissues at the time of irradiation as a factor in radiotherapy. *Br. J. Radiol.* **26**, 638–648 (1953).

24.	Brizel, D. M. *et al.* Tumor oxygenation predicts for the likelihood of distant metastases in human soft tissue sarcoma. *Cancer Res.* **56**, 941–943 (1996).

25.	Nordsmark, M., Overgaard, M. & Overgaard, J. Pretreatment oxygenation predicts radiation response in advanced squamous cell carcinoma of the head and neck. *Radiother. Oncol.* **41**, 31–9 (1996).

26.	Brizel, D. M., Dodge, R. K., Clough, R. W. & Dewhirst, M. W. Oxygenation of head and neck cancer: Changes during radiotherapy and impact on treatment outcome. *Radiother. Oncol.* **53**, 113–117 (1999).

27.	Fowler, J. The rational of dose fractionation. The Relationship of Time and Dose in the Radiation Therapy of Cancer. in 6–23 (Karger Publishers, 1969).

28. Kallman, R. F. The Phenomenon of Reoxygenation and Its Implications for Fractionated Radiotherapy. *Radiology* **105**, 135–42 (1972).

29. Withers, H. R. The 4 Rs of radiotherapy. *Adv. Radiat. Biol.* **5**, 241–271 (1975).

30. Thomlinson, R. H. & Gray, L. H. The histological structure of some human lung cancers and the possible implications for radiotherapy. *Br. J. Cancer* **9**, 539–549 (1955).

31. Moen, I. & Stuhr, L. E. B. Hyperbaric oxygen therapy and cancer - A review. *Targeted Oncology* (2012) doi:10.1007/s11523-012-0233-x.

32. Dewhirst, M. W., Cao, Y. & Moeller, B. Cycling hypoxia and free radicals regulate angiogenesis and radiotherapy response. *Nature Reviews Cancer* (2008) doi:10.1038/nrc2397.

33. Raleigh, J. A., Dewhirst, M. W. & Thrall, D. E. Measuring tumor hypoxia. *Semin. Radiat. Oncol.* (1996) doi:10.1016/S1053-4296(96)80034-8.

34. Vaupel, P., Höckel, M. & Mayer, A. Detection and characterization of tumor hypoxia using pO2 histography. *Antioxidants and Redox Signaling* (2007) doi:10.1089/ars.2007.1628.

35. Nordsmark, M. *et al.* Prognostic value of tumor oxygenation in 397 head and neck tumors after primary radiation therapy. An international multi-center study. *Radiother. Oncol.* (2005) doi:10.1016/j.radonc.2005.06.038.

36. Rudat, V. *et al.* Predictive value of the tumor oxygenation by means of pO2histography in patients with advanced head and neck cancer. *Strahlentherapie und Onkol.* (2001) doi:10.1007/PL00002427.

37. Raleigh, J. A., Chou, S. C., Arteel, G. E. & Horsman, M. R. Comparisons among pimonidazole binding, oxygen electrode measurements, and radiation response in C3H mouse tumors. *Radiat. Res.* **151**, 580–589 (1999).

38. Nordsmark, M. *et al.* Measurements of hypoxia using pimonidazole and polarographic oxygen-sensitive electrodes in human cervix carcinomas. *Radiother. Oncol.* **67**, 35–44 (2003).

39. Le, Q. T., Denko, N. C. & Giaccia, A. J. Hypoxic gene expression and metastasis. *Cancer and Metastasis Reviews* (2004) doi:10.1023/B:CANC.0000031768.89246.d7.

40. Wang, G. L. & Semenza, G. L. General involvement of hypoxia-inducible factor 1 in transcriptional response to hypoxia. *Proc. Natl. Acad. Sci. U. S. A.* **90**, 4304–8 (1993).

41. Balamurugan, K. HIF-1 at the crossroads of hypoxia, inflammation, and cancer. *Int. J. Cancer* **138**, 1058–66 (2016).

42. Semenza, G. L. Targeting HIF-1 for cancer therapy. *Nat. Rev. Cancer* **3**, 721–32 (2003).

43. Moeller, B. J., Cao, Y., Li, C. Y. & Dewhirst, M. W. Radiation activates HIF-1 to regulate vascular radiosensitivity in tumors: Role of reoxygenation, free radicals, and stress

granules. *Cancer Cell* **5**, 429–41 (2004).

44.   Smits, R. W. H. *et al.* Resection margins in oral cancer surgery: Room for improvement. *Head Neck* (2016) doi:10.1002/hed.24075.

45.   Lane, P. M. *et al.* Simple device for the direct visualization of oral-cavity tissue fluorescence. *J. Biomed. Opt.* (2006) doi:10.1117/1.2193157.

46.   Roblyer, D. *et al.* Objective detection and delineation of oral neoplasia using autofluorescence imaging. *Cancer Prev. Res.* (2009) doi:10.1158/1940-6207.CAPR-08-0229.

47.   Beumer, H. W. *et al.* Detection of squamous cell carcinoma and corresponding biomarkers using optical spectroscopy. *Otolaryngol. - Head Neck Surg.* (2011) doi:10.1177/0194599810394290.

48.   Hu, F. *et al.* Assessment of the sensitivity and specificity of tissue-specific-based and anatomical-based optical biomarkers for rapid detection of human head and neck squamous cell carcinoma. *Oral Oncol.* (2014) doi:10.1016/j.oraloncology.2014.06.015.

49.   Valdés, R., Stefanov, S., Chiussi, S., Lõpez-Alvarez, M. & González, P. Pilot research on the evaluation and detection of head and neck squamous cell carcinoma by Raman spectroscopy. in *Journal of Raman Spectroscopy* (2014). doi:10.1002/jrs.4498.

50.   Krishna, H., Majumder, S. K., Chaturvedi, P., Sidramesh, M. & Gupta, P. K. In vivo Raman spectroscopy for detection of oral neoplasia: A pilot clinical study. *J. Biophotonics* **7**, 690–702 (2014).

51.   Barroso, E. M. *et al.* Water concentration analysis by Raman spectroscopy to determine the location of the tumor border in oral cancer surgery. *Cancer Res.* (2016) doi:10.1158/0008-5472.CAN-16-1227.

52.   Muldoon, T. J. *et al.* Subcellular-resolution molecular imaging within living tissue by fiber microendoscopy. *Opt. Express* (2007) doi:10.1364/oe.15.016413.

53.   Muldoon, T. J. *et al.* Noninvasive imaging of oral neoplasia with a high-resolution fiber-optic microendoscope. *Head Neck* (2012) doi:10.1002/hed.21735.

54.   Vishwanath, K., Yuan, H., Barry, W. T., Dewhirst, M. W. & Ramanujam, N. Using Optical Spectroscopy to Longitudinally Monitor Physiological Changes within Solid Tumors. *Neoplasia* **11**, 889–900 (2009).

55.   Vishwanath, K. *et al.* Quantitative optical spectroscopy can identify long-term local tumor control in irradiated murine head and neck xenografts. *J. Biomed. Opt.* **14**, 054051 (2009).

56.   Hu, F. *et al.* Oxygen and Perfusion Kinetics in Response to Fractionated Radiation Therapy in FaDu Head and Neck Cancer Xenografts Are Related to Treatment Outcome. *Int. J. Radiat. Oncol. Biol. Phys.* **96**, 462–9 (2016).

57.   Yasser, M., Shaikh, R., Chilakapati, M. K. & Teni, T. Raman spectroscopic study of radioresistant oral cancer sublines established by fractionated ionizing radiation. *PLoS One*

9, e97777 (2014).

58. Matthews, Q. *et al.* Radiation-induced glycogen accumulation detected by single cell raman spectroscopy is associated with radioresistance that can be reversed by metformin. *PLoS One* **10**, e0135356 (2015).

59. Harder, S. J. *et al.* Raman spectroscopy identifies radiation response in human non-small cell lung cancer xenografts. *Sci. Rep.* **6**, 21006 (2016).

60. Van Nest, S. J. *et al.* Raman Spectroscopic Signatures Reveal Distinct Biochemical and Temporal Changes in Irradiated Human Breast Adenocarcinoma Xenografts. *Radiat. Res.* **189**, 497–504 (2018).

Chapter 2: Optical spectroscopic sensing of tumor hypoxia

<u>Introduction</u>

Low oxygen tension or hypoxia is caused by the imbalance between oxygen delivery and consumption[1–4]. Hypoxia is typically defined at the cellular level as oxygen tension (pO_2) < 10 mmHg. Oxygen-sensing Clark microelectrodes have established a wealth of knowledge related to hypoxia and its role in poor disease-free survival[5–7]. These electrodes provide a direct measure of pO_2 and hence hypoxia in tissue. To measure oxygen tension *in vivo*, the electrode is inserted into tissue to a certain depth and retracted along tracks to provide pO_2 measurements at several points along these tracks. Such measurements of hypoxia have been associated with tumor aggressiveness, resistance to chemotherapy and radiation therapy[4,8–11], and shown to be predictive of tumor metastases in soft tissue sarcoma[12]. It has also been reported that local recurrences have a higher hypoxic fraction (HF) than primary tumors[13,14]. These studies have demonstrated that measuring tumor oxygenation either prior to or during therapy could aid in the selection of appropriate treatment regimens for patients. However, microelectrode-based pO_2 measurements are always invasive (requiring tumor penetration), limited to only accessible organs, can potentially modify the tumor microenvironment, and are not amenable to repeated measurements *in vivo*. A combination of pulsed electron paramagnetic resonance imaging and magnetic resonance imaging has been shown to provide quantitative three-dimensional maps of tumor pO_2 co-registered with anatomical detail in preclinical animal models[15]. Other than an intravenous injection of the triarylmethyl radical (TAM) probe used to sense oxygen, this technology would allow noninvasive and repeated imaging of pO_2 *in vivo*. However, the instrumentation in its current form presents a challenge to clinical translation.

Other established methods to measure tumor hypoxia include the use of pimonidazole[6,7,16,17] and EF5[18], two widely used markers that provide quantitative measures of tumor hypoxia. Both pimonidazole and EF5 accumulate by forming adducts with thiol groups

present in proteins in hypoxic cells. Pimonidazole accumulates in cells with $pO_2 < 10$ mmHg and has been used extensively to map hypoxic regions in excised tumors in animal models. EF5 has been demonstrated in both animal and human studies (using a fluorinated form of EF5) and can be calibrated to provide information about both location and level of hypoxia[19]. Since quantification using these markers requires either tumor excision after administration or the use of radioisotopes for *in vivo* labeling, it precludes their use in longitudinal animal and human studies, where tumor oxygenation could potentially be used as a biomarker of treatment response or local recurrence.

For accessible tumors of the skin and oral cavity, optical fiber-based diffuse reflectance spectroscopy (DRS) can provide a nondestructive and noninvasive alternative to the microelectrode for quantitatively evaluating tumor oxygenation. The tissue of interest is illuminated with visible light from a broadband source (400 to 650 nm) and the reflected light is used to quantify the underlying scatterers and absorbers, a combination of which is used for recognition of tissue pathology. Tumor vascular oxygenation (sO_2) can be quantified by measuring the individual contributions of oxygenated (HbO_2) and deoxygenated (dHb) hemoglobin within the blood vessels. Thus, DRS provides an indirect measure of tissue pO_2 by quantifying the "supply"— oxygenation levels in the vasculature using sO_2 and perfusion levels using total hemoglobin concentration (HbO_2 + dHb). DRS has previously been used to measure tumor oxygenation in small animal model studies to determine treatment response. Vishwanath *et al* found that longitudinal changes in dHb, as quantified by DRS, after treatment with doxorubicin were concordant with changes in tumor HF[20]. Palmer *et al* demonstrated that DRS-based measurements of sO_2 were more stable compared with microelectrode-based measurements of pO_2; furthermore, the direction of change of sO_2 in response to perturbations in the composition of inhaled air in mice was concordant with pO_2 measurements[21]. This study builds upon these previous reports to validate DRS measures of sO_2 using pimonidazole based quantification of tumor HF in two human head and neck cancer cell-based xenografts. In addition to evaluating HF at a depth corresponding to the sampling depth of our probe, we also determined the HF at two

other depths within excised tissue and compared these measurements to sO_2. Our results indicate that DRS-based measurements of sO_2 can provide reliable estimates and thus enable longitudinal tracking of tumor HF in studies, where tumor hypoxia can be a significant biomarker of treatment response.

Materials and Methods

Cell culture and tumor xenografts

All studies and protocols were approved by the Institutional Animal Care & Use Committee (IACUC) of University of Arkansas. Twenty nude mice were housed at the Central Laboratory Animal Facility (CLAF). Mice were maintained under standard 12-h light/dark cycles with ad libitum access to food and water. Mice were subcutaneously injected with either UM-SCC-47 (n = 10) or UM-SCC-22B (n = 10) human head and neck cancer cells. Cells were cultured in a mixture of Dulbecco's modified Eagle medium, 10% fetal bovine serum, 1% Penicillin–Streptomycin, 1% nonessential amino acids, and 1% L-glutamine. Head and neck tumor xenografts were formed by injecting 1.5 million cells suspended in 1:1 mixture of Matrigel (Corning, New York) and saline into the right flank of these animals. When tumor volumes reached 1500 mm^3, mice received an intraperitoneal injection of pimonidazole (at a dose of 60 mg/kg). An hour post injection, the animals were anesthetized by breathing 1.5% isoflurane (mixed with oxygen) and diffuse reflectance spectra were acquired from each tumor. Immediately after DRS measurements, the tumors were resected (with skin) and snap-frozen for histology.

Diffuse reflectance spectroscopy

Figure 1(a) presents our DRS setup. This simple and portable system consists of a halogen lamp (HL-2000, Ocean Optics, Dunedin, Florida) for illumination, a USB spectrometer (Flame, Ocean Optics) for spectral acquisition, and a bifurcated optical probe for light delivery and collection. DRS spectra were acquired in the wavelength range of 475 to 600 nm. The common end of the probe is illustrated in Figure 1(b) and consists of four illumination fibers and

five detector fibers located at a source–detector separation distance (SDSD) of 2.25 mm. Based on previously described methods, we determined the sampling depth of this SDSD to be ~1.8 mm[22]. Reflected light spectra were collected using this system with an integration time of 100 ms. Spectral acquisition was simplified with the use of a foot pedal controlled by custom LabVIEW (National Instruments, Austin, Texas) software. With the exception of three tumors on which multiple spectra were recorded, only one spectrum was measured from each tumor. For tumors with multiple spectra, averaged optical properties were used to represent that tumor. Spectra acquired from tissues were background-subtracted to correct for dark current and ambient light. To calibrate for light throughput, the background-subtracted reflected light intensity from tissue was divided by background-subtracted reflected light intensity from an 80% reflectance standard (SRS-80-010; Labsphere, North Sutton, New Hampshire).

Quantification of tissue optical properties

We used a lookup table (LUT)-based model to fit the acquired DRS spectra and extract wavelength-dependent absorption and scattering properties from tissue. The LUT-based model has been described in detail previously[23] and validated for a range of SDSD[22]. Briefly, the LUT is generated from reflectance spectra acquired from a matrix of tissue-simulating phantoms of known absorption (μ_a) and scattering (μ_s') coefficients. These phantoms contained India ink (Salis International Inc., Golden, Colorado) and polystyrene microspheres beads (diameter = 1 μm; Polysciences, Warrington, Pennsylvania) of known concentrations dissolved in water to create a range of absorption and scattering coefficients, respectively. The LUT corresponding to the SDSD used in this study was validated using tissue-simulating phantoms and found to have errors of 9.5% and 1.5%, respectively, for quantifying μ_a and μ_s', respectively. To fit the model to the data, we constrained scattering to a power law dependence on wavelength and represented it by the equation: $\mu_s'(\lambda) = \mu_s'(\lambda_0) . \left(\frac{\lambda}{\lambda_0}\right)^{-B}$, where $\lambda_0 = 630$ nm. The absorption coefficient is computed as a linear sum of absorbers based on Beer–Lambert's law. Assuming the principal absorbers to be

HbO$_2$, dHb, and mouse skin, the absorption coefficient is given by : $\mu_a(\lambda) = [Hb]\big[\alpha\sigma_{HbO_2}(\lambda) + (1-\alpha)\sigma_{Hb}(\lambda)\big] + [C]skin(\lambda)$, where α is the vascular oxygenation and σ is the extinction coefficient of hemoglobin (oxygenated or deoxygenated). We have previously shown that the effects of pigment packaging, which describes the inhomogeneous distribution of hemoglobin within tissue, are minimal at wavelengths beyond 500 nm[24]. Therefore, we did not include a correction factor to account for pigment packaging.

Immunohistochemistry

All harvested tumors were sectioned using a Cryostat (CM 1860; Leica, Inc., Nussloch, Germany) to slices of 10 µm. Care was taken to slice the frozen tumors starting from the skin side, where the DRS measurements were initiated. Multiple slices were acquired from each tumor at depths corresponding to 0.8, 1.8, and 2.8 mm, with separate, sequential slices utilized for immunofluorescence and histology. All the collected samples were immunestained with a direct labeling protocol. First, the slides were hydrated in phosphate-buffered saline (PBS) and permeabilized with 0.1% Triton-X. Next, the slides were incubated with blocking solution (95% PBS, 4% goat serum, and 1% sodium azide) in room temperature for an hour and stained with mouse monoclonal antibody conjugated to Dylight™ 549 fluorophore (Hypoxyprobe Red549 kit; HPI, Inc., Burlington, Massachusetts) for an hour in a dark room. Finally, slides were rinsed with PBS, covered with fluoromount, and coverslipped with nail polish. Slides were dried for 24 h prior to imaging. All images were acquired using a 4× objective on a Nikon fluorescence microscope with same settings (binning, exposure time, and gain).

Quantification of hypoxic fraction and image analysis algorithm

Pimonidazole accumulates in tissue, where the intracellular oxygen level drops below 10 mmHg[25]. We analyzed all of the acquired immunofluorescence images using MATLAB (Mathworks; Natick, Massachusetts). At each depth within the tumor—0.8, 1.8, and 2.8 mm [Figure 2(a)]—immunofluorescence and histology (H&E-stained) images were acquired from

multiple fields of view from each tumor slice. For representative purposes alone, a fully stitched image of pimonidazole immunofluorescence is presented in Figure 2(b) along with its corresponding H&E image from an adjacent tumor slice. Each tumor slice consisted of an average of 15 fields of view (1.5 mm × 1.1 mm). We converted each individual image to its gray-scaled and normalized version and calculated a threshold using Otsu's method to segment out the pimonidazole- positive pixels[26]. Next, we averaged all thresholds to compute a global threshold. This global threshold was used to segment all of the images, and HF of each image was quantified as the ratio of hypoxic (segmented) pixels to the total number of tissue pixels. Figure 2(c) presents a flowchart of the image processing algorithm employed for this analysis. The average HF corresponding to each depth within a tumor is reported here.

Results and Discussion

Figure 3(a) presents DRS spectra and their corresponding LUT fits (red lines) for two different tumors that were excised at similar tumor volumes. Quantification of optical properties using the LUT fits identified different values of sO_2 for each tumor. This is evident in the wavelength-dependent absorption coefficients for each tumor, which demonstrate the classic double peaks of HbO_2 (542 and 577 nm) for the tumor with recovered sO_2 of 58%. On the other hand, the μ_a spectrum for the tumor with sO_2 of 15% indicates poor oxygenation with a single peak corresponding to dHb [Figure 3(b)]. IHC images of HF corresponding to both tumors illustrate that the tumor with higher sO_2 has a lower percentage of hypoxic tissue compared with the low-sO_2 tumor [Figure 3(c)].

We determined the association between the HF and the scattering and absorption properties of the UM-SCC-22B and UM-SCC-47 tumors. We found a statistically significant negative correlation (r = −0.50; p = 0.02) between the HF and sO_2 [Figure 4(a)]. We also observed similar statistically significant correlations of the HF with THb [Figure 4(b); r = −0.45; p = 0.04] and HbO_2 [Figure 4(c); r = −0.59; p = 0.006]. Taken together, these results indicate that measurements

of vascular sO_2 and THb can provide reliable estimates of the hypoxic state of tissue. Specifically, very low values of sO_2 and THb can point to highly hypoxic and poorly perfused tumor.

In addition to evaluating hemoglobin-based parameters, we determined the relationship between HF and the mean reduced scattering coefficient [Figure 4(d)]. We found a statistically significant positive correlation between the two parameters (r = 0.60; p = 0.005). Since all our tumors were excised at similar tumor volumes, this correlation is unlikely due to tumor volume. A previous study using optical spectroscopy by Vishwanath *et al* found a highly significant positive correlation between mean reduced scattering coefficient and tumor necrotic fraction[20]. Although we do not completely understand the relationship between HF and scattering in our study, it is possible that the highly hypoxic tumors also contained larger necrotic areas—the cellular and structural changes associated with tumor necrosis could potentially contribute to the increased scattering seen here[27,28]. Our future studies include plans to transiently modify tumor hypoxia levels[6] and measure the association between HF and tissue scattering and absorption. These studies could potentially shed further light on the basis for these interactions.

We also investigated the HF as a function of depth within each tumor. HF was calculated at additional depths of 0.8 and 2.8 mm from the surface of the tumor. For each tumor, the fold-change in HF at 1.8 and 2.8 mm was calculated with respect to the HF at 0.8 mm. Although we observed a trend toward increasing HF with depth, this was not statistically significant (Figure 5). These results are similar to a recent study using multispectral optoacoustic tomography on prostate cancer xenografts that found a well-oxygenated rim and a large decrease in oxygenation toward the tumor core[29]. Furthermore, we did not find statistically significant correlations between optical properties and HFs at depths of 0.8 and 2.8 mm (data not shown). Although tumor xenografts are typically considered to be homogeneous, it is interesting to note a lack of correlation at depths that do not lie within the range of sampling depths of the probe.

In summary, we have demonstrated that the vascular oxygenation and total hemoglobin concentration measured using DRS are concordant with measurements of HF and can provide

24

reliable indirect measures of tumor oxygenation. Monitoring changes in tumor oxygenation during therapy—radiation or chemo—can provide clinicians with a complementary aid to identify treatment response and provide opportunities to investigate hitherto unknown reoxygenation kinetics in preclinical animal models in response to clinically relevant treatment regimens.

References

1. Hockel, M. *et al.* Association between tumor hypoxia and malignant progression in advanced cancer of the uterine cervix. *Cancer Res.* **56**, 4509–4515 (1996).

2. Nordsmark, M. & Overgaard, J. A confirmatory prognostic study on oxygenation status and loco-regional control in advanced head and neck squamous cell carcinoma treated by radiation therapy. *Radiother. Oncol.* **57**, 39–43 (2000).

3. Hall, E. J. & Giaccia, A. J. *Radiobiology for the Radiologist. Lippinicoo Williams & Wilkins* vol. 7 Edition (2012).

4. Hockel, M. & Vaupel, P. Tumor Hypoxia: Definitions and Current Clinical, Biologic, and Molecular Aspects. *JNCI J. Natl. Cancer Inst.* **93**, 266–276 (2001).

5. Kavanagh, M. C. *et al.* A comparison in individual murine tumors of techniques for measuring oxygen levels. *Int. J. Radiat. Oncol. Biol. Phys.* **44**, 1137–46 (1999).

6. Raleigh, J. A., Chou, S. C., Arteel, G. E. & Horsman, M. R. Comparisons among pimonidazole binding, oxygen electrode measurements, and radiation response in C3H mouse tumors. *Radiat. Res.* **151**, 580–589 (1999).

7. Nordsmark, M. *et al.* Measurements of hypoxia using pimonidazole and polarographic oxygen-sensitive electrodes in human cervix carcinomas. *Radiother. Oncol.* **67**, 35–44 (2003).

8. Vaupel, P., Kelleher, D. K. & H[ouml]ckel, M. Oxygenation status of malignant tumors: Pathogenesis of hypoxia and significance for tumor therapy. *Semin. Oncol.* **28**, asonc02802f0029 (2001).

9. Gray, L. H., Conger, A. D., Ebert, M., Hornsey, S. & Scott, O. C. The concentration of oxygen dissolved in tissues at the time of irradiation as a factor in radiotherapy. *Br. J. Radiol.* **26**, 638–648 (1953).

10. Tannock, I. Response of aerobic and hypoxic cells in a solid tumor to adriamycin and cyclophosphamide and interaction of the drugs with radiation. *Cancer Res.* **42**, 4921–4926 (1982).

11. Brown, J. M. Tumor Hypoxia in Cancer Therapy. *Methods Enzymol.* **435**, 297–321 (2007).

12. Brizel, D. M. *et al.* Tumor oxygenation predicts for the likelihood of distant metastases in human soft tissue sarcoma. *Cancer Res.* **56**, 941–943 (1996).

13. Vaupel, P., Schlenger, K., Knoop, C. & Hockel, M. Oxygenation of human tumors: Evaluation of tissue oxygen distribution in breast cancers by computerized O2 tension measurements. *Cancer Res.* **51**, 3316–3322 (1991).

14. Schlenger, K. & Vaupel, P. Oxygenation of Carcinomas of the Uterine Cervix: Evaluation by Computerized O2 Tension Measurements. *Cancer Res.* **51**, 6098–6102 (1991).

15. Matsumoto, S. *et al.* Low-field paramagnetic resonance imaging of tumor oxygenation and

glycolytic activity in mice. *J. Clin. Invest.* **118**, 1965–73 (2008).

16. Varia, M. A. *et al.* Pimonidazole: A Novel Hypoxia Marker for Complementary Study of Tumor Hypoxia and Cell Proliferation in Cervical Carcinoma. *Gynecol. Oncol.* **71**, 270–277 (1998).

17. Raleigh, J. A. *et al.* Hypoxia and vascular endothelial growth factor expression in human squamous cell carcinomas using pimonidazole as a hypoxia marker. *Cancer Res.* **58**, 3765–8 (1998).

18. Evans, S. M. *et al.* Detection of hypoxia in human squamous cell carcinoma by EF5 binding. *Cancer Res.* **60**, 2018–2024 (2000).

19. Koch, C. J. [1] Measurement of absolute oxygen levels in cells and tissues using oxygen sensors and 2-nitroimidazole EF5. *Methods Enzymol.* **352**, 3–31 (2002).

20. Vishwanath, K., Yuan, H., Barry, W. T., Dewhirst, M. W. & Ramanujam, N. Using Optical Spectroscopy to Longitudinally Monitor Physiological Changes within Solid Tumors. *Neoplasia* **11**, 889–900 (2009).

21. Palmer, G. M. *et al.* Quantitative diffuse reflectance and fluorescence spectroscopy: tool to monitor tumor physiology in vivo. *J. Biomed. Opt.* **14**, 024010 (2012).

22. Nichols, B. S. Performance of a lookup table-based approach for measuring tissue optical properties with diffuse optical spectroscopy. *J. Biomed. Opt.* **17**, 057001 (2012).

23. Rajaram, N., Nguyen, T. H. & Tunnell, J. W. Lookup table–based inverse model for determining optical properties of turbid media. *J. Biomed. Opt.* **13**, 050501 (2008).

24. Rajaram, N., Gopal, A., Zhang, X. & Tunnell, J. W. Experimental validation of the effects of microvasculature pigment packaging on in vivo diffuse reflectance spectroscopy. *Lasers Surg. Med.* **42**, 680–688 (2010).

25. Arteel, G. E., Thurman, R. G., Yates, J. M. & Raleigh, J. A. Evidence that hypoxia markers detect oxygen gradients in liver: Pimonidazole and retrograde perfusion of rat liver. *Br. J. Cancer* **72**, 889–895 (1995).

26. Otsu, N. A Threshold Selection Method from Gray-Level Histograms. *IEEE Trans. Syst. Man. Cybern.* **9**, 62–66 (1979).

27. Thomlinson, R. H. & Gray, L. H. The histological structure of some human lung cancers and the possible implications for radiotherapy. *Br. J. Cancer* **9**, 539–549 (1955).

28. Drezek, R. *et al.* Light scattering from cervical cells throughout neoplastic progression: influence of nuclear morphology, DNA content, and chromatin texture. *J. Biomed. Opt.* **8**, 7 (2003).

29. Tomaszewski, M. R. *et al.* Oxygen enhanced Optoacoustic Tomography (OE-OT) reveals vascular dynamics in murine models of prostate cancer. *Theranostics* **7**, 2900–2913 (2017).
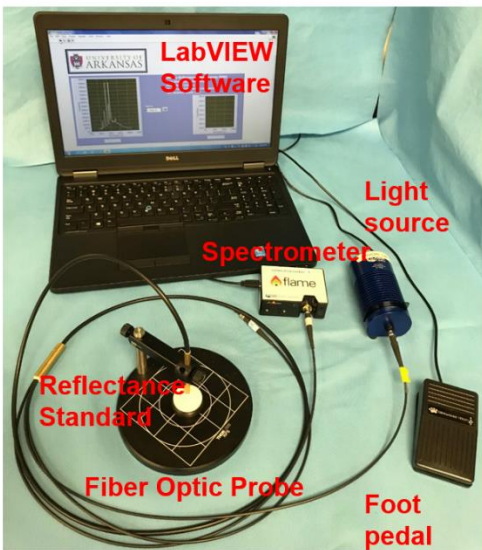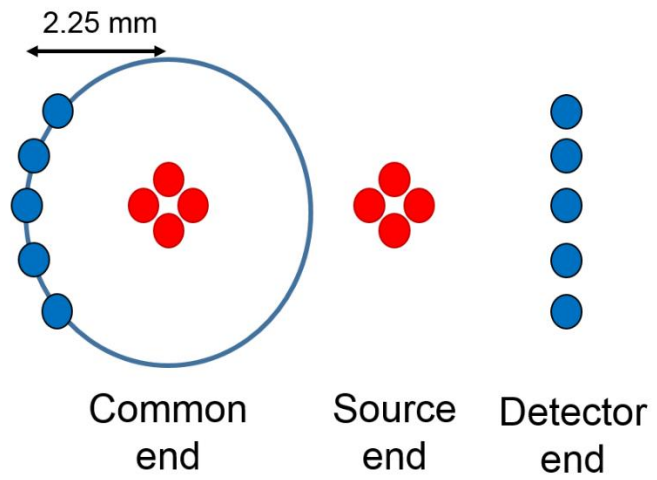
Figure 1. (a) Experimental DRS setup and (b) bifurcated fiber optic probe illustrating the common tissue end, the source end that is connected to the light source, and the detector end that is connected to the USB spectrometer.
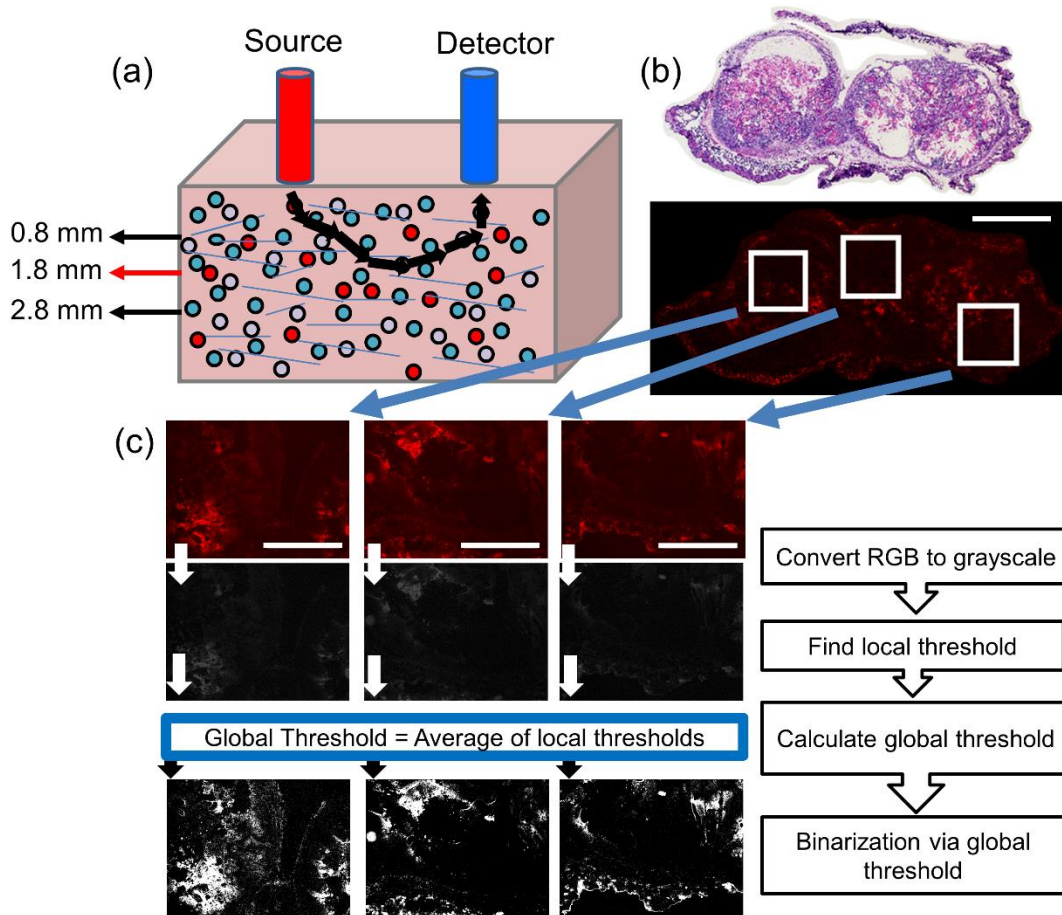
Figure 2. (a) Schematic of optical probe placed on tissue indicating the three depths at which tumor slices were extracted for immunohistochemistry. (b) Stitched H&E and pimonidazole immunofluorescence images of a tumor slice from a depth of 1.8 mm. Scale bar corresponds to 1.8 mm. (c) Flowchart describing the image analysis to calculate HF. Scale bar in these images corresponds to 600 μm.
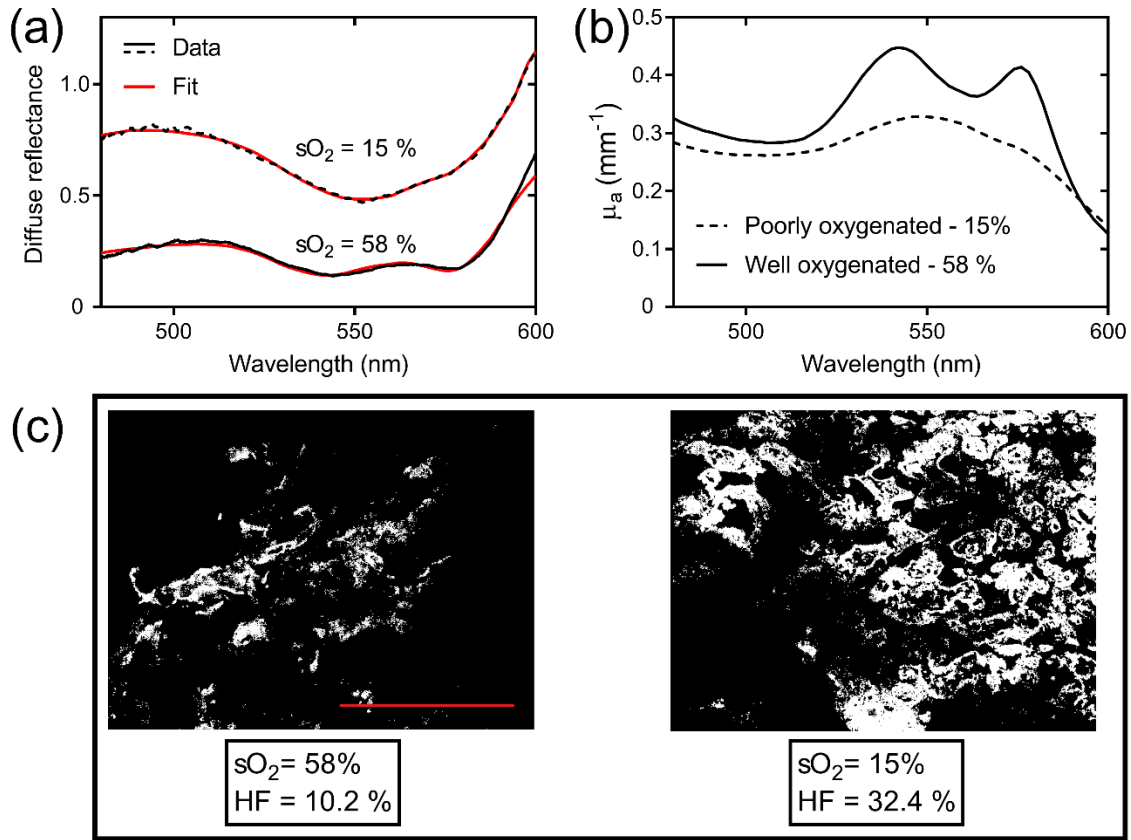
Figure 3. (a) Representative *in vivo* DRS spectra and their LUT fits from UM-SCC-22B tumors with different levels of sO_2. (b) Corresponding wavelength-dependent absorption coefficients determined from LUT fits to the spectra. (c) Processed pimonidazole immunofluorescence images from the same tumors. The calculated HF and vascular oxygenation are shown for each image. Scale bar corresponds to 600 µm.
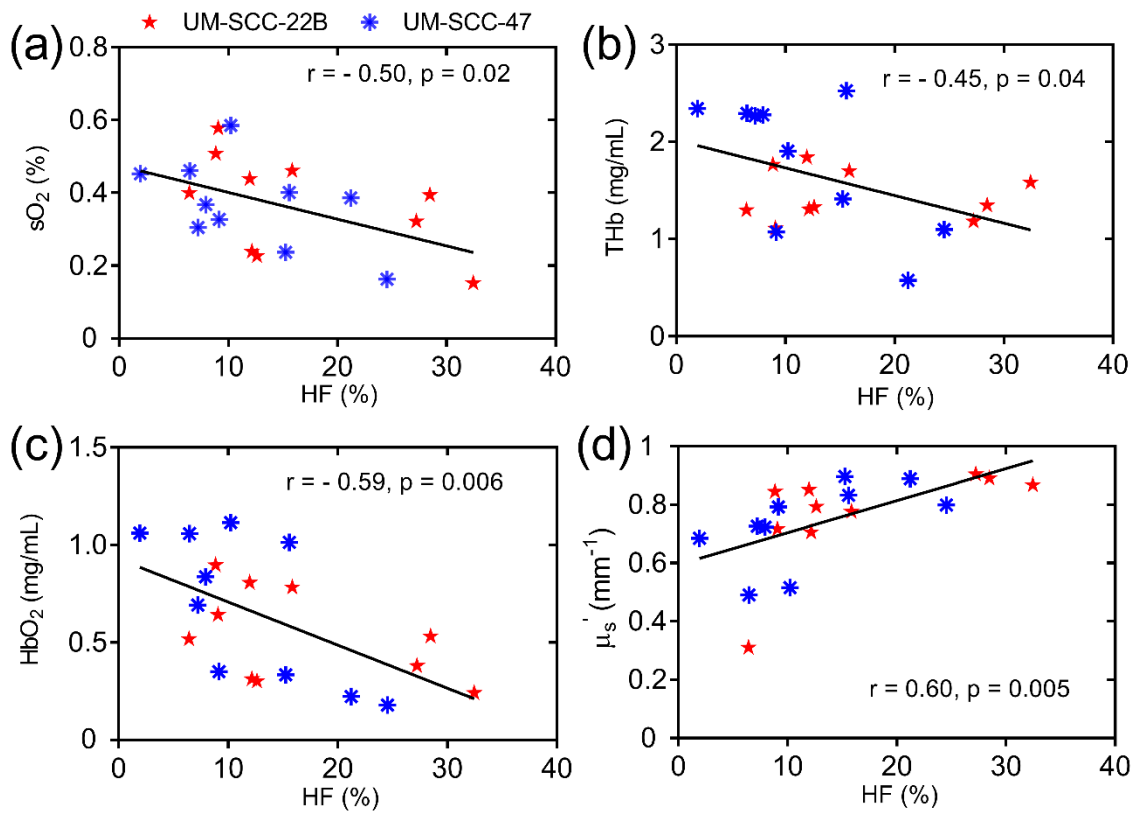
Figure 4. Scatter plots representing the relationship between HF measured at a depth of 1.8 mm and DRS-based measures of (a) sO_2, (b) THb, (c) HbO_2, and (d) mean μ_s' from UM-SCC-22B (red stars) and UM-SCC-47 (blue asterisks). Black solid line indicates the regression line.
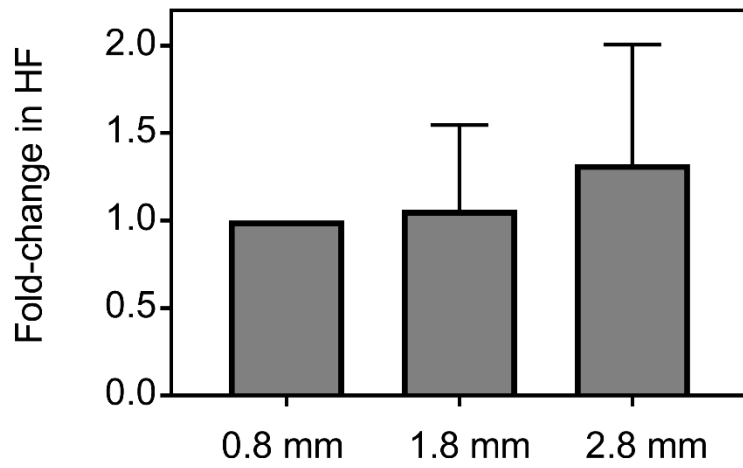
Figure 5. Fold-change in tumor hypoxia levels with depth relative to the HF measured at 0.8 mm. Error bars represent standard deviation of the mean.

Chapter 3: Spectroscopic investigation of radiation-induced reoxygenation in radiation-resistant tumors

<u>Introduction</u>

        The majority of patients diagnosed with head and neck squamous cell carcinoma (HNSCC) present with locally advanced disease (Stage III or IV)[1] and are treated with a combination of surgery, radiation, and chemotherapy[2]. The treatment regimen can last several weeks and typically takes the form of daily radiation therapy - 2 Gy/day; 5 days/week for 7 weeks – and weekly chemotherapy sessions. The delivery of radiation therapy in multiple fractions is hypothesized to cause cell death of oxygenated cells and leads to reoxygenation and radiosensitization of previously hypoxic cells[3–5]. Fractionated radiation therapy is believed to overcome the challenge of hypoxic tumors, which have been shown to be associated with poor long-term outcome[6–9]. Studies in patients and animal models using oxygen-sensing microelectrodes have offered evidence that an increase in tumor oxygenation or reoxygenation between dose fractions is associated with positive treatment response[10,11]. Despite providing absolute measures of oxygenation in tissue, these microelectrodes could disrupt the microenvironment when inserted into the tumor and are therefore not amenable to repeated measurements.

        In contrast to microelectrodes, diffuse reflectance spectroscopy is an optical fiber-based technique that can non-invasively quantify hemoglobin oxygen saturation within a sampled tissue volume. DRS is sensitive to light absorption by hemoglobin, the primary oxygen carrier in blood, and can determine the concentrations of oxygenated and deoxygenated hemoglobin present and hence allow calculation of hemoglobin oxygen saturation[12,13]. Measurements of hemoglobin oxygen saturation from tumors with DRS have been shown to be concordant with simultaneous pO_2 measurements using oxygen-sensing microelectrodes[14,15]. In addition, we have found a significant negative correlation between vascular oxygenation and immunohistochemical assessment of tumor hypoxic fraction[16]. Leveraging the noninvasive capabilities of DRS and its

sensitivity to tumor hemoglobin oxygen saturation, Hu *et al* found that early reoxygenation during the treatment regimen was associated with treatment failure whereas late reoxygenation about 10 days after treatment was associated with local control in head and neck tumor xenografts[17]. These studies utilized a hypofractionated dosing schedule of 7.5-13.5 Gy/day for 5 consecutive days. Interestingly, previous work from our lab has also uncovered radiation-induced reoxygenation in radiation-resistant lung tumor xenografts in the first 24-48 hours after radiation. These studies were conducted in a matched model of radiation resistance treated with conventional fractionation of four 2 Gy doses over two consecutive weeks[18]. However, this work did not explore the mechanism of reoxygenation in the treatment-resistant tumors or relate reoxygenation to treatment outcome.

The primary goal of the current study was to determine radiation-induced changes in tumor oxygenation in head and neck tumor xenografts and investigate the association of this reoxygenation with tumor local control or recurrence. We used two previously characterized patient-derived HNSCC cell lines - UM-SCC-22B and UM-SCC-47 – to represent radiation sensitivity and resistance, respectively[19,20], and treated tumor xenografts with four 2 Gy fractions over 2 consecutive weeks (total dose of 8 Gy). We acquired optical spectra and quantified tumor oxygenation every day for 14 days, including immediately before and an hour after radiation on treatment days. Our results suggest that while reoxygenation patterns can be observed in both radiation-resistant and -sensitive tumors, the kinetics and source of this reoxygenation can be very different, depending on the radiation sensitivity. Given the importance of oxygen supply and consumption within a tumor and their roles in modulating response to radiation, these results shed light on the importance of longitudinal, real-time measurements of tumor oxygenation during radiation therapy to differentiate radiation responders from non-responders and hence improve response rates.

Materials and Methods

Cell culture

      Cell culture conditions have been reported in detail in chapter 2. Oxygen consumption rate (OCR) of UM-SCC-22B and UM-SCC-47 cells were determined using a Seahorse metabolic flux assay as described previously[21]. Head and neck tumor xenografts were formed by injecting 1.5 million cells suspended in 1:1 mixture of Matrigel (Corning, New York) and saline into the right (treated group) or both (control group) flanks of nude mice (see tumor distribution in Table 1).

Tumor xenografts and fractionated radiation treatment

      Animals in the treated (XT) groups underwent radiation treatment with four doses of 2 Gy over two consecutive weeks (8 Gy in total)[20] using an X-rad 320 biological cabinet (Precision X-Ray, North Branford, CT) (see treatment schedule in Figure 1A), while animals in the NT groups served as controls. Animals were placed in the center of a 20 x 20 cm X-ray radiation field. During radiation treatment, mice were kept under anesthesia using a mixture of isoflurane (1.5% v/v) and oxygen while the entire animal body was covered under lead blocks except the tumor. Greening *et al* have shown this combination and dose to closely mimic no anesthesia conditions[22]. Mice were monitored daily, and tumors were excised if: 1) tumor volume reached 1500 mm^3 2) tumor necrosis was observed 3) other health related issues occurred. A subset of mice from each of the 4 groups were euthanized and tumors were excised at baseline, 24, and 48 hours after a single 2 Gy dose of radiation (see Table 2).

Diffuse reflectance spectroscopy

      Our portable spectroscopic system consists of a tungsten halogen lamp (HL-2000, Ocean Optics, Dunedin, Florida) as light source, a USB fiber optic spectrometer (Flame, Ocean Optics) for spectral light acquisition, and a bifurcated optical probe (dia.= 200 µm, NA=0.22; FiberTech Optica, Kitchener, ON, Canada) for light delivery and collection. The probe tip was used for light delivery and collection and is equipped with four illumination and five detector fibers located at a

source-detector separation distance (SDSD) of 2.25 mm with a sampling depth of approximately 1.8 mm[13]. We used a foot pedal controlled with custom LabVIEW software (National Instruments, Austin, Texas) for data acquisition. About 2-5 spectra in the wavelength range of 475 to 600 nm were collected and averaged optical properties were used to represent that tumor in temporal analysis. Because the surface area of our probe (32 mm^2) is always smaller than the surface area of typical tumor under investigation (average ~ 200 mm^2), we were able to collect multiple spectra from various parts of the tumor. Prior to any optical measurement from animals, reflected light intensity from an 80% reflectance standard (SRS-80-010; Labsphere, North Sutton, New Hampshire) was acquired to calibrate for daily variations in light throughput. Optical spectra from each tumor were recorded daily for a period of 14 days (see optical measurements schedule in Figure 1A) while animals were under anesthesia (1.5% v/v isoflurane mixed with 100% oxygen). Analysis of acquired optical spectra was performed using an experimental model. See chapter 2 for details.

Logistic regression and leave-one-out cross-validation

To construct an artificial intelligence-based classification algorithm, we employed a logistic regression (LR) model because of its simplicity. Five extracted optical properties from each tumor normalized to its pre-treatment value were used as input parameters while the model output discriminates two classes (local-control: 0, treatment-failure: 1). In order to train our LR model, we used the spectra from 27 treatment-failure and 16 local-control tumors. We labeled our tumors to be treatment-failure if two weeks after initiation of therapy, the volume had increased ≥ 25% of the initial volume of 200 mm^3. Weights of the LR model were fine-tuned using gradient decent optimization algorithm with a learning rate of 0.0001. The training weights were iteratively adjusted for 50 epochs. Model accuracy was assessed using a leave-one-out cross-validation algorithm. All optical properties of individual tumors and their corresponding binary label were sequentially excluded, and the remaining data set were used to train the model and the accuracy of the model

was evaluated on the left-out tumor. Logistic regression analysis was conducted by scripts written in MATLAB (Mathworks, Natick, Massachusetts).

Immunohistochemistry

An hour prior to euthanasia, mice were injected (i.p.) with Pimonidazole (60 mg/kg – Hypoxyprobe, Burlington, MA). After tumor resection and euthanasia, the flash-frozen tumors were sliced into sections of 10 μm using a cryostat (CM 1860; Lecia, Inc., Nussloch, Germany). We followed a direct labeling protocol in immunostaining of harvested samples[23]: After acclimatization to room temperature, slides were hydrated in PBS and a hydrophobic barrier was formed around each tissue section using a pap pen (Vector Laboratories, Burlingame, CA). Slides were fixed with 4% PFA, permeabilized using 0.5% Triton-X 100, and non-specific binding was blocked at room temperature using an in-house blocking solution (95% PBS + 4% goat serum + 1% sodium azide) for an hour. Slides were then stained with mouse monoclonal antibody conjugated to DylightTM 549 fluorophore (Hypoxyprobe Red 549 kit; HPI, Inc, Burlington, MA). Serial slides were also incubated with primary HIF-1α rabbit (NB100449 – NOVUS Biologicals, Littleton, CO) and VEGF-R2 rabbit (9698S – Cell Signaling Dancers, MA) antibodies for 3 hours at room temperature. The slides were next tagged with Alexa Fluor 488 goat anti-Rabbit (A-11008, Thermo Fisher Scientific, Waltham, MA; for HIF-1α) and (4412S-Cell Signaling; for VEGF-R2). The entire tumor section on each slide was imaged using a confocal microscope (Fluoview FV10i, Olympus) using a 10X objective (UPLSAPO10X, NA = 0.4, Olympus). Images acquired from individual regions of interest (ROI) were stitched using the microscope software. Stitched images were binarized using a fixed threshold to separate pixels containing true signal from the background. This fixed threshold was identified from representative histograms where the signal of non-specific background differed from the true signal. Four tumor sections were treated without Pimonidazole-specific, HIF-1α-specific, and VEGF-R2-specific antibodies to determine endogenous tissue autofluorescence, which was found to be negligible. Two tumor tissue sections

were also incubated with secondary AF488 antibody without HIF-1α and VEGF-R2 specific antibodies to determine the presence of any non-specific binding tissue section, which was found to be absent. Finally, percentage of Pimonidazole positive, HIF-1α positive, and VEGF-R2 positive pixels within each tissue section was calculated by dividing segmented pixels by the total number of tumor tissue pixels.

It is worth mentioning that HIF-1α from Santa Cruz biotechnology (13515) had strong non-specific binding and did NOT provide reliable results. This was determined by treating 3 specimens on the same slide with primary and secondary, secondary alone, and no antibodies which helped us in determining the presence non-specific binding and tissue autofluorescence.

Statistical analysis

Overall survival in each mouse was measured as the length of time in days from when the mouse's tumor reached 200 mm^3 to when the mouse was euthanized for excessive tumor size (defined as a tumor volume of ≥1500 mm^3). Since the animals from control groups were inoculated with tumors on both flanks, overall survival in a control-group mouse was marked as starting on the day when its first tumor reached the volume of 200 mm^3. Any animal that died for a reason other than excessive tumor size had its overall survival right-censored on the day of its death. The differences in overall survival between groups were compared statistically using the 2-sided log-rank test with $p < 0.05$ significance level, while the survival benefit with radiation therapy was quantified as the inverse of the Cox-regression hazard ratio comparing treated to control animals.

Prior to statistical analysis, the raw volume data were logarithmically transformed with the aim of minimizing the correlation of group means with group standard errors. The transformed data then were analyzed using repeated-measures analysis of variance (ANOVA) using the MIXED procedure in SAS v9.4 (The SAS Institute, Cary, NC, USA). The analysis model for log-volumes employed an ante-dependence structure to model the covariance over time among the longitudinally collected data and utilized the Kenward-Roger method to determine test-statistic

degrees of freedom. Within each cell line, the right flanks from control-group mice were compared to the right flanks from XT-group mice. Within each combination of cell line and treatment, mean log-volumes on subsequent days of growth were compared to their Day 1 value. All comparisons employed an unadjusted $p<0.05$ significance level (2-sided) despite the multiple comparisons, in order not to inflate Type II (false-negative) error.

Raw optical properties from day 1 through 14 from right flanks were normalized by treatment group to the group mean of the value it had on day 1. This way, values on day 1 have mean of 1 but individual values different from 1 (i.e. they show variability), and thus can be included in the analysis. The normalized data were then subjected as before to repeated-measures ANOVA using the MIXED procedure in SAS v9.4 software. For each normalized optical property, the analysis model employed an unstructured autocovariance matrix to model the covariance between different measurements performed on the same tumor over time and utilized the Kenward-Roger method to determine test-statistic degrees of freedom. All comparisons between treatment groups or time points were conducted as previously described and employed an unadjusted $p<0.05$ significance level (2-sided) despite the multiple comparisons, in order not to inflate Type II error.

We used the Wilcoxon rank sum test for statistical analysis of immunohistochemical data. All tests employed a 2-sided $p<0.05$ significance level.

Results

Figures 1B-C present the Kaplan-Meier curves for the UM-SCC-22B and UM-SCC-47 tumors, respectively. Animals growing UM-SCC-22B tumors that were irradiated (XT) survived significantly longer compared with non-irradiated controls (NT), with a mean survival of 56.4 vs. 21.9 days (log-rank $p<0.0001$); the associated survival benefit with radiation treatment was 44.7 (indicating 44.7-fold higher survival for irradiated tumors) with a 95% confidence interval [CI] of 9.34–214. Although the heavy censoring in irradiated UM-SCC-47 tumors (Figure 1C) prevented

us from seeing appreciable delay in mean survival compared with non-irradiated controls (mean survivals of 28.5 vs. 25.5 days), we still observed a significant difference in survival of the NT and XT groups (log-rank p=0.0052) with an associated survival benefit of 5.51 (95% CI: 1.48-20.5) for XT groups. Figure 1D-E presents measurements of tumor volume during and after radiation therapy of the UM-SCC-22B and UM-SCC-47 tumors. As early as day 2, fractionated radiation therapy resulted in significant differences between the volume of NT and XT groups of UM-SCC-22B tumors ($p < 0.0001$; illustrated in Figure 1D by black asterisk for day 2 and black forward arrow for following days). In contrast, there were no significant differences between the UM-SCC-47-NT and -XT groups, and mean tumor volumes in both groups were nearly identical for the first 7 days (Figure 1E). Importantly, tumor volumes in the UM-SCC-22B-XT group were significantly higher than baseline only after Day 21 ($p = 0.001$); for all other groups, the increase in tumor volume was significant beginning Day 2.

To determine radiation-induced changes in tumor oxygenation, we quantified the optical properties from the measured DRS spectra (Figure 2) and computed the fold-change in the measured parameters over time with respect to their pre-radiation baseline measures. Figure 3A-D illustrates the fold-change in hemoglobin oxygen saturation (sO_2) and total hemoglobin concentration (cHb). Radiation therapy did not cause significant changes in sO_2 or cHb in the UM-SCC-22B tumors (Figure 3A&C). There was a significant increase in sO_2 in the irradiated UM-SCC-47 tumors compared with pre-radiation baseline sO_2 ($p < 0.05$) and this significant reoxygenation trend was evident on several days over the 14-day period when these tumors were monitored (Figure 3B). The irradiated UM-SCC-47 tumors also showed a significant decrease in cHb compared with pre-radiation baseline (Days 6, 7, 10, 13 and 14) and the non-irradiated group (Days 6, 8, and 14) ($p < 0.05$; Figure 3D). Analysis of oxygenated (HbO_2) and deoxygenated hemoglobin (dHb) concentrations showed that the temporal decay in cHb and the increase in sO_2 in the UM-SCC-47 tumors could be attributed almost entirely to a decrease in dHb while there was no significant change in HbO_2 (Figure 3E-H). Finally, we also extracted the mean reduced

scattering coefficient (μ_s') of our tumors in all groups. We observed temporally significant increase in μ_s' among both NT and XT groups of UM-SCC-22B tumors after second dose of radiation (red & blue pounds – Figure 3I) while no significant changes were reported for UM-SCC-47 tumors (Figure 3J).

While there was an overall increase in tumor oxygenation in the UM-SCC-47 tumors over the 14-day period, we found that reoxygenation trend was cyclical, consisting of several rapid increases followed by decreases in tumor oxygenation. To investigate this cyclical nature of reoxygenation, we studied the short-term effects of radiation therapy on tumor sO_2 over the 48 hours following each dose of radiation. Figure 4 presents data from 1, 24, and 48 hours post-therapy for each of the 4 doses. In response to each dose of radiation, there was an increase in sO_2 in the UM-SCC-22B and UM-SCC-47 tumors 1 hour after radiation; this reoxygenation was statistically significant after the first, third, and fourth doses in the UM-SCC-22B ($p<0.01$). After each dose, this increase in sO_2 was followed by a decrease to baseline levels over the next 48 hours. Similarly, UM-SCC-47 tumors displayed an increase in mean sO_2 immediately after radiation that was followed by a large decrease at the 24-hour time point. However, at the 48-hour time point, the mean sO_2 was greater than the pre-radiation baseline for that dose (Figure 4B). Within these cell lines, the radiation-induced changes in sO_2 appear to be driven by different factors in the UM-SCC-22B and the UM-SCC-47 tumors. The large increase in sO_2 in the UM-SCC-22B tumors immediately after radiation is due to a statistically significant increase in HbO_2. On the other hand, the increase in sO_2 in the UM-SCC-47 tumors is due to a decrease in dHb over time (Figure 4C-F).

Reoxygenation following radiation has been shown to upregulate HIF-1α in tumors[24]. Therefore, we examined the extent of tumor hypoxia and HIF-1α expression in the UM-SCC-22B and UM-SCC-47 tumors over the first 48 hours following radiation therapy (Table 2, Figure 5, Figure 6A). Figure 6B-D presents the results of immunohistochemical assessment from tumor sections collected at baseline, 24h, and 48h after a single 2 Gy dose of radiation in the NT and

XT groups. Our results indicate that in comparison to UM-SCC-22B tumors, UM-SCC-47 tumors have slightly higher hypoxic fraction and a significantly higher HIF-1α expression at baseline (p= 0.02). Radiation therapy had different effects on the hypoxic fraction and HIF-1 expression in the two tumor groups. We observed an increase in hypoxic fraction in the UM-SCC-22B tumors 24- and 48-hours (p=0.03) following radiation therapy and a trend towards decreasing hypoxic fraction in the UM-SCC-47 tumors. While we found no changes in HIF-1α expression in the UM-SCC-22B tumors following radiation, there was a trend towards a decrease in HIF-1α expression in the UM-SCC-47 tumors at the 48-hour time point.

Tumor hypoxia and increased HIF-1 expression has been known to promote angiogenesis via increased expression of vascular endothelial growth factor (VEGF)[25,26]. Thus, we investigated the presence and extend of VEGF-R2 in our tumor sections. Figure 8A presents representative images of immunostaining of VEGF-R2 at baseline and 1 hour after radiation in radiation-sensitive and -resistant tumors. Quantitative assessment of histological slides identified significant increase in expression of VEGF-R2 1 hour after radiation in UM-SCC-22B radiation-sensitive tumors. However, UM-SCC-22B responsive tumors had relatively lower levels of VEGF-R2 both at baseline and in 1, 24, and 48 hours after radiation.

In addition to using optical spectroscopy in understanding differential reoxygenation patterns among radiation-resistant and -sensitive tumors, we also sought to investigate whether these measurements can provide a diagnostic scheme in classifying local-control and treatment failure tumors. Although UM-SCC-22B tumors are sensitive to radiation as demonstrated by this study and others[20], 8 out of 24 UM-SCC-22B tumor bearing animals were treatment-failures. Using logistic regression algorithm, we conducted leave-one-out cross-validation based on the changes in optical properties of days 2 through 14 with respect to day 1. The leave-one-out cross-validated area under the curve (AUC) computed from a logistic regression model based on changes in optical properties in 4 representative days are 0.62 (day 2), 0.58 (day 5), 0.59 (day 9), and 0.59 (day 11). The corresponding daily receiver operating characteristic (ROC) curves are

shown in Figure 9 A-D. We finally confirmed the robustness of our LR analysis by randomly assigning class labels to same dataset and observed that the overall accuracy of the model decreased to the accuracy of random classifier (0.49, 0.44, 0.47, and 0.49 in days 2, 5, 9, and 11, respectively). Taken together, the results of the LR and leave-one-out classifier model demonstrate the capability of changes in optical properties in determining radiation response.

Discussion

Reoxygenation following radiation therapy has long been postulated to be an important mechanism in the radiosensitization of previously hypoxic cells within a tumor and has been shown to be an indicator of tumor response to radiotherapy. However, there is also evidence that reoxygenation following radiation is a double-edged sword because it can lead to radiation resistance. Temporal investigations of tumor reoxygenation are challenging because the technologies utilized are either invasive (oxygen-sensing microelectrodes or tissue removal) or expensive (magnetic resonance imaging, positron emission tomography), and are not amenable to repeated measurements. Diffuse reflectance spectroscopy (DRS) has been used in animal studies to identify differences between partial and complete responders based on differences in sO_2 in response to high doses of radiation/fraction (7-39 Gy)[17,27]. Our long-term clinical goal is to investigate whether using DRS to measure tumor functional changes in HNSCC patients, who are typically treated with dose fractions of 2 Gy, can be validated as a predictor of treatment response. Here, we used DRS to monitor the reoxygenation kinetics of HNSCC tumors with known radiation sensitivity.

Previous work has shown that the UM-SCC-22B tumors are sensitive to radiation therapy while the UM-SCC-47 tumors do not respond to therapy when treated with four doses of 2 Gy over two consecutive weeks[20]. While the outcomes for both cell lines in our study were largely consistent with this report, there was a significant difference in tumor growth delay in the UM-SCC-22B beginning the day after treatment, while the report by Stein *et al* found significant

differences only beginning Day 15. In fact, the mean tumor volume in the irradiated tumors remained unchanged during and up to 1 week after four 2 Gy fractions were administered over 2 weeks. This corresponded to no significant change in tumor hemoglobin oxygen saturation over the 14 days of treatment monitoring, indicating that therapy had likely arrested cell proliferation within these tumors. It is important to note that while there were no long-term changes in sO_2 or cHb in the UM-SCC-22B tumors, there were immediate radiation-induced increases in oxygenation 1-hour post-treatment (Fig. 3) that are largely consistent with previous studies that utilize DRS to monitor radiation response[18,27]. Moreover, the control UM-SCC-22B and UM-SCC-47 tumor that grow at the same rate as the irradiated UM-SCC-47 tumors also show nearly no change in oxygenation with respect to baseline. A lack of reoxygenation has been observed in head and neck cancer patients about two weeks into daily treatment with fractionated radiation therapy (2 Gy/day)[8]. Stadler *et al* reported a statistically significant reduction in pO_2 and increase in hypoxic fraction in locally advanced HNSCC patients who were evaluated 3 weeks after commencing fractionated therapy at 2Gy/day. This decrease in pO_2 was observed in both complete and partial responders[28]. They attributed the observed reduction in pO_2 to reduction of blood flow in response to radiation. Conversely, increases in tumor oxygenation have also been reported in response to 5 doses of 2 Gy in head and neck tumor xenografts although the observed changes did not correlate with response/failure[11].

In contrast to the UM-SCC-22B tumors, we noted a significant increase in sO_2 in the UM-SCC-47 tumors which are relatively non-responsive to radiation. Other studies using DRS to investigate radiation-induced increase in oxygenation have attributed these changes to increased perfusion[17,27], which typically manifests as an increase in oxygenated hemoglobin (HbO_2). When we investigated the changes in hemoglobin concentration, we found that the increased sO_2 was not due to increased HbO_2 but rather due to a decrease in deoxygenated hemoglobin concentration (dHb). By Day 14, the dHb concentration in the UM-SCC-47 tumors had declined to about 79% of its baseline value while HbO_2 remained unchanged compared with pre-radiation

44

baseline. A reduction in deoxygenated hemoglobin concentration in the vasculature points to a decrease in oxygen consumption in the surrounding tumor tissue. This would be congruent with a number of studies in the literature, such as one where SCCVII murine tumors treated with 10 Gy of radiation exhibited a reduction in hypoxia found to be caused by a combination of decreased oxygen consumption and increased perfusion[29]. In HNSCC patients treated with daily fractions of 2 Gy (total of 70 Gy), Lyng and colleagues have shown changes in oxygenation, determined by polarographic needles, to coincide with changes in biopsy-determined cell density[30]. Lack of simultaneous changes in vascular density led them to conclude that the observed changes in hypoxia were caused by changes in OCR rather than changes in delivery. Notably, in patients with advanced HNSCC treated with hyper-fractionated radiation therapy, Dietz *et al* found that complete or partial responders show minimal change in reoxygenation in comparison to a strong reoxygenation among non-responding patients[31].

Although reoxygenation has been considered to lead to cell kill, reoxygenation following radiation can also lead to the generation of reactive oxygen species (ROS) following hypoxia-reoxygenation injury and hence, the stabilization of HIF-1[32]. This is supported by an elegant study by Moeller *et al* where mice with 4T1 mammary adenocarcinoma tumors showed HIF-1 activation following radiation that coincided with reoxygenation[24]. We have previously shown that radiation-resistant human lung cancer cells have lower oxygen-consumption rate (OCR) and higher HIF-1 content both at baseline and 24 hours after a single dose of 2 Gy compared with their radiation-sensitive counterparts[21]. In addition, we have also shown that increased HIF-1 content leads to increased glucose uptake and hence an increased in reduced glutathione which led to a reduction in mitochondrial ROS production. Treatment with a HIF-1 inhibitor led to a decrease in HIF-1, glucose uptake and reduced glutathione and led to increased cell death in the radiation-resistant cells in comparison with the radiation-sensitive cells[33]. Our observation of a decrease in dHb, a corresponding increase in sO_2, coupled with greater HIF-1α expression both prior to and after radiation therapy in the UM-SCC-47 tumors compared with the UM-SCC-22B tumors strongly

suggests that these changes are due to a decrease in oxygen consumption rate and that the reduction in OCR plays a role in radiation resistance. In fact, *in vitro* measurements of oxygen consumption rate revealed lower OCR in UM-SCC-47 cells in comparison to UM-SCC-22B cells (see figure 7).

However, significant research has demonstrated the clinical value of reducing OCR to improve treatment response by increasing the available oxygen for radiosensitization. Secomb and colleagues showed, using theoretical simulations that utilized experimental observations, that a reduction in oxygen consumption by only 30% was sufficient to completely abolish hypoxia whereas a 4-fold increase in flow rate or a 11-fold increase in arterial pO_2 was required to achieve the same effect[34]. A comprehensive study that measured radiation-induced changes in the tumor microenvironment in the first 24 hours proposed that early reoxygenation within tumors was likely due to a combination of increased oxygen supply and a decrease in oxygen consumption[35]. The same group showed that inhibiting mitochondrial respiration using glucocorticoids leads to a reduction in OCR and delayed tumor growth[36]. A more recent study has shown that Arsenic trioxide (As_2O_3) treatment leads to enhanced oxygenation through reduced oxygen consumption in mouse transplantable liver tumors, and its combination with 10 Gy leads to significant delay in tumor growth and extended survival[37]. In addition, Benej *et al* determined that reducing OCR using Papaverine, a muscle relaxant and mitochondrial complex I inhibitor, significantly decreases hypoxia, improves tumor pO_2, and delays radiation-induced tumor growth[38]. These studies present an interesting juxtaposition – while a reduction in oxygen consumption is clearly beneficial in decreasing hypoxia and hence improving response rates, our work demonstrates that the growing, relatively non-responsive UM-SCC-47 tumors are likely developing a reduced oxygen consumption rate which is being manifested as a decrease in deoxygenated hemoglobin and hence increased oxygenation. As discussed earlier, our previous work in a matched model of radiation resistance showed that inhibition of HIF-1α led to a reduction in pyruvate dehydrogenase kinase (PDK-1) content[33]. PDK-1 is a negative regulator of pyruvate entry into the mitochondria.

Thus, inhibiting PDK-1 increased mitochondrial oxygen consumption and hence cell death in radiation-resistant cells. It will be important to investigate the effects of HIF-1 inhibition *in vivo* to determine if the same phenomenon can be recapitulated in tumors.

HIF-1 also plays an important role in regulating vascular radiosensitivity. Gorski *et al* showed that radiation caused a large cell line-dependent increase in vascular endothelial growth factor (VEGF) over the first 72 hours following treatment and that increased VEGF expression promoted endothelial cell radioresistance[39,40]. Treatment of mice with anti-VEGF prior to radiation therapy led to a significant reduction in tumor growth that was greater than the expected additive effect of the two treatments. Moeller *et al* found that VEGF expression overlapped completely with HIF-1 in irradiated tumors, strongly implicating HIF-1 as a major regulator of endothelial cell radiation resistance due its regulation of VEGF[24]. However, our observation of increased VEGF-R2 in UM-SCC-22B tumors which expressed lower levels of HIF-1α may indicate that VEGF could have different upstream sources independent from HIF-1.

Although we did not observe any statistically significant differences in tissue scattering between the NT and XT groups of either cell line, we did observed a significant temporal increase in UM-SCC-22B tumors (both NT and XT) over the 14-day period. The increased scattering in the NT group could be attributed to either increased tumor volume, which would increase cell density and hence light scattering from cells, or an increase in tumor hypoxia. We have previously demonstrated a strong association between tumor hypoxic fraction and tissue scattering[16]. However, the temporal changes in scattering in the XT group are intriguing given the lack of change in tumor volume or tumor oxygenation over the 14-day period and seem worthy of further investigation.

Although diffuse reflectance spectroscopic measurements present a promising avenue for studying radiation response in superficial tumors of skin, cervix, and oral cavity, it has limited penetration depth and is not ideal for deep-seated tumors. Sampling depth can be improved by using larger separations between source and detector fibers as well as by extending spectral

boundaries to near-infrared (NIR). For example, Sunar *et al* have demonstrated the utility of NIRS in monitoring chemo-radiation induced physiological changes in patients of head and neck cancer[41]. In addition to greater penetration depth, NIR spectroscopy provides more quantitative parameters because of the light absorption by lipid and water at higher wavelengths. A study by Ohmae *et al* in breast cancer patients, has shown such optical measurements of lipids and water to be highly concordant with computed tomographic measurements[42]. Tromberg *et al* have used a combination of hemoglobin and lipid absorption as well as scattering to determine a 'Tissue optical index' for predicting treatment response in breast cancer patients undergoing neoadjuvant chemotherapy[43]. Multispectral optoacoustic tomography (MSOT)[44–46] and photoacoustic imaging[47,48] is another technique that can provide information about hemoglobin concentration and saturation at depths of up to 7 cm. However, despite its repeated and non-invasive measurements of tissue physiology, MSOT-based systems are currently more expensive than diffuse optical systems.

We also used radiation induced changes in optical properties (sO_2, HbO_2, dHb, cHb, μ_s') for constructing our logistic regression and leave-one-out based classifier and we are able to differentiate local-control and treatment-failure tumors with AUC value of 0.6. Although we show acceptable results, our accuracy in classification of responding and non-responding tumors is far from ideal. It should be noted that similar accuracy for identification of radiation-response using only changes in sO_2 has been reported[17]. However, that study have used the changes in oxygen saturation in response to larger doses of radiation in constructing their logistic regression model. Since larger doses of radiation can cause greater reoxygenation in tumors[17], changes in oxygenation alone in their model had a similar performance to ours. Since the goal of this study is to investigate whether optical spectroscopy combined with LR can identify tumor response while treated with lower doses of radiation, increasing sample size in training the LR model may increase the overall accuracy in classification of local-control and treatment-failure tumors. In addition, we have used only hemoglobin-related parameters and scattering in training our LR

model. However, oxygenation and structural changes may not provide a fully holistic representation of functional differences among radio-resistant and radio-responsive tumors and adding other biomarkers could enhance the performance of LR in classification of radio-responsive and radio-resistant tumors. While our work here and elsewhere has explored the important role for HIF-1 in the context of oxygen consumption and metabolism in radiation resistance, HIF-1 also affects other aspects of the tumor microenvironment, such as extracellular matrix remodeling. We have previously used Raman spectroscopy on excised tumor xenografts to demonstrate differences in biomolecular composition, specifically lipids and collagen, in irradiated and non-irradiated UM-SCC-22B and UM-SCC-47 tumors[49]. Based on these differences, we were able to accurately distinguish radiation-sensitive from responsive tumors. Thus, combining diffuse reflectance and Raman spectroscopy for simultaneous monitoring of radiation-induced functional and biomolecular changes within the tumor could improve our understanding of microenvironmental changes related to treatment resistance. This combination can also improve the overall accuracy in classification of radiation-resistant and -sensitive tumors. Other studies have also shown that compared to a single optical modality, combination of optical modalities is more accurate in discriminating healthy and diseased lesions in neoplasms of breast[50] and cervix[51,52].

In summary, we have used diffuse reflectance spectroscopy to monitor tumor hemoglobin oxygen saturation during the course of radiation therapy and found that radiation-resistant tumor xenografts show an increase in tumor vascular oxygenation following radiation therapy, a phenomenon not observed in radiation-sensitive HNSCC tumor xenografts. Our analysis of oxygenated and deoxygenated hemoglobin concentrations following radiation therapy point to decreased oxygen consumption as a likely factor in the increased reoxygenation observed in the UM-SCC-47 tumors. In addition to providing valuable information about functional changes within the tumor at early time points, our study also illustrates that optically determined reoxygenation

can be translated into clinical setting and used as a biomarker for distinguishing radio-responsive

and non-responsive head and neck cancer patients.

References

1.	Worsham, M. J. Identifying the risk factors for late-stage head and neck cancer. *Expert Review of Anticancer Therapy* (2011) doi:10.1586/era.11.135.

2.	Marur, S. & Forastiere, A. A. Head and Neck Squamous Cell Carcinoma: Update on Epidemiology, Diagnosis, and Treatment. *Mayo Clinic Proceedings* (2016) doi:10.1016/j.mayocp.2015.12.017.

3.	Fowler, J. The rational of dose fractionation. The Relationship of Time and Dose in the Radiation Therapy of Cancer. in 6–23 (Karger Publishers, 1969).

4.	Kallman, R. F. The Phenomenon of Reoxygenation and Its Implications for Fractionated Radiotherapy. *Radiology* **105**, 135–42 (1972).

5.	Withers, H. R. The 4 Rs of radiotherapy. *Adv. Radiat. Biol.* **5**, 241–271 (1975).

6.	Brizel, D. M., Sibley, G. S., Prosnitz, L. R., Scher, R. L. & Dewhirst, M. W. Tumor hypoxia adversely affects the prognosis of carcinoma of the head and neck. *Int. J. Radiat. Oncol. Biol. Phys.* (1997) doi:10.1016/S0360-3016(97)00101-6.

7.	Nordsmark, M. *et al.* Prognostic value of tumor oxygenation in 397 head and neck tumors after primary radiation therapy. An international multi-center study. *Radiother. Oncol.* (2005) doi:10.1016/j.radonc.2005.06.038.

8.	Brizel, D. M., Dodge, R. K., Clough, R. W. & Dewhirst, M. W. Oxygenation of head and neck cancer: Changes during radiotherapy and impact on treatment outcome. *Radiother. Oncol.* **53**, 113–117 (1999).

9.	Rudat, V. *et al.* Predictive value of the tumor oxygenation by means of pO2histography in patients with advanced head and neck cancer. *Strahlentherapie und Onkol.* (2001) doi:10.1007/PL00002427.

10.	Milas, L. *et al.* Role of Reoxygenation in Induction of Enhancement of Tumor Radioresponse by Paclitaxel. *Cancer Res.* (1995).

11.	Ressel, A., Weiss, C. & Feyerabend, T. Tumor oxygenation after radiotherapy, chemotherapy, and/or hyperthermia predicts tumor free survival. *Int. J. Radiat. Oncol. Biol. Phys.* **49**, 1119–1125 (2001).

12.	Rajaram, N., Nguyen, T. H. & Tunnell, J. W. Lookup table–based inverse model for determining optical properties of turbid media. *J. Biomed. Opt.* **13**, 050501 (2008).

13.	Nichols, B. S. Performance of a lookup table-based approach for measuring tissue optical properties with diffuse optical spectroscopy. *J. Biomed. Opt.* **17**, 057001 (2012).

14.	Palmer, G. M. *et al.* Quantitative diffuse reflectance and fluorescence spectroscopy: tool to monitor tumor physiology in vivo. *J. Biomed. Opt.* **14**, 024010 (2012).

15.	Wang, H. W. *et al.* Treatment-induced changes in tumor oxygenation predict photodynamic therapy outcome. *Cancer Res.* **64**, 7553–61 (2004).

16. Dadgar, S., Troncoso, J. R. & Rajaram, N. Optical spectroscopic sensing of tumor hypoxia. *J. Biomed. Opt.* **23**, 1–10 (2018).

17. Hu, F. *et al.* Oxygen and Perfusion Kinetics in Response to Fractionated Radiation Therapy in FaDu Head and Neck Cancer Xenografts Are Related to Treatment Outcome. *Int. J. Radiat. Oncol. Biol. Phys.* **96**, 462–9 (2016).

18. Diaz, P. M. *et al.* Quantitative diffuse reflectance spectroscopy of short-term changes in tumor oxygenation after radiation in a matched model of radiation resistance. *Biomed. Opt. Express* **9**, 3794 (2018).

19. Kimple, R. J. *et al.* Enhanced radiation sensitivity in HPV-positive head and neck cancer. *Cancer Res.* (2013) doi:10.1158/0008-5472.CAN-13-0587.

20. Stein, A. P. *et al.* Xenograft assessment of predictive biomarkers for standard head and neck cancer therapies. *Cancer Med.* **4**, 699–712 (2015).

21. Alhallak, K. *et al.* Optical imaging of radiation-induced metabolic changes in radiation-sensitive and resistant cancer cells. *J. Biomed. Opt.* **22**, 60502 (2017).

22. Greening, G. J., Miller, K. P., Spainhour, C. R., Cato, M. D. & Muldoon, T. J. Effects of isoflurane anesthesia on physiological parameters in murine subcutaneous tumor allografts measured via diffuse reflectance spectroscopy. *Biomed. Opt. Express* (2018) doi:10.1364/boe.9.002871.

23. Dings, R. P. M. *et al.* Scheduling of radiation with angiogenesis inhibitors anginex and avastin improves therapeutic outcome via vessel normalization. *Clin. Cancer Res.* (2007) doi:10.1158/1078-0432.CCR-06-2441.

24. Moeller, B. J., Cao, Y., Li, C. Y. & Dewhirst, M. W. Radiation activates HIF-1 to regulate vascular radiosensitivity in tumors: Role of reoxygenation, free radicals, and stress granules. *Cancer Cell* **5**, 429–41 (2004).

25. Dachs, G. U. & Tozer, G. M. Hypoxia modulated gene expression: Angiogenesis, metastasis and therapeutic exploitation. *Eur. J. Cancer* (2000) doi:10.1016/S0959-8049(00)00159-3.

26. Yeo, E. J. *et al.* YC-1: A potential anticancer drug targeting hypoxia-inducible factor 1. *J. Natl. Cancer Inst.* (2003) doi:10.1093/jnci/95.7.516.

27. Vishwanath, K. *et al.* Quantitative optical spectroscopy can identify long-term local tumor control in irradiated murine head and neck xenografts. *J. Biomed. Opt.* **14**, 054051 (2009).

28. Stadler, P., Feldmann, H. J., Creighton, C., Kau, R. & Molls, M. Changes in tumor oxygenation during combined treatment with split- course radiotherapy and chemotherapy in patients with head and neck cancer. *Radiother. Oncol.* (1998) doi:10.1016/S0167-8140(98)00032-2.

29. Olive, P. L. Radiation-induced reoxygenation in the SCCVII murine tumour: evidence for a decrease in oxygen consumption and an increase in tumour perfusion. *Radiother. Oncol.*

(1994) doi:10.1016/0167-8140(94)90447-2.

30. Lyng, H., Tanum, G., Evensen, J. F. & Rofstad, E. K. Changes in oxygen tension during radiotherapy of head and neck tumours. *Acta Oncol. (Madr).* (1999) doi:10.1080/028418699432329.

31. Dietz, A. *et al.* Prognostic impact of reoxygenation in advanced cancer of the head and neck during the initial course of chemoradiation or radiotherapy alone. *Head Neck* **25**, 50–8 (2003).

32. Chandel, N. S. *et al.* Reactive oxygen species generated at mitochondrial Complex III stabilize hypoxia-inducible factor-1α during hypoxia: A mechanism of O2 sensing. *J. Biol. Chem.* **279**, 25130–8 (2000).

33. Lee, D. E. *et al.* A Radiosensitizing Inhibitor of HIF-1 alters the Optical Redox State of Human Lung Cancer Cells in Vitro. *Sci. Rep.* **8**, 8815 (2018).

34. Secomb, T. W., Hsu, R., Ong, E. T., Gross, J. F. & Dewhirst, M. W. Analysis of the effects of oxygen supply and demand on hypoxic fraction in tumors. *Acta Oncol. (Madr).* (1995) doi:10.3109/02841869509093981.

35. Crokart, N. *et al.* Early reoxygenation in tumors after irradiation: Determining factors and consequences for radiotherapy regimens using daily multiple fractions. *Int. J. Radiat. Oncol. Biol. Phys.* (2005) doi:10.1016/j.ijrobp.2005.02.038.

36. Crokart, N. *et al.* Glucocorticoids modulate tumor radiation response through a decrease in tumor oxygen consumption. *Clin. Cancer Res.* (2007) doi:10.1158/1078-0432.CCR-06-0802.

37. Diepart, C. *et al.* Arsenic trioxide treatment decreases the oxygen consumption rate of tumor cells and radiosensitizes solid tumors. *Cancer Res.* (2012) doi:10.1158/0008-5472.CAN-11-1755.

38. Benej, M. *et al.* Papaverine and its derivatives radiosensitize solid tumors by inhibiting mitochondrial metabolism. *Proc. Natl. Acad. Sci. U. S. A.* (2018) doi:10.1073/pnas.1808945115.

39. Gorski, D. H. *et al.* Blockade of the vascular endothelial growth factor stress response increases the antitumor effects of ionizing radiation. *Cancer Res.* (1999).

40. Gupta, V. K. *et al.* Vascular endothelial growth factor enhances endothelial cell survival and tumor radioresistance. *Cancer J.* (2002) doi:10.1097/00130404-200201000-00009.

41. Sunar, U. *et al.* Noninvasive diffuse optical measurement of blood flow and blood oxygenation for monitoring radiation therapy in patients with head and neck tumors: a pilot study. *J. Biomed. Opt.* (2007) doi:10.1117/1.2397548.

42. Ohmae, E. *et al.* Comparison of lipid and water contents by time-domain diffuse optical spectroscopy and dual-energy computed tomography in breast cancer patients. *Appl. Sci.* (2019) doi:10.3390/app9071482.

43. Tromberg, B. J. *et al.* Predicting responses to neoadjuvant chemotherapy in breast cancer: ACRIN 6691 trial of diffuse optical spectroscopic imaging. *Cancer Res.* **76**, 5933–44 (2016).

44. Tomaszewski, M. R. *et al.* Oxygen enhanced Optoacoustic Tomography (OE-OT) reveals vascular dynamics in murine models of prostate cancer. *Theranostics* **7**, 2900–2913 (2017).

45. Tomaszewski, M. R. *et al.* Oxygen-enhanced and dynamic contrast- enhanced optoacoustic tomography provide surrogate biomarkers of tumor vascular function, hypoxia, and necrosis. *Cancer Res.* (2018) doi:10.1158/0008-5472.CAN-18-1033.

46. Ghosh, P. *et al.* Oxygen-Enhanced Optoacoustic Tomography Reveals the Effectiveness of Targeting Heme and Oxidative Phosphorylation at Normalizing Tumor Vascular Oxygenation. *Cancer Res.* (2020) doi:10.1158/0008-5472.can-19-3247.

47. Zackrisson, S., Van De Ven, S. M. W. Y. & Gambhir, S. S. Light in and sound out: Emerging translational strategies for photoacoustic imaging. *Cancer Research* (2014) doi:10.1158/0008-5472.CAN-13-2387.

48. Rich, L. J. & Seshadri, M. Photoacoustic monitoring of tumor and normal tissue response to radiation. *Sci. Rep.* (2016) doi:10.1038/srep21237.

49. Paidi, S. K. *et al.* Label-free Raman spectroscopy reveals signatures of radiation resistance in the tumor microenvironment. *Cancer Res.* **79**, 2054–64 (2019).

50. Majumder, S. K., Keller, M. D., Boulos, F. I., Kelley, M. C. & Mahadevan-Jansen, A. Comparison of autofluorescence, diffuse reflectance, and Raman spectroscopy for breast tissue discrimination. *J. Biomed. Opt.* (2008) doi:10.1117/1.2975962.

51. Chang, S. K. *et al.* Combined reflectance and fluorescence spectroscopy for in vivo detection of cervical pre-cancer. *J. Biomed. Opt.* (2005) doi:10.1117/1.1899686.

52. Georgakoudi, I. *et al.* Trimodal spectroscopy for the detection and characterization of cervical precancers in vivo. *Am. J. Obstet. Gynecol.* (2002) doi:10.1067/mob.2002.121075.

Table 1. Tumor distribution in different groups in radiation-response study.

Cell line	Treatment	No. of mice	No. of tumors
UM-SCC-22B	NT	13	24
	XT	24	24
UM-SCC-47	NT	12	22
	XT	19	19
Total		68	89

Table 2. Tumor distribution in different groups for immunohistochemistry

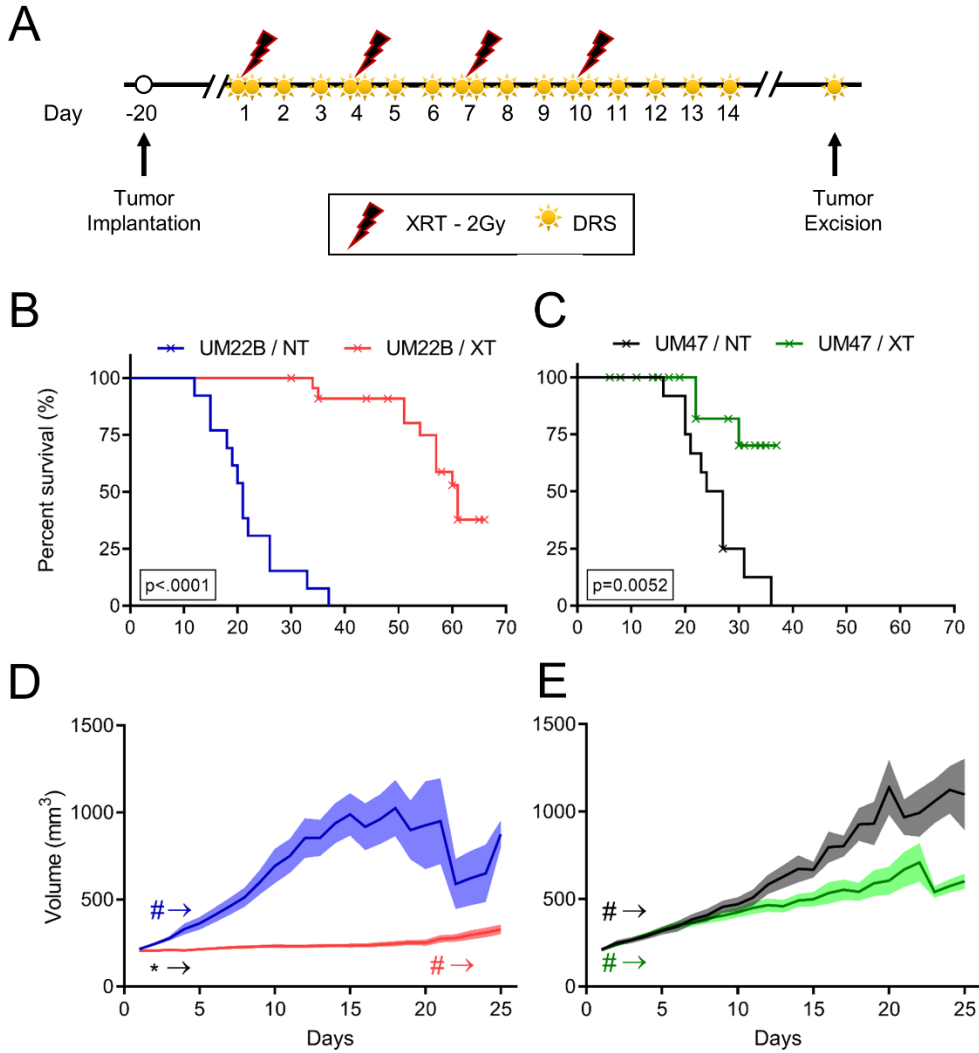| Cell line	Treatment	Baseline	24h	48h
UM-SCC-22B	NT	7	5	5
	XT		5	5
UM-SCC-47	NT	4	3	3
	XT		4	4

Figure 1. Study design for radiation-resistant and -sensitive tumors. A, Timeline for the schedule of fractionated radiation and spectroscopic measurement. The lightning bolt signs indicate days of each fractions of radiation. Yellow sun signs indicate acquisition of optical spectra from the animals. On days of radiation, DRS spectra were collected immediately before and one hour after radiation. Comparison of the survival rate for control (NT) and irradiated (XT) animals bearing UM-SCC-22B (B) and UM-SCC-47 (C) tumors. P values based on log-rank test. Censored data points illustrated by x sign. Tumor growth kinetics (D&E) are observed to identify radiation response of NT and XT groups among UM-SCC-22B and UM-SCC-47 tumors. Data are presented as group mean (line) ± SEM (semitransparent shadow). Significant differences among NT and XT treatments in specific days are illustrated with black asterisks (*) while significant differences of specific days with respect to their own value in day 1 are illustrated using pounds (#). Arrows adjacent to the significance signs are indication of presence of significance until the end of study. * and # indicate statistical significance at p<0.05.
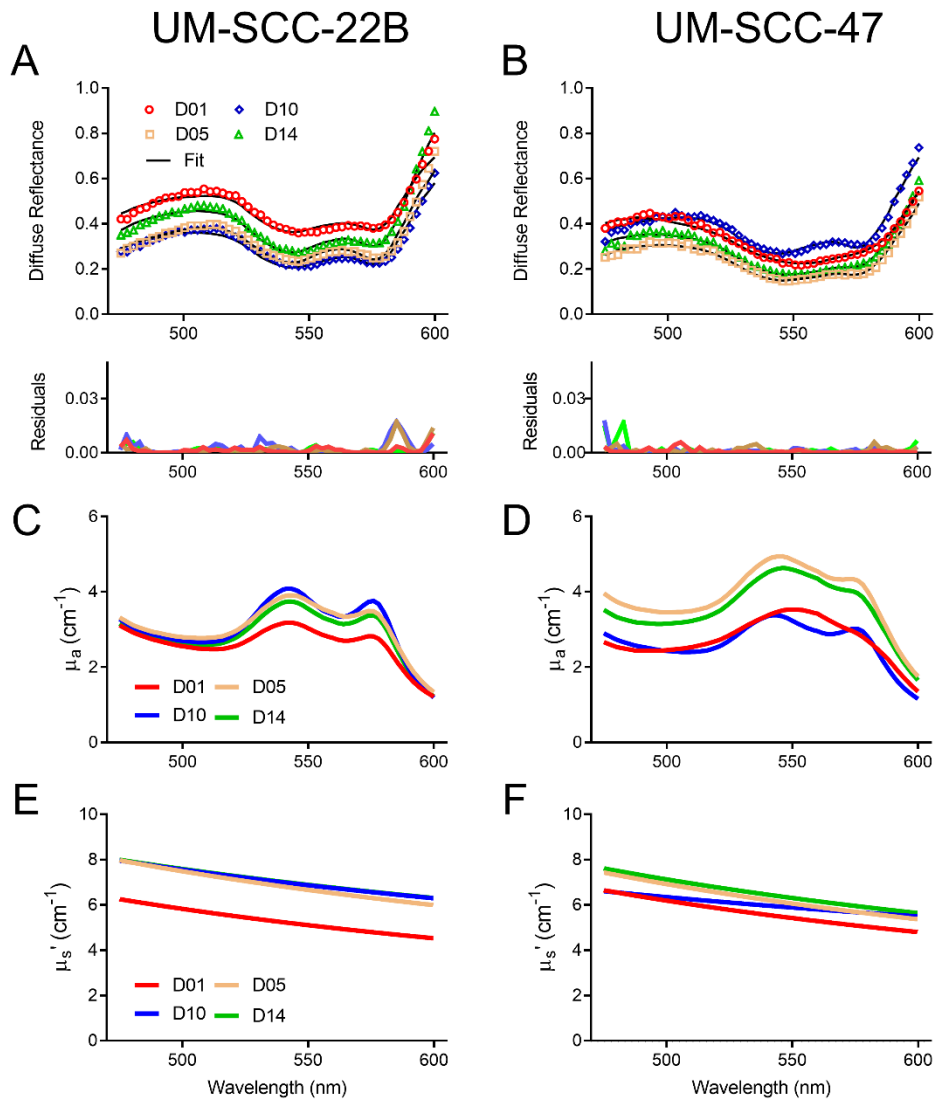
Figure 2. Representative DRS spectra, residuals, and extracted absorption and scattering coefficients. DRS spectra of UM-SCC-22B (A) and UM-SCC-47 (B) tumors on day1 (red circles), day5 (yellow squares), day10 (blue diamonds), day14 (green triangles), and their corresponding LUT fit (black solid line). Representative spectra collected from animals in XT groups. The perfect agreement between the measured data and their fits is also illustrated. Extracted absorption and scattering coefficients are illustrated in figure D-F.
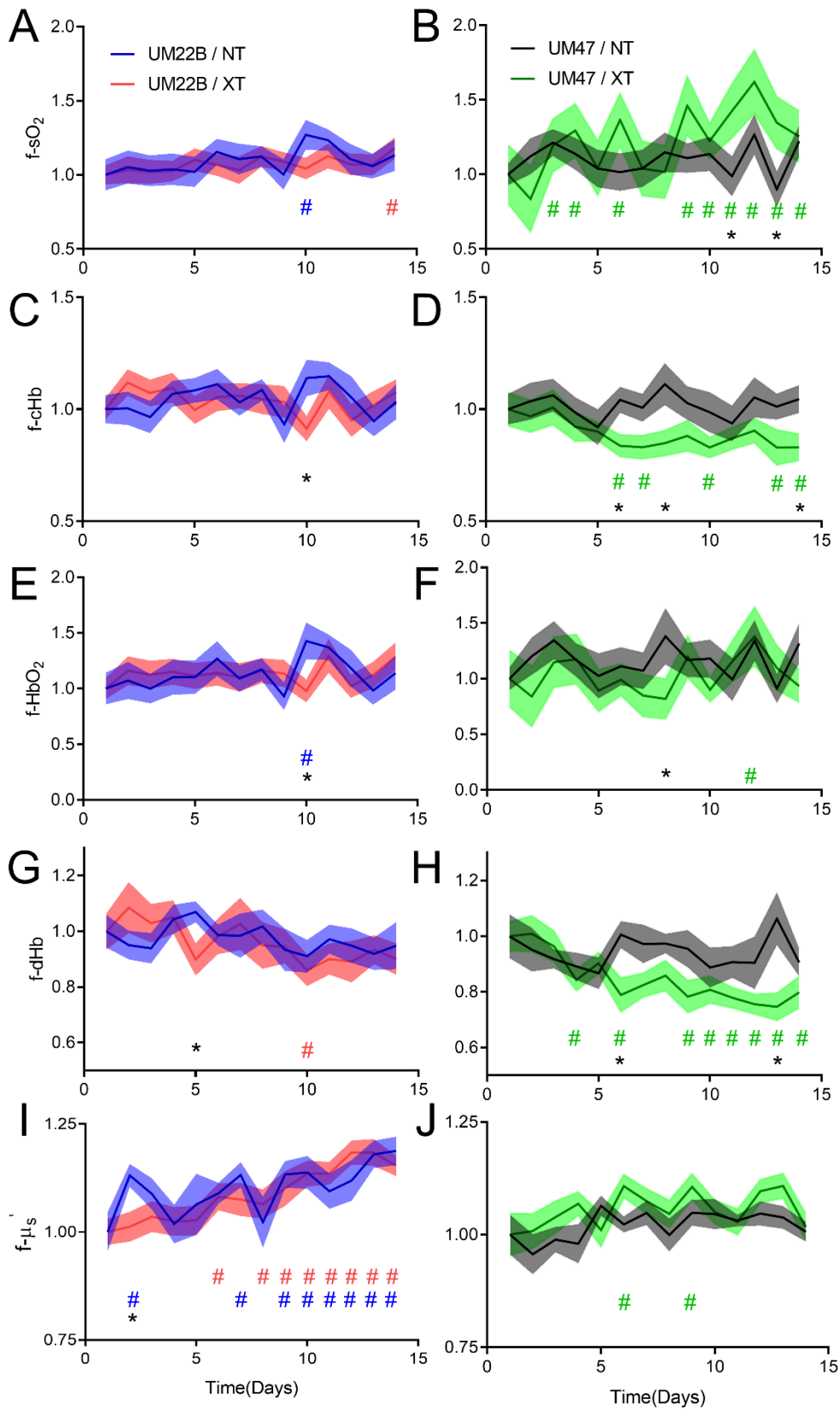
Figure 3. Fold change in hemoglobin oxygen saturation sO_2 (A&B), total hemoglobin concentration cHb (C&D), oxygenated hemoglobin HbO_2 (E&F), deoxygenated hemoglobin dHb (G&H), and reduced scattering coefficient μ_s' (I&J) are observed over time to identify biomarkers of radiation-resistance. Data are presented as group mean (line) ± SEM (semitransparent shadow). Significant differences among NT and XT treatments in specific days are illustrated with black asterisks (*) while significant differences of specific days with respect to their own value in day 1 are illustrated using pounds (#). * and # indicate statistical significance at $p < 0.05$.
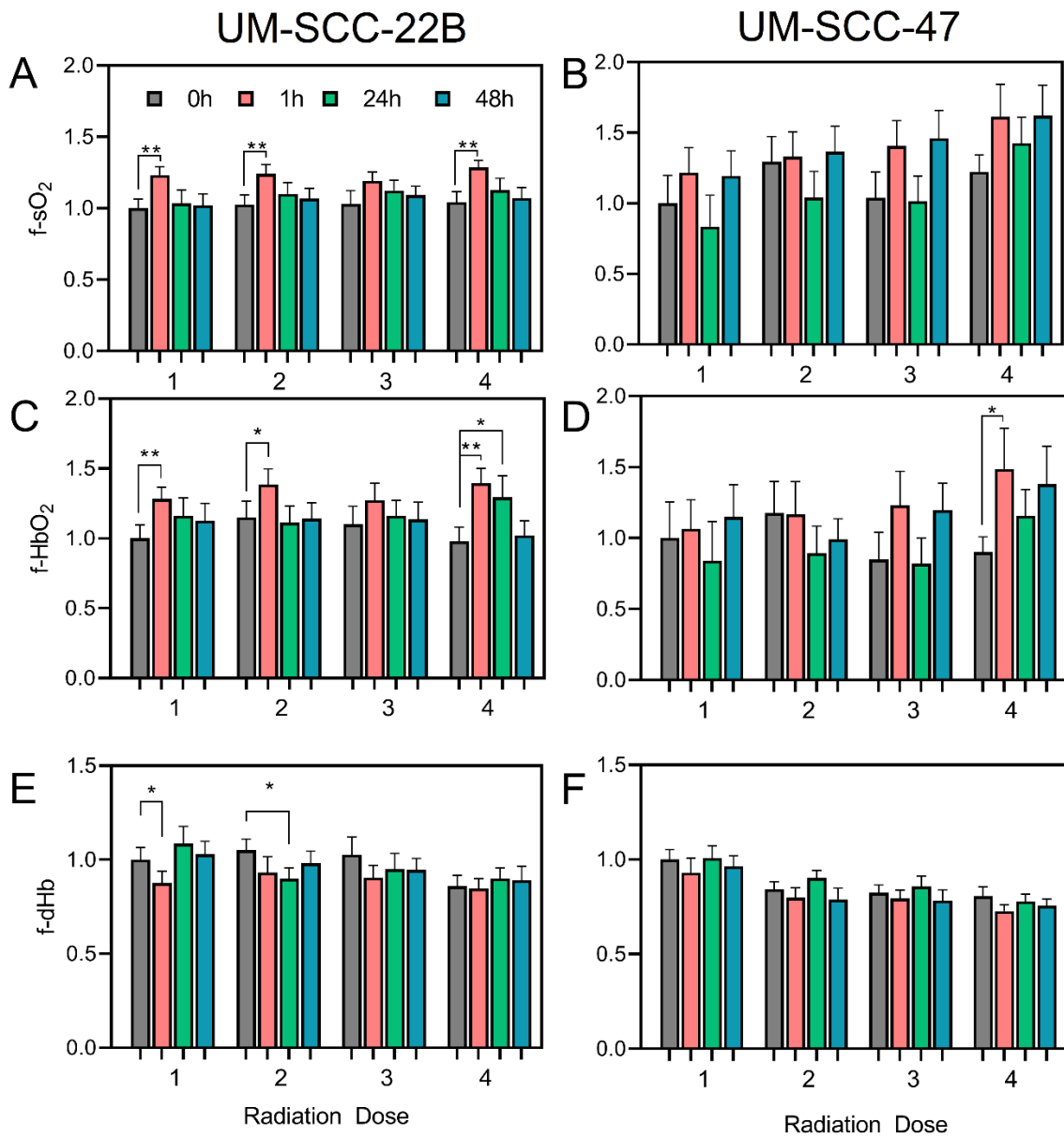
Figure 4. Temporal changes in optical properties in response to 4 doses of radiation. Fold-changes in sO_2 (A, B), HbO_2 (C, D), and dHb (E, F) in response to 4 doses of radiation are illustrated at 4 time points: before (gray), 1h (red), 24h (green), and 48h (blue) after radiation. Data are presented as group mean + SEM. * and ** respectively indicate $p < 0.05$ and $p < 0.01$.
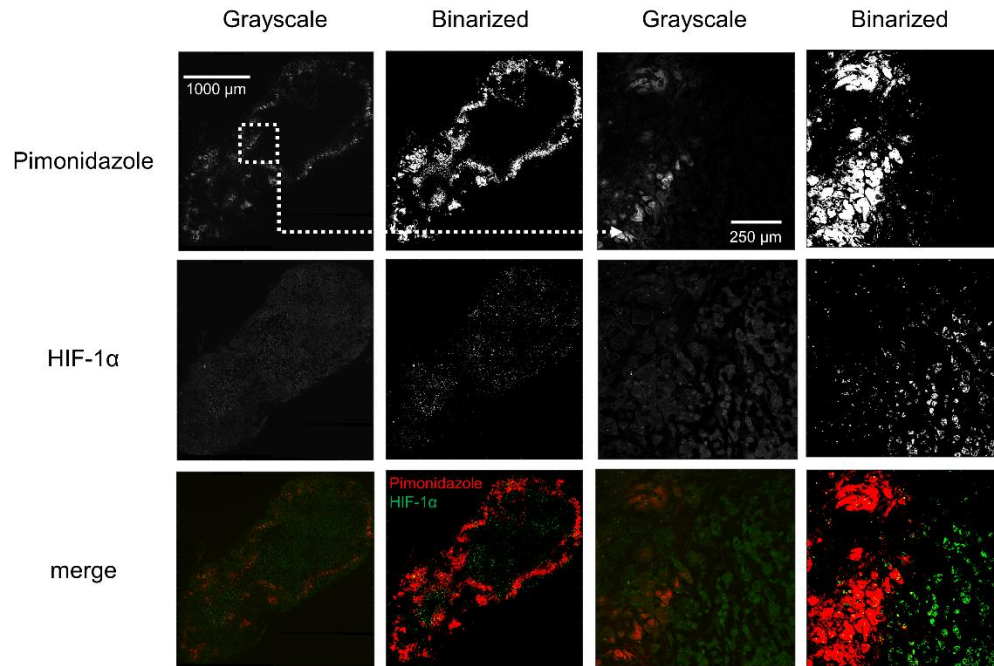
Figure 5. Double-staining of Pimonidazole and HIF-1α from a representative UM-SCC-47 tumor excised 24 hours after radiation. The acquired images were binarized using a fixed threshold.

Figure 6. Immunohistochemical assessment of tumor hypoxia and HIF-1α in tumor tissue sections. A, Representative images from UM-SCC-22B and UM-SCC-47 tumors excised at baseline, 24, and 48 hours after radiation. The false-colored red and green signals respectively represent Pimonidazole positive and HIF-1α positive pixels. The scale bar represents 250 μm. Quantification of percentage of Pimonidazole positive and HIF-1α positive pixels in UM-SCC-22B and UM-SCC-47 tumors at baseline (B) and following time points (C&D).
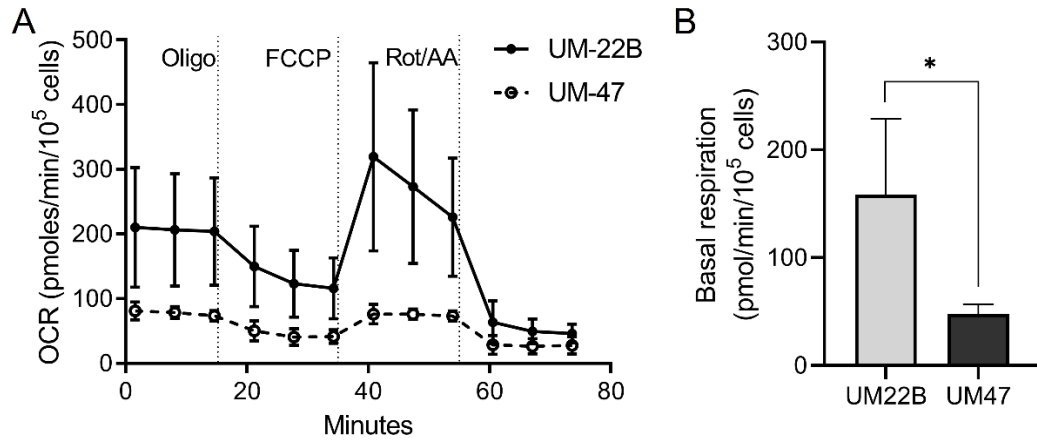
Figure 7. Basal oxygen consumption rate measured by Seahorse metabolic flux assay according to manufacturer's protocol. * indicate statistically significant difference according to Wilcoxon rank sum test. Error bars represent standard deviation from the mean of 3 plate value.

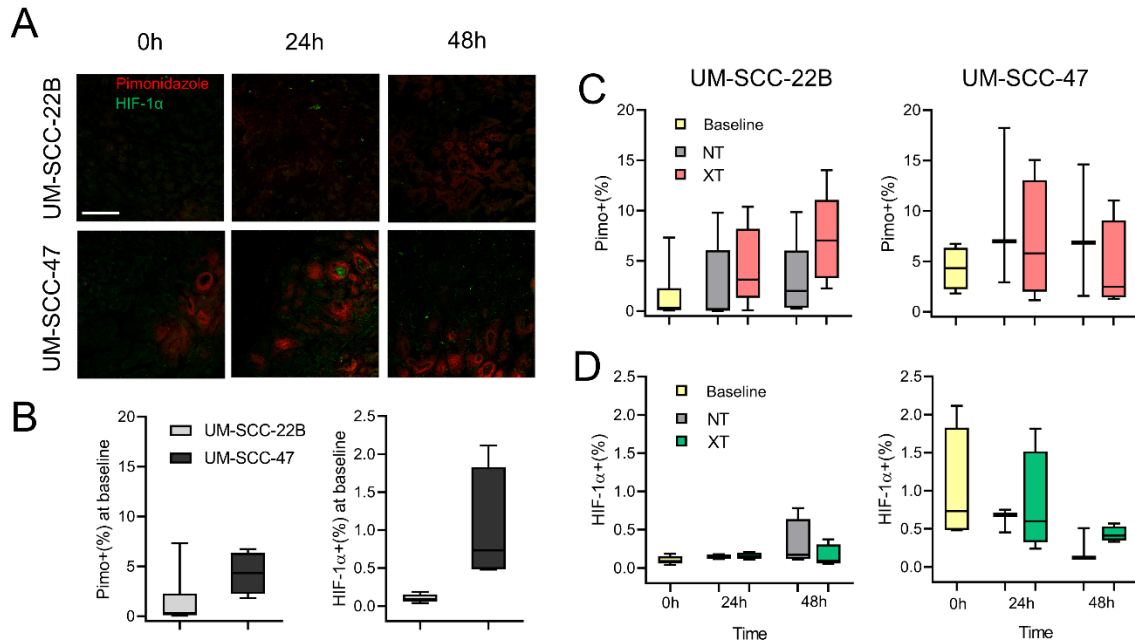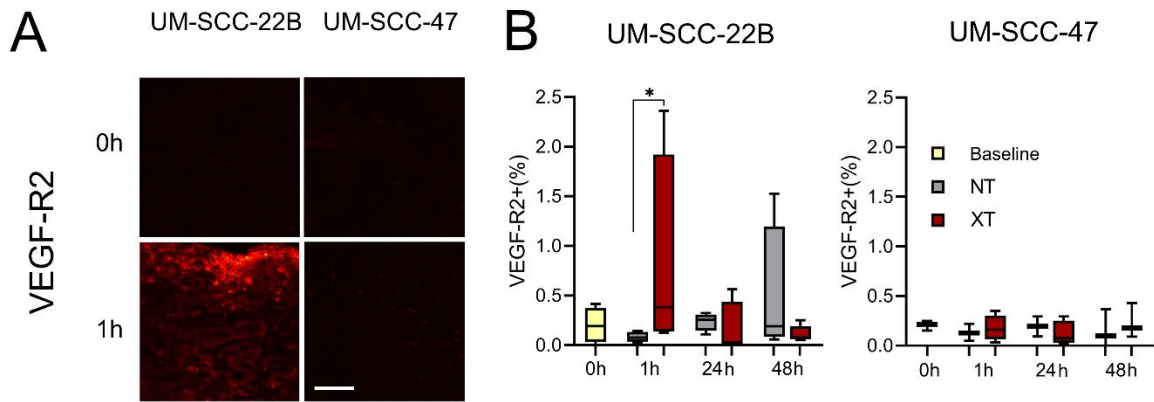Figure 8. Immunohistochemical assessment of VEGF-R2 in tumor tissue sections. A, Representative images from UM-SCC-22B and UM-SCC-47 tumors excised at baseline and 1 hours after radiation. The false-colored red signal represents VEGF-R2 positive pixels. The scale bar represents 250 μm. Quantification of percentage of VEGF-R2 positive pixels in UM-SCC-22B and UM-SCC-47 tumors (B).
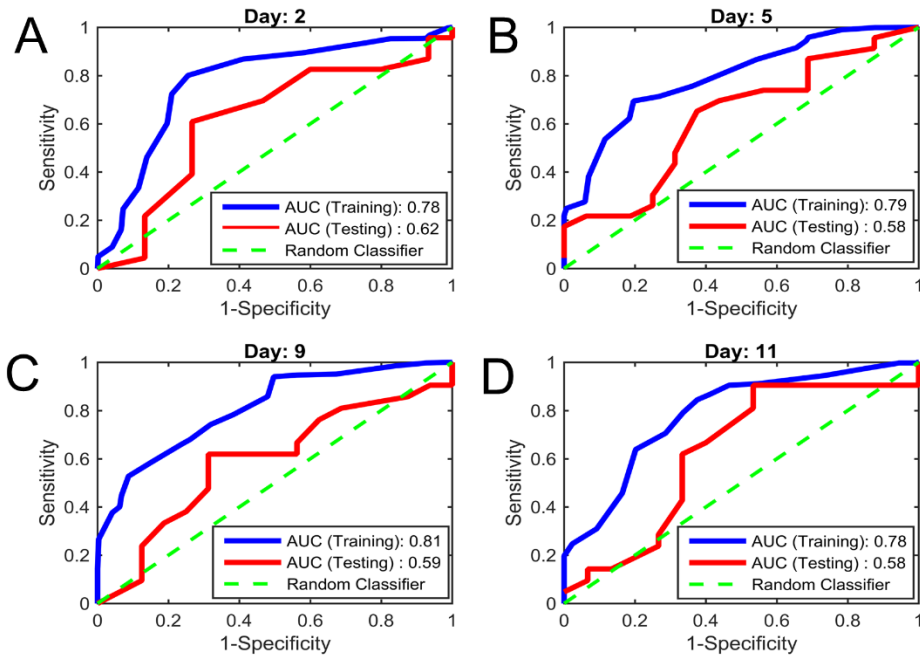
Figure 9. Accuracy of local-control and treatment-failure classification performed by logistic regression is presented. Daily ROC curved are generated from leave-one-out analysis.

Chapter 4: Raman spectroscopic investigation of radiation-induced biochemical changes in tumor microenvironment of head and neck tumor xenografts

Introduction

Tumor hypoxia and hence changes in oxygenation have been extensively studied in the context of radiation therapy due to the role of oxygen in mediating radiation-induced cell death. Several preclinical and clinical studies have explored the utility of using oxygen-sensing microelectrodes[1] or noninvasive diffuse optical spectroscopy[2–5] (as already extensively discussed in Chapters 1 and 2) to measure tumor hypoxia as well as radiation-induced changes in oxygenation and hence, predict treatment outcome. However, in addition to tumor oxygenation, radiation therapy can also induce biomolecular alterations in tumor microenvironment that might be associated with treatment response or resistance. Such biomolecular alterations can be measured with Raman spectroscopy (RS).

RS is an optical technique that can provide quantitative and chemically-specific information about biomolecular changes of the host cells and tissues. RS is based on in-elastic scattering of photon after its interaction with a vibrating molecule[6]. The energy difference among the incident photon on the sample and its in-elastically scattered version is equal to the required energy to excite the specific vibration of a specific molecule. Thus, biological molecules with unique chemical features can be identified without exogenous dyes and changes in their content can provide pathological information[7]. RS has primarily been studied within the sphere of cancer detection and margin analysis. For example, Haka *et al* have used *in vivo* RS measurements for intra operative margin assessment during partial mastectomy of breast cancer patients and have shown perfect sensitivity and specificity in stratification of tumor lesions healthy normal tissue[8]. Similar results have also been shown for cancers of oral cavity, cervix, and brain[6,9,10]. More recent studies have utilized RS in studying radiation-induced spectral alterations in *in vivo* cell cultures and *ex vivo* tumor samples. Yasser *et al* have identified spectral differences associated with

proteins, lipid, and nucleic acids between parental and radio-resistant sublines of oral cancer cell lines[11]. Matthews *et al* have investigated radiation-induced biomolecular changes of glycogen accumulation in radio-resistant cancer cells and have shown that such accumulation can be inhibited via glycogen synthesis inhibitor, metformin[12]. In addition, RS application in detection of biomolecular changes in excised radiated tumor xenografts have also been shown[13,14].

In a very recent study, we investigated the utility of RS in identifying radiation-induced changes in excised lung and head & neck tumor xenografts and observed consistent differences in lipid and collagen content between radiation-resistant and -sensitive tumors[15]. Although our results featured RS as a powerful tool in studying radiation-induced changes in tumor microenvironment, the tumor xenografts used in our previous study were excised 35-50 days after tumor inoculation and radiation. Here, we sought to investigate whether *in vivo* Raman spectroscopy is sensitive to early radiation-induced microenvironmental alterations. To this end, we used head and neck UM-SCC-22B and UM-SCC-47 cell lines, with known radiosensitivity[16] in formation of our tumors and treated tumor xenografts with a single dose of 2 Gy[5]. We performed *in vivo* Raman spectroscopy on tumors and analyzed collected Raman spectra using multivariate curve resolution-alternating least squares (MCR-ALS) to uncover biomolecular changes within the tumor microenvironment. We observed radiation-induced increase in lipids and collagen respectively in radiation-sensitive and -resistant tumors. Our results underline the sensitivity of Raman spectroscopy to early radiation-induced microenvironmental changes. Longitudinal RS measurements that associate these changes with treatment response of individual tumors could shed further light in microenvironmental characteristics of radiation-resistant tumors and can potentially serve as biomarkers of radiation-response.

Materials and Methods

Aqueous solutions

Three solutions of metabolites containing lactate, glucose, and combination of lactate and glucose were prepared in distilled water as following. Glucose-only solution was prepared by dissolving 500 mg of D-(+)-Glucose (G8270 – Sigma Aldrich) in 10 mL of distilled water to achieve a concentration of 50 g/L. This concentration was chosen to represent 5% of the maximum solubility of D-glucose in distilled water. Lactate-only solution on the other hand, was prepared by mixing 0.414 mL (equivalent of 500 mg at density of 1.206 g/mL) of Lactic acid solution (L1875 – Sigma Aldrich) with 10 mL of distilled water. This was performed to ensure equal concentrations for lactate-only and glucose only solutions. Finally, to create the solution consisting of both D-Glucose and Lactate, 500 mg of D-Glucose was dissolved in 10 mL of Lactic acid solution.

Cells, tumors, and radiation treatment

Cell culture conditions and tumor xenografts formation have previously been described in chapter 2 in detail. Tumor growth of all mice were monitored daily and animals were randomly distributed to one of the treatment (control or a single dose of 2 Gy of radiation) and time points (Baseline, 1, 24, and 48 hours after radiation) once their volume reached 200 mm^2 (See tumor distribution in Table 1). Treatment of 2 Gy was delivered using an X-rad 320 biological cabinet (Precision X-Ray, North Branford, CT) while the entire animal body was covered under lead blocks except the tumor. During radiation, mice were kept under anesthesia using a mixture of isoflurane (1.5% v/v) and 100% oxygen. This study was approved by the Institutional Animal Care & Use Committee (IACUC) at University of Arkansas (Protocol number: 18061).

Raman spectroscopy

Prior to *in vivo* Raman spectroscopic measurements, tumor bearing animals were anesthetized and the skin tissue covering the tumor was surgically removed. Great care was taken to prevent damaging tumor microenvironment and cause unintended bleeding. The bare

tumor was brought into contact with a fiber-optic-probe to perform Raman spectroscopic measurement. After acquisition of Raman spectra, tumors were excised, and animals were euthanized. Our Raman system has been described previously[15]. Briefly, this system included a diode laser emitting at 830 nm (500 mW maximum power, Process Instruments, Salt Lake City, UT) for excitation and an imaging spectrograph (Holospec f/1.8i, Kaiser Optical Systems, Ann Arbor, MI) with a thermoelectrically cooled CCD camera (LS 785, Princeton Acton) for spectral acquisition. A 2 mm flexible custom-made fiber probe (EmVision LLC - Loxahatchee, FL) was used for light delivery through an excitation fiber located at the center of the probe. The excitation fiber was terminated with a short-pass filter which transmits laser light and attenuates longer wavelengths. This fiber is surrounded with 15 collection fibers annularly located at approximately 800 μm away from the central excitation fiber. The collection fiber is also preceded with a long-wavelength pass filter transmitting tissue's Raman spectrum and blocking backscattered light. Finally, a sapphire ball lens was placed after the short- and long-pass filters creating a distance of 1 mm between the optical fibers and the ball lens to ensure collimation of the excitation light (for reducing the incident energy and preventing tissue damage) and maximal coupling of the in-elastically scattered light into the collection fibers[17]. The estimated sampling volume achieved by this probe is 1 mm^3. We used this setup to collect 50 Raman spectra with acquisition time of 1 second from spatially distinct locations on the tumor to account for tissue heterogeneity. For measurements from aqueous solutions, the fiber probe was placed within the aqueous solution. 2350 spectra from 47 tumors and 2400 spectra from 3 aqueous solutions were acquired.

Data analysis

Saturated spectra and spectra contaminated with cosmic rays were visually identified and removed from the dataset. Prior to any further processing, the wavenumber axis of the acquired Raman spectra were shifted according to spectral peaks of 4-acetamidophenol. Further data pre- and post-processing was limited to only fingerprint region (600-1800 cm^{-1}). Next, tissue

fluorescence was removed by subjecting the recorded Raman spectra to a fifth-order polynomial algorithm. To neutralize potential variations in laser power, baseline-corrected spectra were then normalized such that their sum of squares is set to unity. Next, the normalized spectra were subjected to median-filtering to remove random spikes induced by cosmic rays to avoid overlaying of cosmic rays with biological signal. We decomposed the spectral data and recovered the spectral profiles (loadings) and the abundance (scores) of the biochemical constituent of biological specimen using multivariate curve resolution-alternating least squares (MCR-ALS) without prior knowledge of the content of the specimen[18]. Loadings and scores were limited to nonnegative values in decomposition of the normalized spectra through an iterative optimization routine until convergence was achieved. All data pre-processing and analysis was conducted using MATLAB (Mathworks, Natick, MA).

Immunohistochemistry and histology

We sliced flash-frozen tumors into sections of 10 μm using a cryostat (CM 1860; Lecia, Inc., Nussloch, Germany). Immunofluorescence procedure has been described recently[5]. Briefly, tumor sections were hydrated in PBS, fixed with 4% PFA, permeabilized using 0.5% Triton-X 100, and incubated using an in-house blocking solution (95% PBS + 4% goat serum + 1% sodium azide) for an hour. Next, slides were incubated with Fatty acid synthase (3180S – Cell Signaling, Danvers, MA) antibody for 3 hours at room temperature. The slides were next tagged with Alexa Fluor 488 goat anti-Rabbit (4412S – Cell Signaling). Immunostained tumor sections of all the slides were imaged using a confocal microscope (Fluoview FV10i, Olympus) using a 10X objective (UPLSAPO10X, NA = 0.4, Olympus). The microscope software enabled stitching individual images acquired from different regions of interest (ROI) into one single image which encompassed entire tissue section. Signal of acquired images were compared to background intensity using histogram, and a fixed threshold was used in separating pixels containing true signal from the background. Possible presence of non-specific binding and endogenous tissue

autofluorescence were respectively investigated by imaging slides incubated with no antibodies and slides incubated with secondary antibody only. Both were found to be absent. Finally, percentage of FASN positive pixels within each tissue section was calculated by dividing segmented pixels by the total number of tumor tissue pixels.

In addition to immunohistochemical assessment of FASN, we also performed Masson's trichrome staining for collagen on serial slides of same tumors. Slides were imaged using a 10X objective on a Nikon fluorescence microscope and images acquired from different regions of interest were stitched using Fiji – ImageJ.

Statistical analysis

We performed Shapiro-Wilk W test to identify whether MCR and immunohistochemical data were normally distributed. The null hypothesis was rejected for both data sets. Thus, statistically significant differences between medians of various groups were assessed based on a Wilcoxon rank sum test. All tests employed a 2-sided $p<0.05$ significance level. In addition to performing statistical analysis on MCR-scores of lipid and collagen, we used Wendt formula to calculate the effect size of comparisons among various treatments and time points[19]. All statistical analyses were performed using JMP (The SAS Institute, Cary, NC).

Results

We first sought to investigate the accuracy of MCR-ALS model in decomposition and extraction of MCR-coefficients and -scores from Raman spectra of aqueous solutions with known content. We made three different solutions containing Lactate (L), Glucose (G), and combination of Lactate and Glucose (G+L, Figure 1A). Pre-processed Raman spectra of three different solutions are illustrated in Figure 1B where each spectrum is average of 800 spectral measurement from specific solution. Spectral averaging was performed for visualization purposes only. Entire Raman spectral dataset were decomposed using MCR-ALS without any mathematical manipulation (e.g. group averaging) and MCR-scores containing "pure" spectral components

were extracted (Figure 2C). As expected, we identified only two "pure" components that strongly resembled the characteristics of Raman spectra of Lactate and Glucose (spectral variance = 99.998%). The extracted "pure" components closely resembled Raman spectra of pure lactate and glucose[20,21]. Finally, we investigated the quantitative scores of glucose and lactate from individual measurements of L, G, and L+G solutions (Figure 2D). We observed high, low, and intermediate lactate-related MCR-scores respectively from L, G, and L+G solutions. Furthermore, we observed low, high, and intermediate glucose-related MCR-scores respectively from L, G, and L+G solutions. These results indicate that based on lactate- and glucose-related MCR scores, L, G, and L+G solutions can be accurately differentiated with MCR-ALS algorithm.

Having confirmed the accuracy of MCR-ALS algorithm in identifying the content of solutions with no *a priori* information provided, we next sought to decompose spectral data acquired from *in vivo* animal measurements. Raw Raman spectra of different tumor types and treatments are shown in Figure 2A. The autofluorescence of the spectra shown here were removed via background subtraction in pre-processing steps. Each spectral map contained > 350 spectra. Regardless of tumor type and treatment, all tumor classes show prominent peaks at 1301 cm^{-1} (CH vibration of lipids), 1448 cm^{-1} (CH$_2$ bending modes in lipids and collagen) and 1656 cm^{-1} (C = C stretching in lipids). Although we observed no visually identifiable spectral variations among the four groups, we hypothesized that a subset of pixels representing specific molecular moieties have predictive power but is lost in averaged Raman spectra among different groups of each cell line. We next decomposed the animal Raman spectra using MCR-ALS algorithm and obtained three 'pure' coefficients. Figure 2B illustrates the three MCR-coefficients that represent key tumor constituents of control (NT) and radiated (XT) UM-SCC-22B and UM-SCC-47 tumors. As seen in Figure 2B, MCR-coefficient B1 contains prominent peaks at 1078 cm^{-1}, 1266 cm^{-1}, 1301 cm^{-1}, 1442 cm^{-1}, and 1654 cm^{-1} all of which are characteristics of lipids[22]. MCR-coefficient B2 contains spectral peaks at 928 cm^{-1}, 1040 cm^{-1}, 1251 cm^{-1}, 1315 cm^{-1}, 1453 cm^{-1}, and 1661

cm[-1] which closely resemble characteristics of collagen[23,24]. In addition, the spectra pattern B3 contains spectral peaks belonging to combination of collagen and nucleic acid. In addition to recovering MCR-coefficients of contributing biological moieties, we also extracted the scores matrix (MCR-scores) that contained the weight (abundance) of each of the MCR-coefficients for all the acquired Raman spectra. Using these scores, we then quantitatively compared the lipid- and collagen-related MCR-scores of NT and XT tumors from UM-SCC-22B and UM-SCC-47 groups. We observed higher values of lipid-related MCR scores in radiated group (XT) of UM-SCC-22B tumors. Although statistically significant differences were not detected, we identified an effect size of 0.52 among these two groups indicating that 52% of XT tumors had higher lipid-related MCR scores in comparison to NT tumors. In contrast, control and radiated UM-SCC-47 tumors had similar MCR-scores of lipid with smaller effect size (r=0.07). Similar results were observed for collagen scores of UM-SCC-22B tumors (r=0.08). However, radiated UM-SCC-47 tumors exhibited greater collagen-related MCR scores in comparison to control tumors (r=0.37) although no statistical significance was observed (figure 2C).

Having identified the generic differences in lipid- and collagen -related MCR scores in NT and XT groups of different tumor types, we next sought to identify the kinetics of these changes over the next 48 hours after radiation (Figure 3). Tumors undergoing a single dose of 2 Gy (XT – red boxes) and control tumors (NT – gray boxes) were subjected to Raman spectral measurements at baseline, 1, 24, and 48 hours after treatment. We observed an increase in lipid-related MCR scores in UM-SCC-22B tumors. NT and XT groups at 1- and 24-hours post-radiation had higher values of lipid-related MCR scores with respect to the baseline. In addition, we observed higher lipid-related MCR scores between NT and XT groups at 1 hour and 24 hours after radiation time points. In contrast, radiation-resistant UM-SCC-47 tumors did not exhibit temporal changes in lipid-related MCR score although we observed larger MCR-score in XT groups at 1 and 24 hours after radiation time points. In addition to lipids, we observed higher levels of collagen-related MCR scores at 1 and 24 hours after radiation time points in UM-SCC-

47 tumors. However, it must be noted that we did not observe any statistically significant differences in anytime points. In addition, due to small sample size associated with each group, we did not perform analysis on effect size because any result can be driven by very limited number of animals distributed to each group.

Fatty acid synthase (FASN) is a key lipogenic enzyme that is responsible for endogenous synthesis of fatty acids[25] and has been linked to radiation resistance[26,27]. Thus, we investigated the presence and extent of FASN expression in our tumors in the first 48 hours after radiation. Figure 4 presents representative images of immunohistochemical staining of FASN at baseline and 1h after radiation in UM-SCC-22B and UM-SCC-47 tumors (A). Figure 4B illustrates the quantification of immunohistochemical assessment of NT and XT tumors collected at baseline, 1, 24, and 48 h after a single 2 Gy dose of radiation. We noted a significant increase in expression of FASN 1 hour after radiation in radiation-sensitive UM-SCC-22B tumors. In contrast to UM-SCC-22B tumors, we observed no significant changes in expression of FASN in UM-SCC-47 tumors.

Finally, to confirm the accuracy of multivariate analysis of Raman spectra, we compared collagen-related MCR-scores to histologically determined collagen area fraction. Figure 5A presents a representative UM-SCC-22B tumor section stained with Masson's trichrome and its corresponding binarized mask. We identified a non-significant correlation between MCR-scores of collagen with collagen area fraction (r=0.21). Both UM-SCC-22B and UM-SC-47 tumors presented with a wide range of collagen area fraction and collagen-related MCR scores.

Discussion

Better understanding of metabolic alterations that lead to radiation-resistance is crucial for personalization of treatment and identification of radiation-resistant tumors at early time points after treatment commencement. Radiation resistant cancer cells exhibit altered metabolic shift towards glycolytic[28,29] and anabolic pathways[26,27] to produce energy and synthesis of lipids in order to ensure rapid tumor growth and avoid cell death. One significant driving factor for this

glycolytic shift is hypoxia and its transcription factor, hypoxia-inducible factor-1α (HIF-1α), a phenotype associated with higher mortality[30–32] and a predictive/prognostic biomarker of radiation response[33,34]. Stabilization of HIF-1 also promotes glycolytic activity[35]. As discussed in previous chapter, greater HIF-1 expression as well as lower optical redox ratio (ORR) have been identified in radiation-resistant lung cancer cell line[28], a results which were reversed by chemical inhibition of HIF-1[29]. In addition to inducing glycolytic changes in tumors, radiation can also alter tumor microenvironmental content. we recently used Raman spectroscopy to study radiation-induced biochemical changes in tumor microenvironment of lung and head and neck tumor xenografts. On *ex vivo* tumors excised 35-50 days after radiation, we have identified HIF-1 targets, lipid and collagen, to be significantly higher in radiation-sensitive tumors compared with radiation-resistant tumors[15]. Our long-term clinical goal is to investigate whether Raman spectroscopy can differentiate radiation-responder and non-responder patients during the first days of treatment. Here, we sought to test the sensitivity of label-free Raman spectroscopy to early radiation-induced biomolecular alterations in radiation-resistant and -sensitive tumors.

We observed higher contents of lipid-related MCR-score in 1, 24, and 48 hours after radiation in comparison to baseline in radiation-sensitive tumors. These results are supported by a study by Deng *et al*, where increased lipid content was observed in radiation sensitive LNCaP cell line compared to relatively resistant H460 and MCF7 cell lines[36]. In radiation-sensitive UM-SCC-22B tumors, we additionally observed an increase in FASN one hour after radiation which could be the reason for the observed major increase in lipid-related MCR scores. However, numerous studies have shown lipogenesis inhibition via pharmacological inhibitors or RNA-inhibitor mediated silencing of lipogenic enzymes, FASN and Acetyl-CoA Carboxylase-α, arrests cell proliferation and hence, leads to cell death[37–42]. Rysman *et al* have shown that *de novo* lipogenesis protects cancer cells from insults by free radicals and chemotherapeutics which can be reversed by inhibition of lipogeness[43]. Furdui and colleagues have identified higher expression

of FASN in radiation resistant rSCC-61 cells, inhibition of which results in increased cytotoxicity and sensitivity to radiation[26,27]. Rae and colleagues have shown that inhibition of FASN sensitizes prostate cancer cells to 2 Gy of radiation[44]. Additionally, immunohistochemically determined FASN expression have been associated with tumor progression and survival in neoplasms of ovary[45], melanoma[46], and nephroblastoma[47]. Bensaad *et al* have shown lipid droplet accumulation in hypoxic condition to be HIF-1α dependent and its inhibition profoundly increases ROS toxicity, delays tumor growth, and reduces cell survival[48]. These studies have implied that accumulation of glycolytic intermediates is vital for cell proliferation and survival. Although our findings are in contrast with the mentioned studies, one particular study in neoplastic lesions of oral tongue by Krontiras *et al* noted that FASN expressing tumors had better survival compared to weaker FASN expressing tumors[49] which implies that the relationship between FASN expression and radiation-response is not well-understood and deserves further investigation.

Radiation injury is known to incite an acute response by overexpressing growth factors through macrophages that lead to recruitment and development of fibroblast and myofibroblasts which leads to collagen secretion[50,51]. In addition to collagen deposition induced by radiation, collagen has been identified to protect cancer cells against radiation. *In vitro* studies of renal cell carcinoma have shown that adherence to collagen I protects cancer cells from radiation-induced apoptosis during both normoxic and hypoxic conditions[52]. Collagen deposition has also been known to be driven by hypoxia inducible factors (HIFs). *In vitro* studies of MDA-MB-231 breast cancer cells have shown hypoxia to stimulate prominent collagen cross linking through HIFs, knock downs of which abolished collagen cross linking[53]. These studies are consistent with our findings because as shown in previous chapter, UM-SCC-47 non-responsive tumors have higher content of HIF-1α[5].

Because of the lack of normal distribution of MCR-scores and the fact that some of the investigated time point were assigned with very small number of samples (i.e. n=2), we did not

investigate radiation-induced significant differences between various time points. However, comparison of lipid-related MCR-scores among control and radiated UM-SCC-22B tumors yielded a p value very close to significance (p=0.052). Using Raman spectroscopy at early time points after radiation, several studies have shown significant biomolecular differences in radiation-resistant and -sensitive cells[12,36]. Thus, we hypothesize that increasing sample size in future studies can identify significant biomolecular differences *in vivo* as well.

Although MCR-ALS has widely been used in multivariate analysis in various disciplines, the extracted MCR-scores do not measure the content of actual species of specimen under investigation. Thus, it is important to confirm the accuracy of these findings with controlled experiments. To this end, we performed Raman spectroscopic measurements on aqueous solutions with known content and identified very close agreement between *a priori* known concentrations with MCR-identified contributors. To validate our *in vivo* MCR-findings, we compared collagen-scores of MCR against gold-standard methods of collagen determined from the same tumors. However, we failed to show significant and strong correlations between two factors. In chapter 2 of this dissertation, we performed a similar study where optical findings of tumor oxygenation were confirmed with immunohistochemical measures of hypoxia. Hypoxia on those tumors were specifically investigated in depth of the tumor that corresponded to penetration depth of diffuse reflectance probe. However, for tumors that were used in current study, we failed to track the tumor depth in which histological slides were obtained and hence, there is a very strong possibility that the collected slides were harvested from deeper layers of tumor. This could explain the lack of strong correlation between the two parameters. Thus, any future studies that aim to compare optical findings with tumor histology must ensure to collect slides exactly from the depths that associate with penetration depth of utilized probe.

Other forms of imaging modalities namely, coherent anti-stokes Raman scattering (CARS) and stimulated Raman scattering (SRS) have been used in study of lipid droplets and their role in

cancer progression and metastasis[54,55]. We are particularly intrigued by a study by Zhang *et al* in which SRS was been used to investigate the role of lipid droplets in different metabolic events i.e. lipogenesis vs. lipolysis[56]. However, Raman spectroscopic measurements are sensitive to vibrational modes of numerous other molecules which may contain pathological information about radioresistant phenotype. For example, Matthews *et al* have shown radiation resistant cancer cells to have higher content of glycogen which its pharmacological inhibition results in increased radiosensitivity[12]. Other studies have also suggested that the synthesis of glycogen to be induced in hypoxic conditions through HIF-1 and the accumulation of the glycogen promotes cancer cell survival when exposed to glucose-free medium[57].

In summary, we have used Raman spectroscopy to observe radiation-induced biomolecular alterations in the first 48 hours after a single dose of 2 Gy and identified. Multivariate analysis of acquired Raman spectra revealed increase in lipid and collagen content respectively in radiation-sensitive and -resistant tumors. In a recent study, we have identified higher content of HIF-1α in UM-SCC-47 tumors with respect to UM-SCC-22B tumors in 1 hour after radiation[5]. We reason that the higher content of HIF-1α and FASN in these tumors could be responsible for the observed increase in lipid content. Our future studies include genetic alteration of the pathways that contribute to fatty acid synthesis and collagen breakdown to determine if modification of these pathways lead to corresponding changes in MCR-derived spectral components. Longitudinal confirmatory studies with promising results can open the path for clinical translation of Raman spectroscopy where specific biomolecular-changes can be used as a biomarker of radiation-resistance.

References

1. Nordsmark, M. *et al.* Prognostic value of tumor oxygenation in 397 head and neck tumors after primary radiation therapy. An international multi-center study. *Radiother. Oncol.* (2005) doi:10.1016/j.radonc.2005.06.038.

2. Hu, F. *et al.* Oxygen and Perfusion Kinetics in Response to Fractionated Radiation Therapy in FaDu Head and Neck Cancer Xenografts Are Related to Treatment Outcome. *Int. J. Radiat. Oncol. Biol. Phys.* **96**, 462–9 (2016).

3. Vishwanath, K. *et al.* Quantitative optical spectroscopy can identify long-term local tumor control in irradiated murine head and neck xenografts. *J. Biomed. Opt.* **14**, 054051 (2009).

4. Diaz, P. M. *et al.* Quantitative diffuse reflectance spectroscopy of short-term changes in tumor oxygenation after radiation in a matched model of radiation resistance. *Biomed. Opt. Express* **9**, 3794 (2018).

5. Dadgar, S. *et al.* Spectroscopic investigation of radiation-induced reoxygenation in radiation-resistant tumors. *Neoplasia* **23**, 49–57 (2020).

6. Jermyn, M. *et al.* Intraoperative brain cancer detection with Raman spectroscopy in humans. *Sci. Transl. Med.* **7**, 274ra19 (2015).

7. Matthäus, C. *et al.* Noninvasive imaging of intracellular lipid metabolism in macrophages by Raman microscopy in combination with stable isotopic labeling. *Anal. Chem.* **84**, 8549–56 (2012).

8. Haka, A. S. *et al.* In vivo margin assessment during partial mastectomy breast surgery using Raman spectroscopy. *Cancer Res.* **66**, 3317–22 (2006).

9. Kanter, E. M. *et al.* Application of Raman spectroscopy for cervical dysplasia diagnosis. *J. Biophotonics* **2**, 81–90 (2009).

10. Krishna, H., Majumder, S. K., Chaturvedi, P., Sidramesh, M. & Gupta, P. K. In vivo Raman spectroscopy for detection of oral neoplasia: A pilot clinical study. *J. Biophotonics* **7**, 690–702 (2014).

11. Yasser, M., Shaikh, R., Chilakapati, M. K. & Teni, T. Raman spectroscopic study of radioresistant oral cancer sublines established by fractionated ionizing radiation. *PLoS One* **9**, e97777 (2014).

12. Matthews, Q. *et al.* Radiation-induced glycogen accumulation detected by single cell raman spectroscopy is associated with radioresistance that can be reversed by metformin. *PLoS One* **10**, e0135356 (2015).

13. Harder, S. J. *et al.* Raman spectroscopy identifies radiation response in human non-small cell lung cancer xenografts. *Sci. Rep.* **6**, 21006 (2016).

14. Van Nest, S. J. *et al.* Raman Spectroscopic Signatures Reveal Distinct Biochemical and Temporal Changes in Irradiated Human Breast Adenocarcinoma Xenografts. *Radiat. Res.* **189**, 497–504 (2018).

15.   Paidi, S. K. *et al.* Label-free Raman spectroscopy reveals signatures of radiation resistance in the tumor microenvironment. *Cancer Res.* **79**, 2054–64 (2019).

16.   Stein, A. P. *et al.* Xenograft assessment of predictive biomarkers for standard head and neck cancer therapies. *Cancer Med.* **4**, 699–712 (2015).

17.   Motz, J. T. *et al.* Optical Fiber Probe for Biomedical Raman Spectroscopy. *Appl. Opt.* (2004) doi:10.1364/AO.43.000542.

18.   Felten, J. *et al.* Vibrational spectroscopic image analysis of biological material using multivariate curve resolution-alternating least squares (MCR-ALS). *Nat. Protoc.* **10**, 217–40 (2015).

19.   Wendt, H. W. Dealing with a common problem in Social science: A simplified rank-biserial coefficient of correlation based on the U statistic. *Eur. J. Soc. Psychol.* (1972) doi:10.1002/ejsp.2420020412.

20.   Pandey, R. *et al.* Noninvasive Monitoring of Blood Glucose with Raman Spectroscopy. *Acc. Chem. Res.* (2017) doi:10.1021/acs.accounts.6b00472.

21.   de Barros Souza, F. *et al.* Intramuscular lactic acid assessment through Raman spectrography: New perspectives in sports medicine. *Rev. Bras. Med. do Esporte* (2003).

22.   Stiebing, C. *et al.* Raman imaging of macrophages incubated with triglyceride-enriched oxLDL visualizes translocation of lipids between endocytic vesicles and lipid droplets. *J. Lipid Res.* (2017) doi:10.1194/jlr.M071688.

23.   Nguyen, T. T. *et al.* Characterization of type i and IV collagens by Raman microspectroscopy: Identification of spectral markers of the dermo-epidermal junction. *Spectrosc. (New York)* (2012) doi:10.1155/2012/686183.

24.   Lung, P. W. *et al.* In vivo study of dermal collagen of striae distensae by confocal Raman spectroscopy. *Lasers Med. Sci.* (2018) doi:10.1007/s10103-017-2431-3.

25.   Kuhajda, F. P. *et al.* Fatty acid synthesis: A potential selective target for antineoplastic therapy. *Proc. Natl. Acad. Sci. U. S. A.* (1994) doi:10.1073/pnas.91.14.6379.

26.   Mims, J. *et al.* Energy Metabolism in a Matched Model of Radiation Resistance for Head and Neck Squamous Cell Cancer. *Radiat. Res.* **183**, 291–304 (2015).

27.   Bansal, N. *et al.* Broad phenotypic changes associated with gain of radiation resistance in head and neck squamous cell cancer. *Antioxidants and Redox Signaling* (2014) doi:10.1089/ars.2013.5690.

28.   Alhallak, K. *et al.* Optical imaging of radiation-induced metabolic changes in radiation-sensitive and resistant cancer cells. *J. Biomed. Opt.* **22**, 60502 (2017).

29.   Lee, D. E. *et al.* A Radiosensitizing Inhibitor of HIF-1 alters the Optical Redox State of Human Lung Cancer Cells in Vitro. *Sci. Rep.* **8**, 8815 (2018).

30.	Schindl, M. *et al.* Overexpression of hypoxia-inducible factor 1α is associated with an unfavorable prognosis in lymph node-positive breast cancer. *Clin. Cancer Res.* (2002).

31.	Bos, R. *et al.* Levels of hypoxia-inducible factor-1α independently predict prognosis in patients with lymph node negative breast carcinoma. *Cancer* (2003) doi:10.1002/cncr.11246.

32.	Birner, P. *et al.* Overexpression of hypoxia-inducible factor 1α is a marker for an unfavorable prognosis in early-stage invasive cervical cancer. *Cancer Res.* (2000).

33.	Aebersold, D. M. *et al.* Expression of hypoxia-inducible factor-1α: A novel predictive and prognostic parameter in the radiotherapy of oropharyngeal cancer. *Cancer Res.* (2001).

34.	Burri, P. *et al.* Significant correlation of hypoxia-inducible factor-1α with treatment outcome in cervical cancer treated with radical radiotherapy. *Int. J. Radiat. Oncol. Biol. Phys.* (2003) doi:10.1016/S0360-3016(02)04579-0.

35.	Semenza, G. L. Oxygen Sensing, Homeostasis, and Disease. *N. Engl. J. Med.* (2011) doi:10.1056/nejmra1011165.

36.	Deng, X. *et al.* Monitor Ionizing Radiation-Induced Cellular Responses with Raman Spectroscopy, Non-Negative Matrix Factorization, and Non-Negative Least Squares. *Appl. Spectrosc.* (2020) doi:10.1177/0003702820906221.

37.	Beckers, A. *et al.* Chemical inhibition of acetyl-CoA carboxylase induces growth arrest and cytotoxicity selectively in cancer cells. *Cancer Res.* (2007) doi:10.1158/0008-5472.CAN-07-0389.

38.	Kridel, S. J., Axelrod, F., Rozenkrantz, N. & Smith, J. W. Orlistat Is a Novel Inhibitor of Fatty Acid Synthase with Antitumor Activity. *Cancer Res.* (2004) doi:10.1158/0008-5472.CAN-03-3645.

39.	Pizer, E. S. *et al.* Inhibition of fatty acid synthesis induces programmed cell death in human breast cancer cells. *Cancer Res.* (1996).

40.	De Schrijver, E., Brusselmans, K., Heyns, W., Verhoeven, G. & Swinnen, J. V. RNA interference-mediated silencing of the fatty acid synthase gene attenuates growth and induces morphological changes and apoptosis of LNCaP prostate cancer cells. *Cancer Res.* (2003).

41.	Brusselmans, K., De Schrijver, E., Verhoeven, G. & Swinnen, J. V. RNA interference-mediated silencing of the acetyl-Coa-carboxylase-α gene induces growth inhibition and apoptosis of prostate cancer cells. *Cancer Res.* (2005) doi:10.1158/0008-5472.CAN-05-0571.

42.	Chajès, V., Cambot, M., Moreau, K., Lenoir, G. M. & Joulin, V. Acetyl-CoA carboxylase α is essential to breast cancer cell survival. *Cancer Res.* (2006) doi:10.1158/0008-5472.CAN-05-1489.

43.	Rysman, E. *et al.* De novo lipogenesis protects cancer cells from free radicals and chemotherapeutics by promoting membrane lipid saturation. *Cancer Res.* (2010)

doi:10.1158/0008-5472.CAN-09-3871.

44.   Rae, C., Haberkorn, U., Babich, J. W. & Mairs, R. J. Inhibition of fatty acid synthase sensitizes prostate cancer cells to radiotherapy. *Radiat. Res.* (2015) doi:10.1667/RR14173.1.

45.   Gansler, T. S., Hardman, W., Hunt, D. A., Schaffel, S. & Hennigar, R. A. Increased expression of fatty acid synthase (OA-519) in ovarian neoplasms predicts shorter survival. *Hum. Pathol.* (1997) doi:10.1016/S0046-8177(97)90177-5.

46.   Innocenzi, D. *et al.* Fatty acid synthase expression in melanoma. *J. Cutan. Pathol.* (2003) doi:10.1034/j.1600-0560.2003.300104.x.

47.   Camassei, F. D. *et al.* Expression of the lipogenic enzyme fatty acid synthase (FAS) as a predictor of poor outcome in nephroblastoma: An interinstitutional study. *Med. Pediatr. Oncol.* (2003) doi:10.1002/mpo.10274.

48.   Bensaad, K. *et al.* Fatty acid uptake and lipid storage induced by HIF-1α contribute to cell growth and survival after hypoxia-reoxygenation. *Cell Rep.* (2014) doi:10.1016/j.celrep.2014.08.056.

49.   Krontiras, H. *et al.* Fatty acid synthase expression is increased in neoplastic lesions of the oral tongue. *Head Neck* (1999) doi:10.1002/(SICI)1097-0347(199907)21:4<325::AID-HED6>3.0.CO;2-P.

50.   Li, M., Jendrossek, V. & Belka, C. The role of PDGF in radiation oncology. *Radiation Oncology* (2007) doi:10.1186/1748-717X-2-5.

51.   Yarnold, J. & Vozenin Brotons, M. C. Pathogenetic mechanisms in radiation fibrosis. *Radiotherapy and Oncology* (2010) doi:10.1016/j.radonc.2010.09.002.

52.   Krasny, L. *et al.* An in-vitro tumour microenvironment model using adhesion to type i collagen reveals Akt-dependent radiation resistance in renal cancer cells. *Nephrol. Dial. Transplant.* (2010) doi:10.1093/ndt/gfp525.

53.   Wong, C. C. L. *et al.* Hypoxia-inducible factor 1 is a master regulator of breast cancer metastatic niche formation. *Proc. Natl. Acad. Sci. U. S. A.* (2011) doi:10.1073/pnas.1113483108.

54.   Li, J. *et al.* Lipid Desaturation Is a Metabolic Marker and Therapeutic Target of Ovarian Cancer Stem Cells. *Cell Stem Cell* (2017) doi:10.1016/j.stem.2016.11.004.

55.   Le, T. T., Huff, T. B. & Cheng, J. X. Coherent anti-Stokes Raman scattering imaging of lipids in cancer metastasis. *BMC Cancer* (2009) doi:10.1186/1471-2407-9-42.

56.   Zhang, C., Li, J., Lan, L. & Cheng, J. X. Quantification of Lipid Metabolism in Living Cells through the Dynamics of Lipid Droplets Measured by Stimulated Raman Scattering Imaging. *Anal. Chem.* (2017) doi:10.1021/acs.analchem.6b04699.

57.   Pelletier, J. *et al.* Glycogen Synthesis is Induced in Hypoxia by the Hypoxia-Inducible Factor and Promotes Cancer Cell Survival. *Front. Oncol.* (2012)

doi:10.3389/fonc.2012.00018.

Table 1. Tumor distribution in different groups. NT and XT respectively represent control and radiated animals.

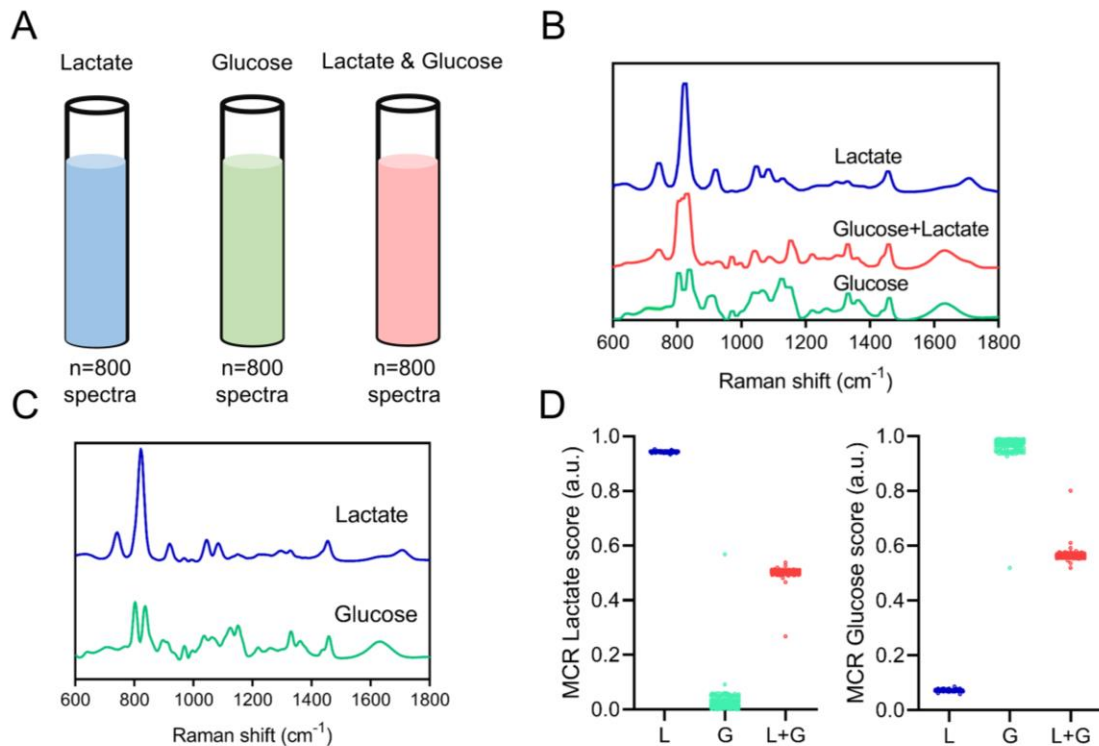| Cell line	Treatment	Baseline	1h	24h	48h
UM-SCC-22B	NT	7	3	3	2
	XT		2	3	2
UM-SCC-47	NT	4	3	3	3
	XT		4	4	4

Figure 1. MCR-ALS analysis of aqueous solutions with known content. **A**, 800 Raman spectra from Lactate-only, Glucose-only, and combined Lactate and Glucose solutions. **B**, Average Raman spectra from three different solutions. Standard deviations from group average were smaller than the lines and hence, are not visible. **C**, MCR-coefficients extracted from the MCR-ALS algorithm. **D**, MCR-scores of lactate and glucose of individual Raman spectra from 2400 spectral measurements.
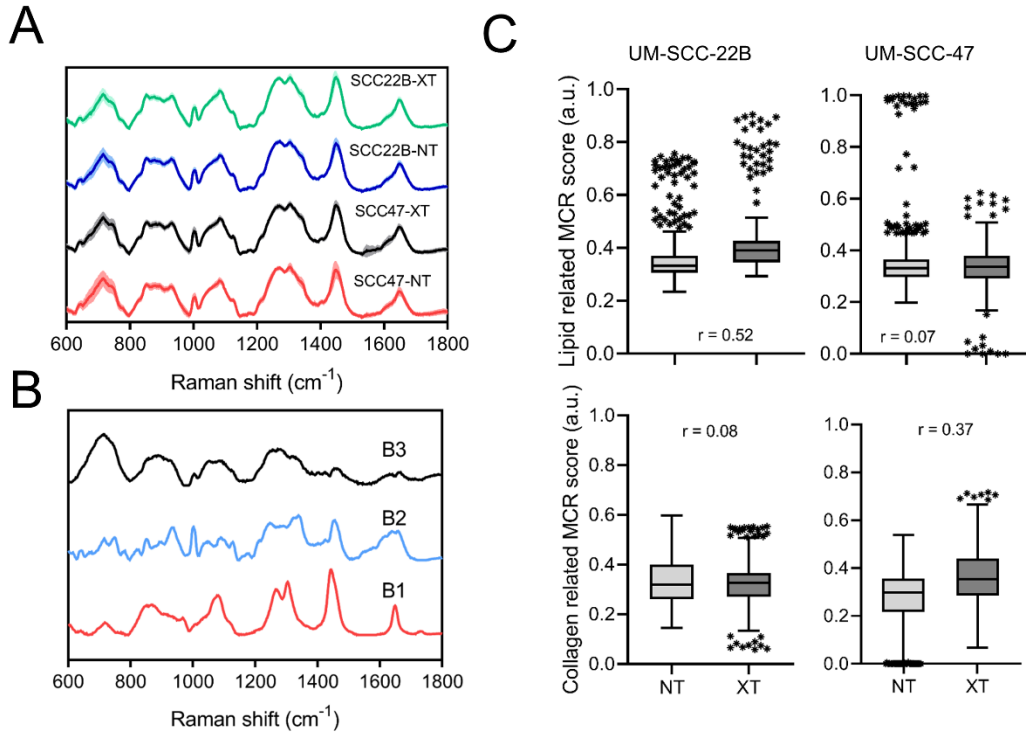
Figure 2. Spectral decomposition of Raman spectra using MCR-ALS algorithm. A, Average Raman spectra ± 1 standard deviations from group mean (transparent shadow) collected from NT and XT treated radiation-resistant (UM-SCC-47) and radiation-sensitive (UM-SCC-22B) head and neck tumor xenografts. B, MCR-coefficients derived from raw Raman spectra. B1 and B2 respectively represent lipid-rich and collagen-rich loadings. B3 represents a loading that contains spectral features from combination of weak collagen and nucleic acid. C, Boxplots illustrating the scores of lipid-rich and collagen-rich coefficients in UM-SCC-22B (left panel) and UM-SCC-47 tumors (right panel). Outliers are <10% data from each group. No significant differences were observed using Wilcoxon rank sum test. The effect size (r) also provided.
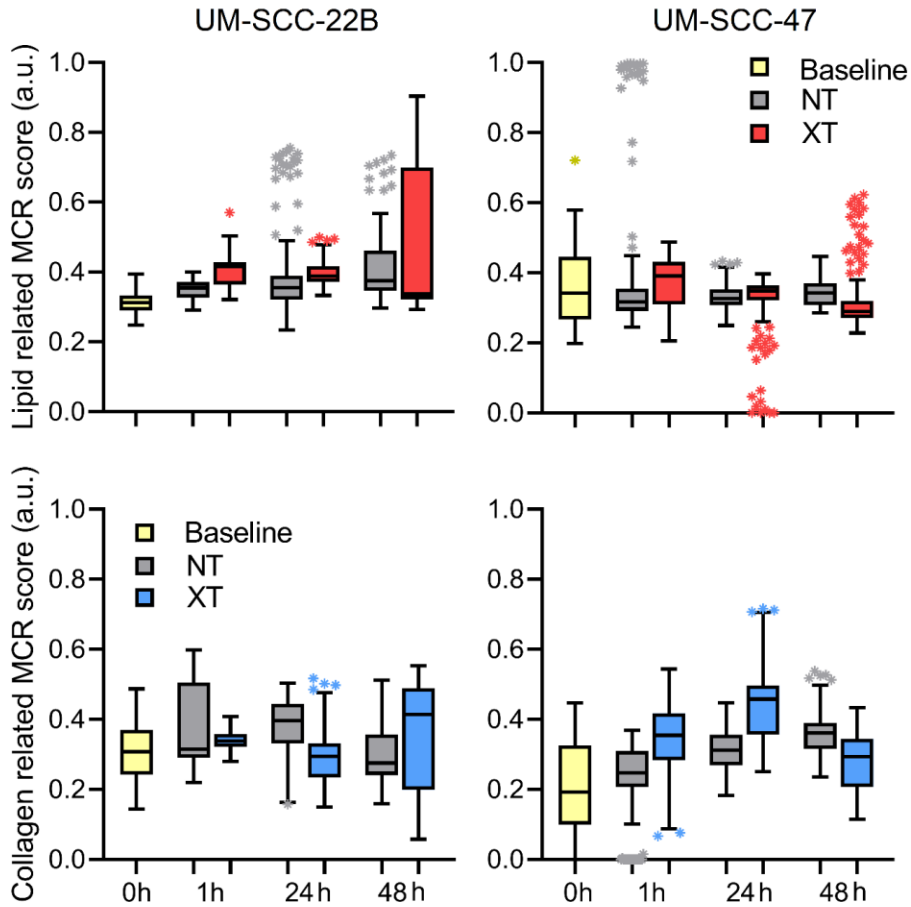
Figure 3. MCR scores of UM-SCC-22B and UM-SCC-47 tumors at different time points after radiation. Boxplots illustrating the scores of lipid-rich and collagen-rich coefficients in UM-SCC-22B (left panel) and UM-SCC-47 tumors (right panel). Outliers in each group illustrated using asterisks with highest percentage of outliers (15%) observed in 1H-NT group. Effect sizes are provided for each comparison. Statistical analysis not performed because of presence of n=2 samples in some of time points.
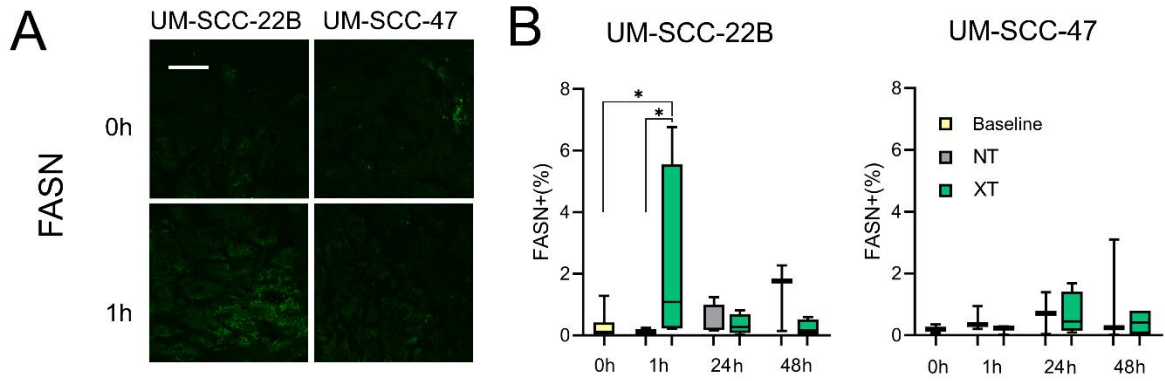
Figure 4. Immunohistochemical assessment of FASN in tumor tissue sections. A, Representative images from UM-SCC-22B and UM-SCC-47 tumors excised at baseline and 1 hours after radiation. The false-colored green signal represents FASN positive pixels. The scale bar represents 250 μm. B, Quantification of percentage of FASN positive pixels in UM-SCC-22B and UM-SCC-47 tumors.
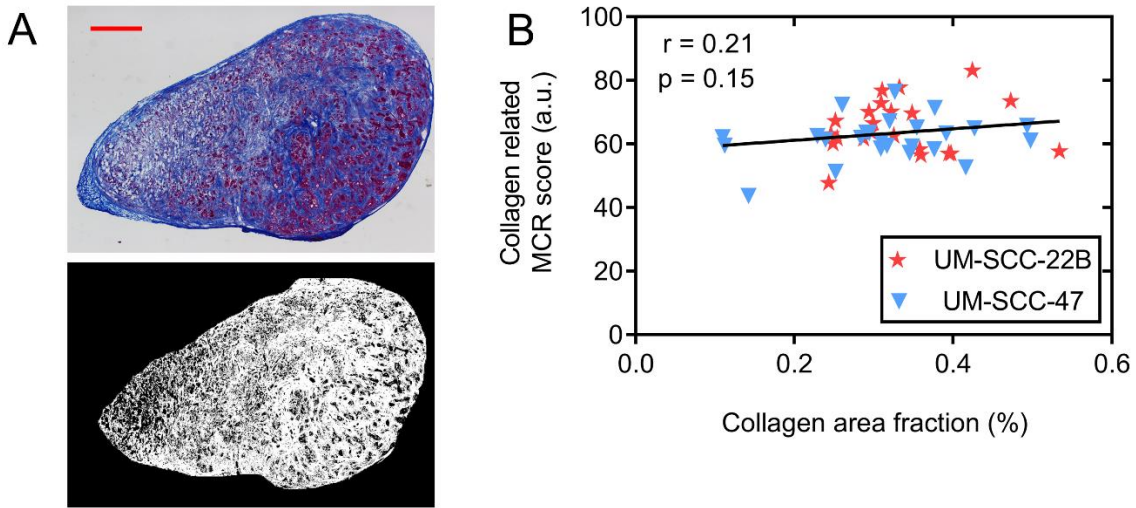
Figure 5. A, Representative UM-SCC-22B tumor stained with Masson's Trichrome and its corresponding binarized version. White pixels indicate collagen-positive regions. The scale bar represents 1 mm. B, Scatter plot representing the association between histologically-determined collagen fraction and collagen-related MCR scores in UM-SCC-22B (red stars) and UM-SCC-47 (blue inverse triangle) tumors. Symbols include tumors excised before, 1h, 24, and 48 hours after radiation. Black solid line indicates the regression line.

Chapter 5: Conclusion

Summary

This dissertation used diffuse reflectance and Raman spectroscopy to investigate the association between radiation-induced physiological and biomolecular changes with radiosensitivity of the employed tumors. These studies were carried out on tumor xenografts that were inoculated with two human head and neck cancer cell lines, UM-SCC-22B (isolated from radiation-sensitive sensitive tumor) and UM-SCC-47 (isolated from a radiation-resistant tumor), to represent various radiosensitivity of head and neck tumors that is observed in head and neck oncology.

Because tumor hypoxia has long been linked to poor radiation-response, we first investigated the association between diffuse reflectance spectroscopic measurements of oxygen saturation with tumor hypoxia. We showed optically determined oxygenation is negatively correlated with tumor hypoxic fraction and hence can serve as a negative indicator of tumor hypoxia. Next, we investigated whether physiology of radiation-resistant and -sensitive tumors are altered differently in response to radiation and identified measurable differences in reoxygenation kinetics of radiation-resistant and -sensitive tumor xenografts in pre-clinical animal models. Based on radiation-induced changes in optical properties, we trained a logistic regression model that is capable of classifying treatment failure and local control tumors. Although the observed accuracy and the area under the curve associated with the model is not ideal, we believe that the addition of Raman spectroscopy can greatly improve the overall accuracy of the model by providing quantitative measures of both functional and biomolecular changes in the tumor microenvironment. Thus, investigating additional features (e.g. radiation-induced biomolecular changes) can improve our understanding of radioresistant-phenotype and improve our ability to identify responding and non-responding tumors.

Raman spectroscopy has previously been shown to identify different biomolecular composition, specifically lipids and collagen, in radiation-resistant and -sensitive tumors that were excised 25-30 days after radiation[1]. However, it is not clear whether *in vivo* measurements at early time points after radiation can identify different biomolecular changes among radiation-resistant and -sensitive tumors. Thus, to study radiation-induced biomolecular changes in tumor microenvironment and the association of these changes with tumor radiosensitivity, we performed *in vivo* Raman spectroscopy on radiation-resistant and -sensitive tumors in the first 48 hours after radiation. We observed difference in the spectral scores of lipid and collagen respectively in radiation-sensitive and -resistant tumors. These results indicate that Raman spectroscopy can detect biomolecular changes between radiation-resistant and -sensitive tumors as early as 48 hours after radiation and can potentially serve as biomarkers for identification of radiation-resistant and -sensitive tumors.

Future studies include simultaneous measurements of diffuse reflectance and Raman spectra with the goal of characterizing radiation-induced reoxygenation and biomolecular changes in head and neck cancer patients. These two modalities will be combined by engineering novel spatially-offset probe that can be used to access tumors of oral cavity or delivered to tumors of pharynx and larynx thru the working channel of flexible laryngoscopes (Figure 1). Prior to initiation of treatment on these patients, baseline RS and DRS spectra will be acquired. Subsequent optical measurements will be performed on following days after each dose of radiation and kinetics of oxygenation and biomolecular contents will be associated with radiation response. We envision that performing combined diffuse reflectance and Raman spectroscopic measurements on numerous responding and non-responding patients can help us develop artificial intelligence-based-model that based on only baseline measurement, can identify radiation-responsive and non-responsive HNSCC patients.

However, prior to initiation of clinical trials, feasibility studies for measurements of diffuse reflectance, Raman spectra, and their combination can help us optimize measurement protocols,

and modify software and hardware of these systems. One such feasibility study has already been initiated in otolaryngology department of University of Arkansas for Medical Science Winthrop P. Rockefeller Cancer Institute. The objective of this single-arm observational study is to investigate the feasibility of using diffuse reflectance spectroscopy for measuring optical properties of 10 patient tumors that are located inside the oral cavity. Three optical spectra will be collected from the diseased tonsil, the contralateral healthy tonsil, and a normal tissue site on the buccal mucosa. The acquisition of control spectra from normal tissue will allow normalization of each tumor spectrum to the patient's normal tissue, and significantly reduce inter- and intra-patient variability. The acquisition of spectra from contralateral healthy tonsil will serve as a control measurement that represents functional properties of healthy tonsil. Patients with tumors on both tonsils and patients who have undergone any form of treatment or surgery will be excluded from this study. Success metrics defined for this study includes the acquisition of optical spectra with a high signal to noise ratio (of at least 100) that can be fit to our data analysis models to extract meaningful endpoints, such as total hemoglobin, vascular oxygenation, and tissue scattering in at least 80% of the patients enrolled in the study. So far, we have recruited 6 Caucasian male tonsil cancer patients with average age of 50. However, the employed LUT model was able to fit only half of the acquired spectra. Table 1 presents the distribution of successful fits across different patients and measurements sites. Figure 2A illustrates representative diffuse reflectance spectra collected from diseased tonsil (black solid), contralateral healthy tonsil (black dashed line), normal buccal mucosa (black dashed-dot line), their corresponding LUT fits (red solid line), and their corresponding chi-squared values. As seen in the figure, the LUT failed to successfully fit the spectra collected from normal buccal mucosa. Quantification of accepted fits from all three sites among 6 patients yielded high values of vascular oxygenation for spectra collected from tissue sites (figure 2B). However, as mentioned earlier, the LUT was not able to fit half of the collected spectra. We strongly believe this is driven by the lack of proper contact between optical probe and the tissue at the time of data acquisition. We continue to work with our physician collaborators

in optimizing our data acquisition protocol that guarantees data acquisition when probe is in complete contact with the tissue. However, such success may never be achieved due to lack of visibility of the probe-tumor interface inside upper aero-digestive tract. An alternative solution can be the use of optical probe equipped with pressure or proximity sensors that automatically triggers acquisition of spectra as soon as the probe comes into contact with the tumor[2]. Such measures can eliminate the uncertainties of data acquisition and pave the way for initiation of large-scale clinical trials where combined diffuse reflectance and Raman spectroscopy can be used for monitoring radiation-response of head and neck cancer patients.

<u>Future work</u>

Diffuse optical spectroscopy is a powerful technique that is capable of non-invasive monitoring of tumor physiology and thanks to its short integration time, is ideal for accessible tumors of oral cavity. Our pre-clinical study on tumor xenografts identified reoxygenation phenomena in radiation-resistant tumors, which combined with other immunohistochemical proofs, suggested that OCR reduction in response to radiation is the driving factor for radioresistant phenotype. However, numerous studies have identified reducing OCR as a strategy in improving treatment response[3–7]. Thus, several important questions remain unanswered: Does the sequence of HIF-1 inhibition and OCR reduction carries significance? How do they affect reoxygenation kinetics and how do they differ in radiation-resistant and -sensitive tumors? To answer such questions, kinetics of reoxygenation, OCR, and HIF-1 content (respectively using DRS, seahorse assay, and western blot or immunohistochemistry) induced by radiation alone, combined with HIF-1 inhibitor, combined with OCR reducing agents, and combined with both treatments in various sequences should be monitored to shed additional light about the relevance of these pathways to radiation-resistance. Acquired optical properties can also be used for classification purposes. Thus, gathering larger dataset can also be beneficial in terms of training

of various machine learning algorithms for accurate classification of local-control and treatment-failure tumors.

We and others have extensively utilized diffuse reflectance spectroscopy in pre-clinical and clinical *in vivo* studies and hence, have a solid understanding of the setup, models used for simulating light-tissue interaction, and the association between probe geometry, wavelength, and penetration depth. In contrast, Raman spectroscopy has been investigated to a lesser extent in biological tissue and deserves detailed studies before its clinical translation. For example, multilayer tissue stimulating phantoms with known content and concentrations can provide a better understanding in terms of whether Raman spectroscopic measurements provide a depth averaged reading of sample. Accurate measurement of penetration depth can also be helpful in designing spatially-offset probes that can later be used for longitudinal in vivo studies where treatment response of individual animals can be monitored. In addition to depth penetration, such experiments can uncover the accuracy of MCR-ALS algorithm in determining sample constituents. Alternatively, tumors with known specific microenvironmental characteristics can be utilized to pursue such studies. For example, using B16.BL6 murine melanoma cell line which presents increased MMP9 expression, we can expect to observe lower collagen content determined by Raman spectroscopy combined with MCR-ALS algorithm. This can provide a controlled method to validate the sensitivity of the Raman spectroscopy and MCR-ALS algorithm to specific biomolecular constituents of tissue.

Although our *in vivo* Raman spectroscopic studies uncovered early radiation-induced changes in lipids and collagens, additional studies can shed light on biological pathways that lead to observed biomolecular changes. For example, pharmacological and/or RNA mediated inhibition of HIF-1 and FASN can provide valuable information on differential pathways that radiation-resistant and -sensitive tumors take. One intriguing way to study the effect of modulating these pathways is window chamber model of cancer because it enables gathering additional information such as tumor oxygenation using hyperspectral imaging and tumor redox state using

95

nonlinear two photon microscopy. Alternatively, these studies can be pursued at the cellular level since they lack the complexity of dynamic tumor microenvironment and hence, result interpretation become less challenging.

Finally, longitudinal and simultaneous monitoring of animals using combination of *in vivo* DRS and Raman spectroscopy will enable us to correlate the observed radiation-induced physiological and biomolecular changes with treatment outcome and hence, will provide better understanding with possible pathways involved in radiation-resistance. In addition, combination of these modalities will enable us with identifying the earliest time point at which diffuse reflectance spectroscopy, Raman spectroscopy, or their combination can accurately classify treatment responders and non-responders.

References

1. Paidi, S. K. *et al.* Label-free Raman spectroscopy reveals signatures of radiation resistance in the tumor microenvironment. *Cancer Res.* **79**, 2054–64 (2019).

2. Palmer, G. M. Assessing effects of pressure on tumor and normal tissue physiology using an automated self-calibrated, pressure-sensing probe for diffuse reflectance spectroscopy. *J. Biomed. Opt.* (2018) doi:10.1117/1.jbo.23.5.057004.

3. Benej, M. *et al.* Papaverine and its derivatives radiosensitize solid tumors by inhibiting mitochondrial metabolism. *Proc. Natl. Acad. Sci. U. S. A.* (2018) doi:10.1073/pnas.1808945115.

4. Crokart, N. *et al.* Glucocorticoids modulate tumor radiation response through a decrease in tumor oxygen consumption. *Clin. Cancer Res.* (2007) doi:10.1158/1078-0432.CCR-06-0802.

5. Crokart, N. *et al.* Tumor radiosensitization by antiinflammatory drugs: Evidence for a new mechanism involving the oxygen effect. *Cancer Res.* (2005) doi:10.1158/0008-5472.CAN-05-1288.

6. Crokart, N. *et al.* Early reoxygenation in tumors after irradiation: Determining factors and consequences for radiotherapy regimens using daily multiple fractions. *Int. J. Radiat. Oncol. Biol. Phys.* (2005) doi:10.1016/j.ijrobp.2005.02.038.

7. Diepart, C. *et al.* Arsenic trioxide treatment decreases the oxygen consumption rate of tumor cells and radiosensitizes solid tumors. *Cancer Res.* (2012) doi:10.1158/0008-5472.CAN-11-1755.

Table 1. Tumor distribution in different groups. NT and XT respectively represent control and radiated animals.

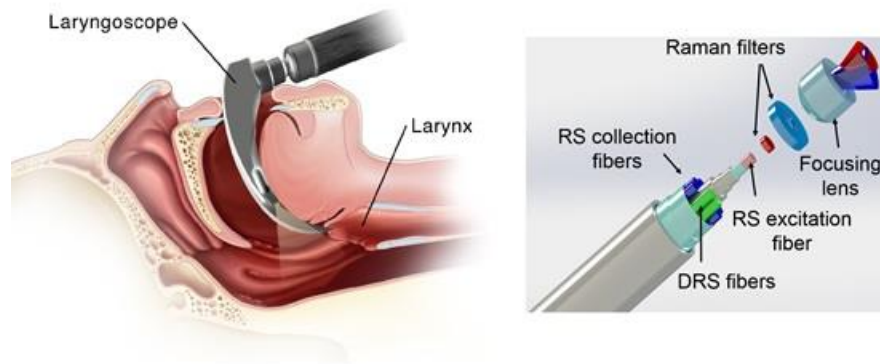| Patient	Age	Gender	Race	Diseased Tonsil			Healthy Tonsil			Buccal Mucosa			Accepted spectra	Surgeon	
#1	37	Male	Caucasian										33%	EV	
#3	56	Male	Caucasian										0%	EV	33%
#4	41	Male	Caucasian										77%	EV	
#5	49	Male	Caucasian										22%	EV	
#2	66	Male	Caucasian										66%	MM	72%
#6	55	Male	Caucasian										77%	MM	
				44%			38%			55%			Accepted spectra		

Figure 1. Delivery of combined Diffuse reflectance and Raman spectroscopic probe to tumor. For tumors located in upper aero-digestive tract (i.e. larynx, pharynx, etc.) the probe will be inserted into working channel of an NET laryngoscope.
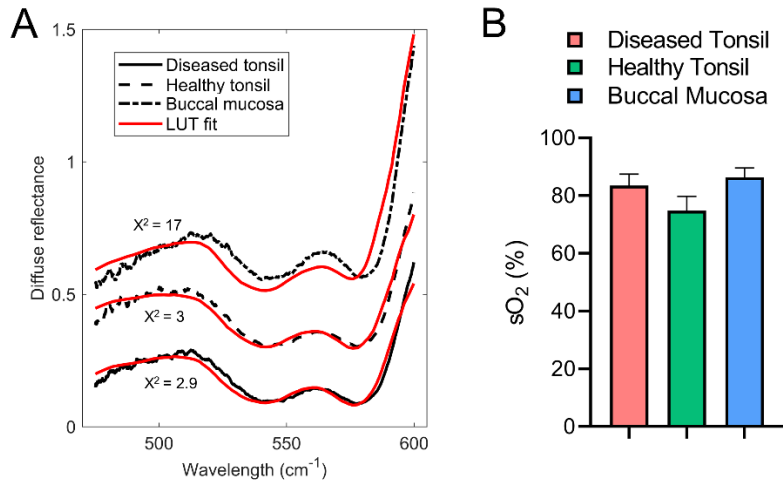
Figure 2. A. Representative DRS spectra acquired from diseased tonsil, contralateral healthy tonsil, normal buccal mucosa, and their corresponding LUT fits. B. Quantification of oxygen saturation from different tissue sites. Bars and error bars respectively represent mean and standard deviation of the mean.

Appendix

IACUC protocol approval

UNIVERSITY OF ARKANSAS

Office of Research Compliance

To: Narasimhan Rajaram
Fr: Craig Coon
Date: January 17th, 2018
Subject: IACUC Approval
Expiration Date: December 19th, 2018

The Institutional Animal Care and Use Committee (IACUC) has APPROVED your protocol # **18061**: *Functional optical markers of radiation resistance in tumors*.

In granting its approval, the IACUC has approved only the information provided. Should there be any further changes to the protocol during the research, please notify the IACUC in writing (via the Modification form) prior to initiating the changes. If the study period is expected to extend beyond December 19th, 2018 you can submit a modification to extend project up to 3 years, or submit a new protocol. By policy the IACUC cannot approve a study for more than 3 years at a time.

The following individuals are approved to work on this study: Narasimhan Rajaram and Sina Dadgar. Please submit personnel additions to this protocol via the modification form prior to their start of work.

The IACUC appreciates your cooperation in complying with University and Federal guidelines involving animal subjects.

CNC/tmp

Vita

Sina Dadgar was born in Maku, WA, Iran in 1990. He attended Azad university of Miyaneh and obtained his bachelor's degree in Electrical Engineering in June 2012. He entered graduate school in Bahcesehir University in Istanbul, Turkey and received his master's degree in Electrical Engineering in December 2013. He started his PhD program in Biomedical Engineering department in University of Arkansas in August 2016.

This dissertation has been typed by the author and reviewed by his academic advisors.